Norman, Benjamin E., Ph.D., August, 2003 NUCLEAR PHYSICS

HIGH P_T CHARGED KAON PRODUCTION IN

$\sqrt{S_{NN}}$ = 200 GEV AU-AU COLLISIONS AT RHIC (121 pp.)

Director of Dissertation: Spyridon Margetis

Relativistic heavy-ion collisions compress nuclei to states of extremely high temperature and density. Under these conditions, phenomenological models as well as Lattice QCD calculations predict a phase transition in nuclear matter, in which quarks and gluons are no longer bound in hadrons but instead can move freely inside the interaction volume. This transition would be accompanied by a restoration of chiral symmetry, and the resulting state is called Quark Gluon Plasma (QGP). The observation of this phase transition and the study of the dynamics and properties of the deconfined phase have important consequences, both for the understanding of QCD and for cosmology, as it recreates conditions that existed for the universe as a whole some 10 μs after the Big Bang.

Charged Kaons can provide signals of the formation of a QGP. First, they cary a large fraction of the strange quark content of the hadrons produced in the collision. The amount of strangeness can probe the degree of chemical equilibrium in the system. Chemical equilibrium may occur in a QGP or a normal hadronic system, but it occurs much more quickly in a QGP. Another benefit of measuring charged Kaons is that they provide identified spectra at high transverse momentum. A suppression of high momentum particles in heavy ion collisions relative to smaller systems can suggest partonic energy loss in a color deconfined medium

The technique used in this analysis to identify charged Kaons is the topological reconstruction of their one-prong decays: e.g. $K^{\pm} \rightarrow \mu^{\pm} + \nu_{\mu}$ (63.5%) or $K^{\pm} \rightarrow \pi^{\pm} + \pi^{0}$ (21.2%). This is similar to traditional 'V0' reconstruction, except we observe the charged parent and daughter of the decay. The main tracking device in the STAR detector is a Time Projection Chamber (TPC), which is a cylindrical ionization chamber 2 meters in radius and 4.5 meters long having pad readouts at the endcaps. This allows 3D reconstruction of charged particle trajectories.

Presented in this Dissertation is a measurement of the charged Kaon spectra in $\sqrt{s_{NN}} = 200$ GeV Au-Au collisions at the Relativistic Heavy Ion Collider during 2001. Our data set is about 3 million "central" events and 3 million "minimum bias" events.

Spectra are presented out to transverse momenta of 4 GeV/c, and the ratio K^{-}/K^{+} is presented as a function of collision centrality and rapidity. For the most central collisions, the charged Kaon yield ($(K^{-} + K^{+})/2$) at midrapidity is dN/dy = 55. For comparison this value in 130 GeV collisions was dN/dy = 50. We observe a suppression of high p_{T} charged Kaons in central collisions relative to peripheral. This suppression has a number of possible sources, one of which may be partonic energy loss in a colored medium. The measurements presented here further supplement the rich data being produced at RHIC and contribute to understanding the physics of heavy ion collisions at $\sqrt{s_{NN}} = 200$ GeV.

HIGH P_T CHARGED KAON PRODUCTION IN $\sqrt{S_{NN}} = 200$ GEV AU-AU COLLISIONS AT RHIC

A dissertation submitted to
Kent State University in partial
fulfillment of the requirements for the
degree of Doctor of Philosophy

by

Benjamin E. Norman

August, 2003

Dissertation written by

Benjamin E. Norman

B.S., Kent State University, 1998

Ph.D., Kent State University, 2003

Approved by

_____ , Chair, Doctoral Dissertation Committee

_____ , Members, Doctoral Dissertation Committee

_____ ,

_____ ,

_____ ,

Accepted by

_____ , Chair, Department of Physics

_____ , Dean, College of Arts and Sciences

Table of Contents

List of Figures

List of Tables

Acknowledgments

First and foremost, I would like to thank my research advisor, Dr. Spyridon Margetis. His encouragement and motivation over the past 5 years have been a major factor in the completion of this undertaking. His support in this dissertation and other facets of my graduate education has been invaluable.

I also want to thank Dr. Declan Keane and Dr. George Fai at Kent State for enlightening discussions regarding my research. I have also received much insight from conversations with Dr. Peter Jacobs at Lawrence Berkeley National Lab, Dr. Fuqiang Wang at Purdue University, Dr. Rene Bellwied and Dr. Claude Pruneau at Wayne State University, and Dr. Helen Caines at Yale University.

The faculty and staff here at Kent State have been very supportive, and I would be remiss in not thanking them for their help in my tenure here. That time was made all the more enjoyable by the company of my classmates. John, Nate, Strahinja, Tony, Will, it was great to go through this with you guys. I am constrained by space, or I would name all the friends I have made inside and outside the department. I will remember you and the times we have shared for the rest of my life.

The encouragement of my father and mother, William and Virginia, for the last 28 years of my life has had a great impact on my course thus far, and I thank them for all they have given me.

Lastly, I would like to thank my lovely companion for the past year, Patricia Mullins. Her love and support has been a tremendous source of strength for me. I can only hope to repay that in the days that come.

Chapter 1

Introduction

The purpose of the RHIC facility is to provide an environment where various experiments, such as STAR, may probe the fundamental interactions of the constituents of nuclear matter. In the standard model, hadronic matter is composed of massive quarks which interact through the exchange of massless gluons.

1.1 The Color Interaction

Quarks are spin 1/2 fermions with electromagnetic charge +2/3 or -1/3. In addition, they have *flavor* and *color* degrees of freedom. Gluons also have color, and it is this degree of freedom that corresponds to the strong nuclear force. The dominant theory to describe this interaction is *Quantum ChromoDynamics* (QCD), where *chromo* refers to the color interaction.

Unlike gravity, electromagnetism, and the weak nuclear force, the coupling constant for the color force increases as the separation between quarks grows. In fact, it can be shown through detailed simulation on a discreet lattice of space-time (*lattice QCD*) that the effective interaction is approximately linear with the separation. [5] It is easily shown that this behavior makes *deconfinement* of single quarks impossible under normal conditions. As two quarks are separated, it becomes energetically more favorable to form a quark-antiquark pair from the vacuum than to increase the separation of the original quarks. Under normal pressures and densities, quarks are thought to only exist as color singlets such as 3-(anti)quark states called (anti)*baryons*

and quark-antiquark states called *mesons*.

1.2 Deconfinement

To fully calculate the effect of the strong nuclear force requires the summation of an infinite number of integrals, each containing a different power of the coupling constant, α_s. These sums are impossible to calculate to a good approximation when α_s is not small. Since the QCD coupling between two quarks decreases with decreasing distance, however, one may discard higher terms in α_s at very short distances. This regime of very low coupling strength is called *asymptotic freedom* and corresponds to high momentum transfers. *Perturbative QCD* describes the physics where the truncation of the full sum is a good approximation. Unfortunately, however, the coupling in nucleons – the only stable states of matter available to the experimentalist – is not small enough to permit a perturbative treatment.

One very simple way of dealing with the nonperturbative nature of a colored system is the *MIT Bag Model*. This model consists of quarks and massless gluons in a "bag". Inside the bag, the quarks are massless. Outside, they are infinitely massive, thus the bag provides a boundary for the quarks. The kinetic pressure from the quarks thus contained is balanced by a phenomenological *bag constant*, which represents an external pressure on the bag. The bag constant is a neat way of accounting for all the nonperturbative effects.

In this simple model, one sees that the contained quarks could break free of the bag if either their energy increased (kinetic pressure) or more quarks were present in the bag (Pauli pressure). Eventually, the internal pressure would exceed the bag pressure, and the quarks would be deconfined.

1.3 Chiral Symmetry

The bare or *current* masses of quarks are those which appear explicitly in the QCD Lagrangian. The current masses of three lightest quarks are small compared to the mass of the lightest baryon ($m_u \simeq 4\,\mathrm{MeV}/c^2$, $m_d \simeq 7\,\mathrm{MeV}/c^2$, $m_s \simeq 150\,\mathrm{MeV}/c^2 \ll m_p \simeq 1\,\mathrm{GeV}/c^2$). Chiral symmetry corresponds to the conservation of *helicity* (the projection of a particle's spin on to its direction of motion); helicity is definite for massless particles. We can say that chiral symmetry is explicitly broken by the mass term in the Lagrangian, but that it is still an approximate symmetry because the masses are small compared to baryons. If we let the current masses vanish, then chiral symmetry is restored to the Lagrangian. This is an $\mathrm{SU}(3)_L \times \mathrm{SU}(3)_R$ symmetry because the now-massless quarks must have definite helicity, and the left- and right-handed quarks transform independently under flavor rotation.

Even assuming zero mass for the light quarks, though, one runs into problems at low energies. [6] Consider the vacuum at low temperature. Even a vacuum totally devoid of matter will have fluctuations whereby a quark-antiquark pair may be created, so long as that creation does not violate the uncertainty principle. If such a $q\bar{q}$ pair is to be formed from the vacuum at a separation r, the quark and antiquark must have a relative momentum (and kinetic energy) of about 1/r. (Here we use natural units and apply the momentum-position formulation of the uncertainty principle.) At small r, the potential from the color field has a Coulomb form $-4\pi\alpha_s/r$, where α_s goes roughly as $1/\ln\frac{1}{r}$. We should define what is meant by small at this point. The characteristic momentum scale of QCD is $\Lambda_{qcd} \simeq 200$ MeV. This corresponds to a length scale r_0 of about 1 fm ($\hbar c \simeq 197$ MeV fm $= 1$ in natural units). We see that the potential energy will be overshadowed by the kinetic energy due to the

logarithmic factor, and so the total energy is positive for very low r. At larger r, the potential is approximately proportional to r, and so the total energy there is also positive. At some point, near r_0, the energy is minimized and can be shown to be negative through detailed calculation.

In summary, the empty vacuum is not the most energetically favorable configuration. It is preferred to have $q\bar{q}$ pairs created at a distance r_0 than to have a complete void. The QCD "vacuum", then, actually refers to a random distribution of color charge pairs. Another way this is often stated is that the expectation value of the quark condensate, $\langle \bar{q}q \rangle$ is nonzero. One can now examine how this affects chirality. If a left-handed test quark is placed in the vacuum, it may annihilate with a left-handed antiquark that was produced in tandem with a right-handed quark, its partner as described above. What will remain is the right-handed quark, and it appears as if a quark changed its helicity. This implies a mass, and so we encounter *dynamical chiral symmetry breaking*. Even if the light quarks did not have explicit masses appearing in the Lagrangian, they acquire a dynamical contribution to the mass that spontaneously breaks chiral symmetry. This results in a *constituent* mass of about 360 MeV for up and down quarks, and 540 MeV for strange quarks.

At higher temperatures, however, the kinetic energy of these quark-antiquark pairs is increased. There will be a critical temperature where the total energy of the pair is always positive, and the existence of the pair will not be energetically favorable. This restores chiral symmetry as the $\langle \bar{q}q \rangle$ disappears.

1.4 Quark-Gluon Plasma

The term Quark-Gluon Plasma (QGP) refers to a phase of deconfined quarks and gluons. This can be accomplished at very high baryon density, temperature, or both.

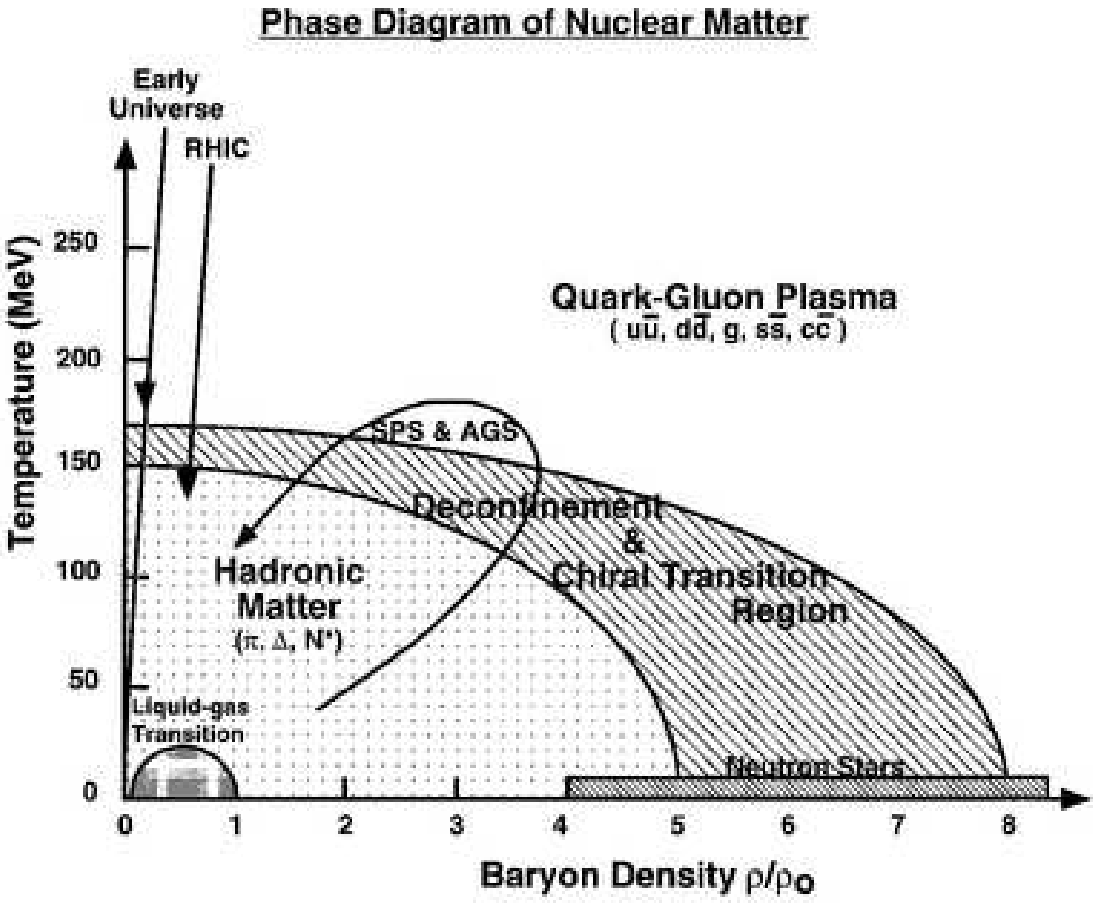

Figure 1.1: Phase diagram of nuclear matter

The phase diagram of nuclear matter is shown in Figure 1.1. The temperature, T, is shown on the vertical axis, and the baryon density, ρ_B, is shown on the horizontal axis. The latter reflects the net baryon density of the system.

The phase transition to deconfined quarks and gluons is expected to be accompanied by a restoration of chiral symmetry. This can be seen in the simple qualitative argument above for the high temperature, low baryon density region. The QGP would be a perturbative QCD system, and color charges would be free to move through it. [7]

In an Au-Au collision at RHIC energies ($\sqrt{s_{NN}} = 200$ GeV), it is theorized that gluon interactions would dominate at early times. [8] A gluon-rich QGP may form in the hot, dense interaction region. We can see the evolution of the collision in Figure 1.2. The QGP could reach a chemical equilibrium between the different quark flavors, but this is not required. After some time, a phase transition back to hadronic matter occurs. As the hadron gas expands and cools, the chemical balance of the particles is effectively fixed because inelastic collisions stop. This is referred to as *chemical freeze-out*, and is thought to occur about 160 - 170 MeV. At some later time, the particles separate to the point where they no longer interact even elastically, and the system is said to undergo *thermal freeze-out*. This is around 120 MeV.

1.5 Probing the QGP

The mysteries of the early state of the collision (before chemical and thermal freeze-out) are well hidden from the experimentalist. The most basic tools available, such as total yields and momentum spectra, provide a snapshot of the system at freeze-out. In order to gain insight into the nature of the system before that time, we must use more subtle probes. [9] Such probes almost always involve the study of high momentum particles, because the early stage of the collision is dominated by hard scattering of quarks and gluons. STAR is equipped to study high p_{T} photons and charged particles. Jets and leading particles are of particular interest because they may be sensitive to differences in energy loss between excited hadronic matter and a QGP. The size and duration of the early state may be inferred from Hanbury-Brown and Twiss (HBT) interferometry. This technique originated in astrophysics but is can be applied to heavy ion collisions by measuring the correlation between like particles.

The chemical freeze-out conditions may be determined by examining the strangeness

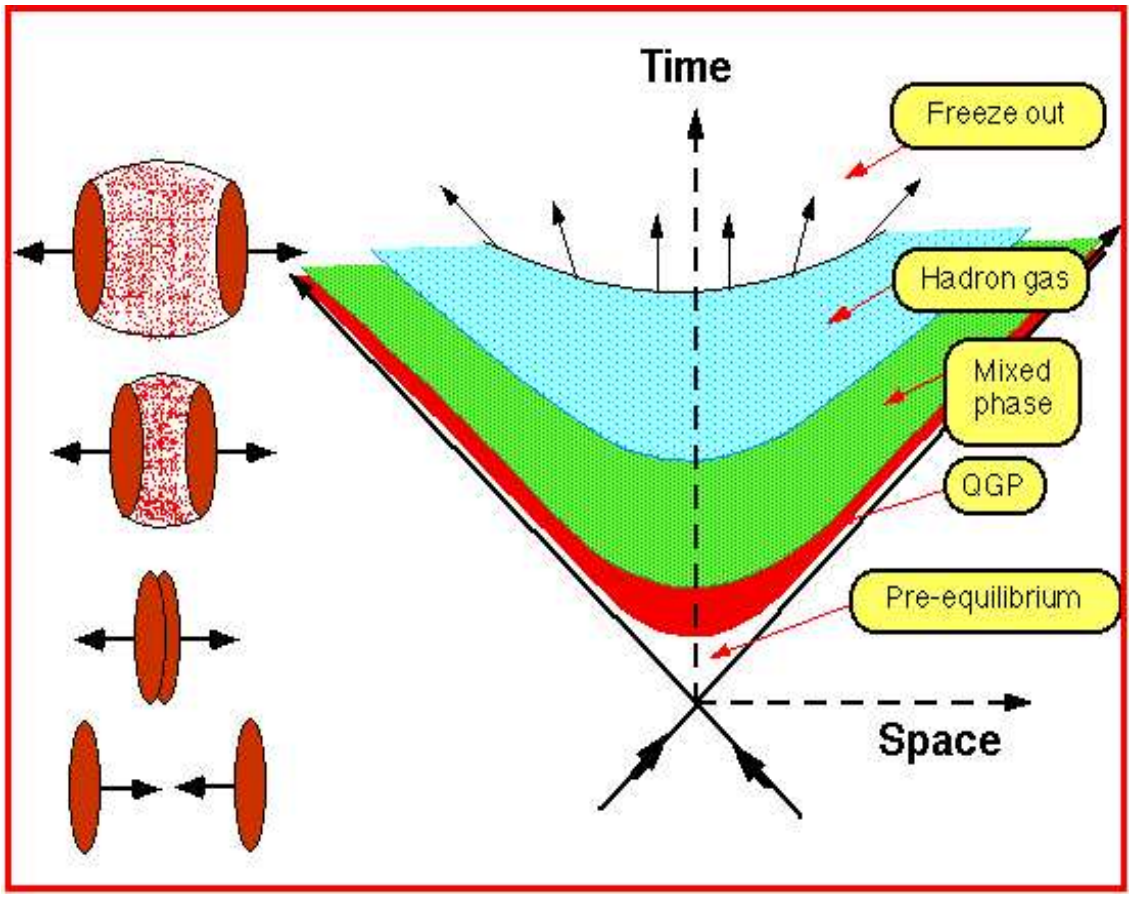

Figure 1.2: Space-time evolution of a heavy ion collision.

content of the final state particles. The relative strangeness content of these particles reflects the degree of chemical equilibration that occurred in the early stage. Similarly, the conditions at thermal freeze-out can be characterized by the bulk properties of the spectra (common velocity, thermal parameters, etc.).

1.6 Strangeness

Strangeness enhancement has long been heralded as a signal for QGP production. [10] Clearly, the valence strangeness content of normal nuclear matter is zero. When normal nuclear matter is collided at high energy, there are processes which produce particles carrying valence strangeness quarks. Pions, being the lightest mesons, are produced copiously in such collisions. This leads the way to reactions such as $\pi^0 + p \rightarrow K^+ + \Lambda$. This *associated production* occurs only for K^+ because it receives its valence u quark from the initial particle states. K^- is not made in such a reaction, because its valence $\bar{d}$ antiquark is not found in the initial state. [11] The other source of strange particles in a hadronic collision is *pair production*, where, for example, $K^{\pm}$ pairs are produced. We shall focus on the charged Kaons for this discussion, because they are the lightest (and thus most easily produced) strange hadrons and carry the majority of the strangeness content of the system. The charged Kaons, in particular, are directly observed in the STAR TPC, unlike the K^0_S and K^0_L.

We see, then, that there are two mechanisms for creating strange particles in a nuclear collision that do not require QGP formation. The relative abundance of strange particles, however, may be greatly enhanced if the source is a QGP. Clearly, in a deconfined medium, it will only be necessary to create $s\bar{s}$ pairs instead of pairs of hadrons; the energy deficit for the former is smaller. Also, the restoration of chiral symmetry will reduce the effective masses of the quark to their "bare" masses, making

$s\bar{s}$ production even more likely.

The degree of relative strangeness production is influenced by two factors, temperature and baryon density. If the temperature of the system is high, there is more energy available for producing the heavier pairs of strange particles. Increasing baryon density can also increase relative strangeness abundance. As the density of u and d quarks is high, Fermi exclusion requires that new u and d quarks be formed at higher energy levels than the ground state. This makes it energetically favorable to produce ground state s quarks instead.

In heavy ion collisions, we see that these two factors conflict. Higher collision energies mean a higher temperature for the produced particles. On the other hand, it has been observed that higher collision energies result in a decrease of net baryon content as the baryon number from the incoming nuclei is boosted farther away from midrapidity. The net effect of this balance is that the maximum degree of strangeness enhancement is reached in some moderate range of temperature and baryon density. A concrete measurement of strangeness enhancement in the final state is the Wrobleski factor defined by

$$\lambda_s \equiv \frac{2\langle s\bar{s}\rangle}{\langle u\bar{u}\rangle + \langle d\bar{d}\rangle} \,. \tag{1.1}$$

Figure 1.3 shows a plot of the T - μ_B plane with curves of constant λ_s. [12] Also shown is the chemical freeze-out curve at $\langle E\rangle/\langle N\rangle = 1$ GeV. No matter what energy density the system may have attained at earlier time, this curve should describe it reasonably well as it cools and inelastic scattering halts. Notice that the maximum Wrobleski factor along the freeze-out curve is at moderate temperature and baryon density. At the highest baryon density or temperature, the relative strangeness content is less than maximum. We shall see this clearly in the Kaon to Pion ratio as presented in

Chapter 5.

1.7 Nuclear Modification

One purpose of colliding relativistic heavy ions is to create a high energy density over an extended region of space. While such collisions accomplish this goal very well, the dynamics of nucleus-nucleus (AA) collisions are much more complex than nucleon-nucleon (NN) collisions. One can expect modification of particle momentum spectra and bulk dynamics that goes beyond a simple superposition of NN collisions. Mixed in with these nuclear effects is the promise of signals of QGP formation.

In the case that a QGP is formed, partons which undergo hard scattering in the initial collision (and would fragment into high momentum hadrons) are subject to energy loss in the colored plasma. Both radiative energy loss (bremsstrahlung) and elastic scattering would contribute, but it is believed that the former dominates. [13] Furthermore, hard scattered gluons would lose more energy than hard scattered quarks in a colored medium due their stronger interaction with that medium. This partonic energy loss would manifest itself as a suppression of *leading hadrons* in the final spectra, relative to a collision where no QGP was formed (like NN). Leading hadrons are high momentum final state particles, which carry a significant portion of the momentum from a hard-scattered parton.

As mentioned above, an AA collision has complex dynamics that may hide the partonic energy loss signature of QGP formation. One such effect is *nuclear shadowing*. This refers to the modification of parton distribution functions within nucleons that are contained in a nucleus. Such a change in the parton momentum distribution will clearly change the hadronic momentum spectra to some degree. Also important is the *Cronin effect* [14], a term that is used to describe the observed redistribution

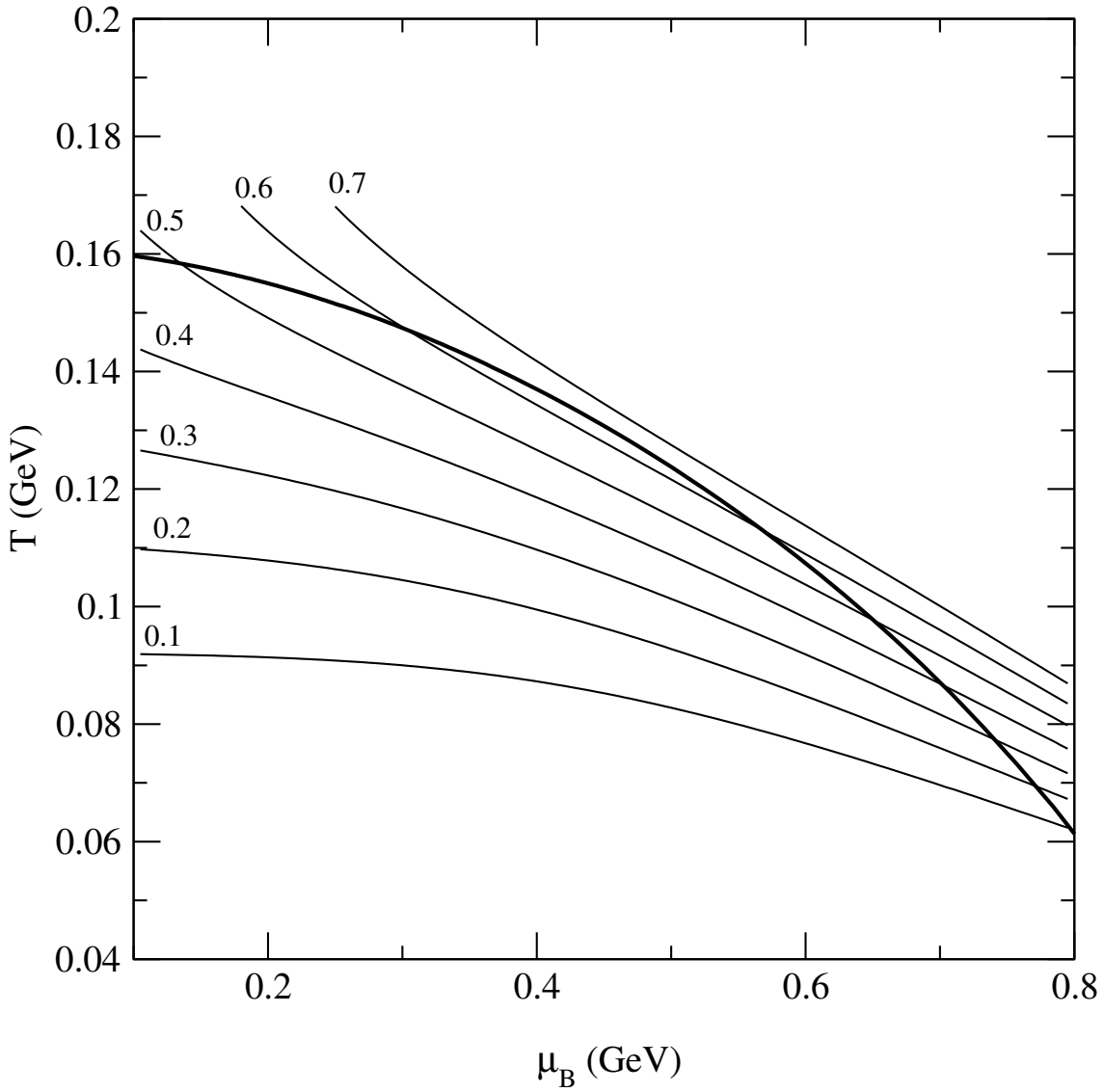

Figure 1.3: Lines of constant Wrobleski factor λ_s (for definition see text) in the T – μ_B plane (thin solid lines) together with the freeze-out curve (thick solid line)

of cross section from one p_{T} range to another in pA relative to pp collisions. Possible physical causes for this effect include broadening of the momentum spectra due to initial state multiple scattering. This broadening of the spectra causes an suppression relative to NN at lower p_{T} and an enhancement at higher p_{T}. These factors must be considered carefully in the interpretation of high p_{T} hadron suppression in AA data.

1.8 Summary

One of the main motivations of the experiments at the RHIC facility is the observation and subsequent study of a new state of nuclear matter, the QGP. The study of this new state could significantly reinforce the validity of QCD and the standard model of fundamental particles. The measurement of charged Kaons from decay topology provides the potential for examining various signatures of such a plasma, including strangeness content and high p_{T} hadron suppression.

Chapter 2

The STAR Experiment

The Solenoidal Tracker At RHIC (STAR) experiment is one of two large experiments at the Relativistic Heavy Ion Collider (RHIC) facility at Brookhaven National Lab (BNL) in Upton, New York. RHIC has 6 experimental sites, 4 of which are occupied by STAR, PHENIX, and the two smaller experiments, BRAHMS and PHOBOS. A perspective view of the STAR experiment is shown in Figure 2.1.

2.1 RHIC

RHIC accelerates heavy ions through several stages in order to deliver them to the experimental sites. The Tandem Van De Graff, AGS Booster, AGS, and RHIC ring are all crucial for producing high energy heavy ions (up to 100 A GeV).

2.1.1 Tandem Van De Graff Generator

Heavy ions are produced in the Tandem Van De Graff generator facility. One of the Tandem generators is dedicated to accelerated ion production for RHIC. The input to the Tandem is an ion source such as a high temperature gold filament, which would produce Au^{1-}. The Tandem, which develops a 15.5 MV electrostatic potential, earns its name from the fact that it accelerates ions before and after passing them through a stripper foil, which removes electrons from the incoming ions. The ions coming out of the Tandem have an energy of 1 A MeV. Gold ions produced in the Tandem are steered by magnets to extract a beam of Au^{12+}. [15]

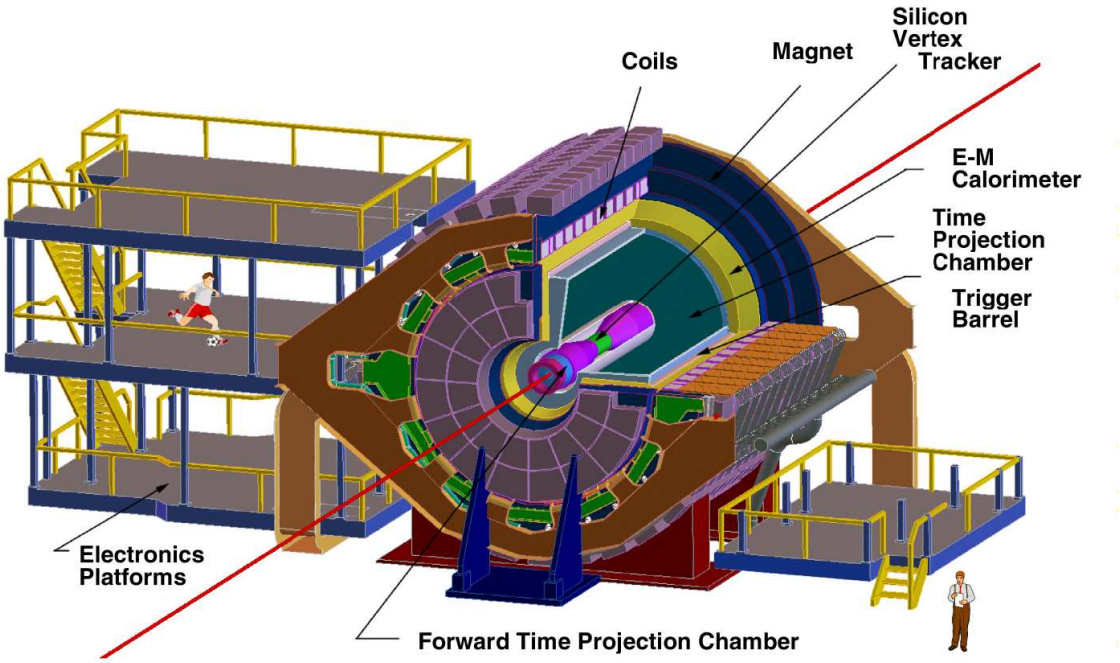

Figure 2.1: Perspective view of STAR experimental apparatus

2.1.2 AGS Booster

The next stage in the acceleration is the AGS Booster, which accelerates ions coming along the Tandem-to-Booster (TtB) line from the Tandem before delivering them to the Alternating Gradient Synchrotron (AGS). The TtB includes another stripper foil to produce Au^{31+} for injection into the Booster. The Booster is a synchrotron (which accelerates charged particles in a circular path by increasing both the magnetic field intensity and the electric field frequency) with a circumference of 202 m, 1/4 that of the AGS.

The booster is required because it has superior vacuum to the AGS. This is important because an ion beam suffers losses from two effects: electron capture and electron stripping. [16] Electron capture is the dominant effect at low energy, and electron stripping is more important at higher energies. When low energy ions are

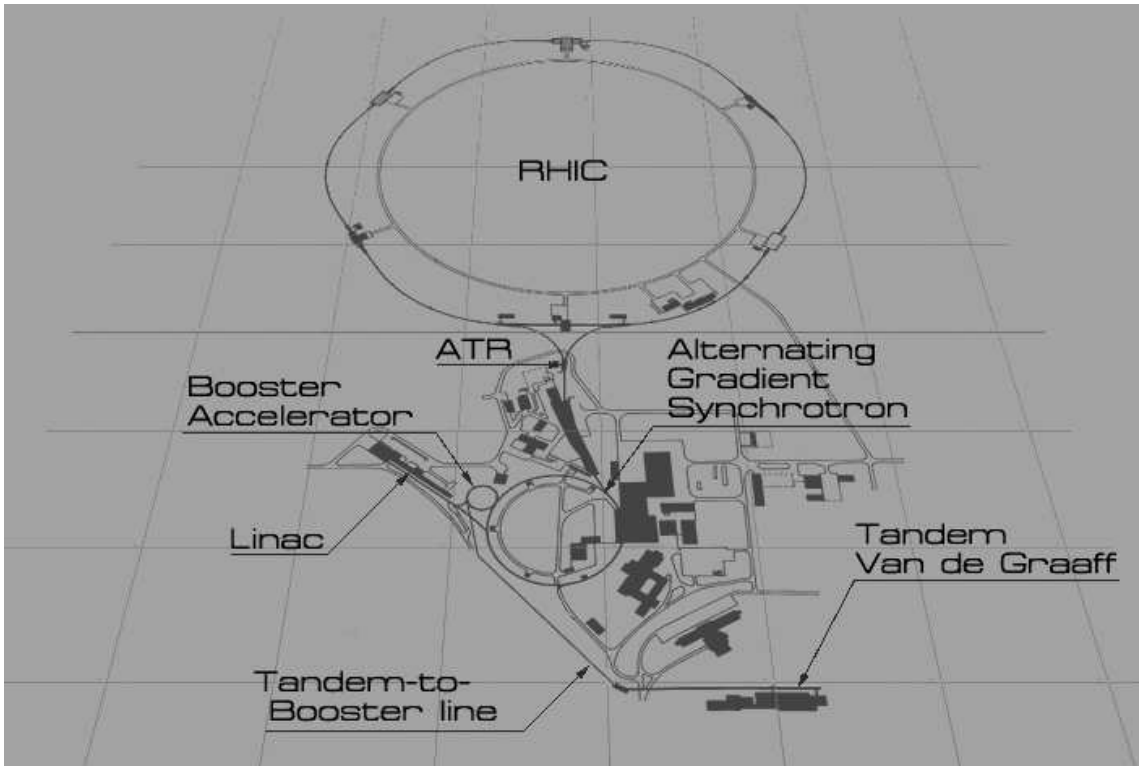

Figure 2.2: Various facilities for accelerating ions at RHIC.

injected into the Booster, the good vacuum (10^{-11} Torr) prevents significant beam loss due to electron capture from residual gas. By the time ions leave the Booster, they are in the energy regime where electron stripping dominates. On the transfer line from the Booster to the AGS, they are further stripped of their electrons. Gold, for example, is reduced to Au^{77+}, leaving only 2 electrons. High charge states have lower potential for electron stripping, so the weaker vacuum (10^{-7} Torr) of the AGS still allows good transmission of the ion beam. Without the Booster, the AGS would not be usable for ions with an atomic mass greater than 28 (silicon); it would lose too much of the incident low energy beam to electron capture. Ions exiting the booster have momenta of 100 A MeV. [15]

2.1.3 Alternating Gradient Synchrotron

The AGS itself is a synchrotron with an 807 m circumference. It, like the Booster, uses alternating quadrupole magnets to focus the beam. These quadrupoles cause a gradient in the magnetic field in the plane perpendicular to the beam direction. The net transverse magnetic field is zero at the center, so ions which are on the ideal circular path in the synchrotron are not diverted. Ions which have drifted away from the center are focused in an ellipse by the quadrupole. The subsequent quadrupole magnet is rotated by 90 degrees so that the beam is compressed along the other transverse axis. This strong (alternating) focusing technique earns the AGS its name. The AGS accelerates ions up to 9 A GeV . [15]

2.1.4 RHIC Ring

The beam next passes through AGS To RHIC (ATR) transfer line, where a filter foil strips Gold of its final two electrons to produce Au^{79+}. At this point, the ion

beam is split into bunches by switching magnets. The bunches are alternately sent down the two RHIC rings ("blue" and "yellow") in opposite directions. The final acceleration in the RHIC rings raises the energy of the nuclei to 100 A GeV for a total $\sqrt{s_{NN}}$ of 200 GeV in a collision. $\sqrt{s_{NN}}$ here refers to the center of mass energy of the collision (i.e. the total energy available for particle production) per incident nucleon pair. [15] The collider has a design luminosity of $L = 2 \times 10^{26}$ cm^{-2} s^{-1} for Au-Au collisions at this maximum energy. The circumference of the RHIC ring is 3834 m, which is chosen because it is 19/4 times that of the AGS. That is the ratio of the number of ion bunches desired in each RHIC ring (57) relative to the number in the AGS (12). This facilitates injection of ions from the AGS into the RHIC rings.

In RHIC, ion bunches are steered by magnets to cross at the 6 interaction points every 220 ns. This corresponds to a crossing rate of 4.55 MHz. Each bunch contains about 7.5×10^8 ions. The luminosity is the flux of particle pairs, i.e., the number of particle crossings per unit area per unit time and is equivalent to

$$L = f \frac{N_1 N_2}{A} , \tag{2.1}$$

where f is the frequency of bunch crossing, N_1 and N_2 are the number of particles in each intersecting bunch, and A is the transverse area of the interaction region. So the design luminosity above corresponds to a interaction area of about $A = (4.55 \times 10^6 \text{ s}^{-1})(7.5 \times 10^8)^2/(2 \times 10^{26} \text{ cm}^{-2} \text{ s}^{-1}) = 0.013 \text{ cm}^2$, or a diameter of about 1.3 mm. The total interaction rate is $L\sigma_{NN}$, where σ_{NN}, the total Au-Au cross section, is about 7.2 barn. [17] So the interaction rate is about $(2 \times 10^{26} \text{ cm}^{-2} \text{ s}^{-1})(7.2 \times 10^{-24} \text{ cm}^2) =$ 1440 Hz. [18]

2.2 STAR Magnet

Momentum determination in the STAR Time Projection Chamber (TPC) requires a strong, uniform magnetic field. The magnet strength was designed with a balance between raw field strength and homogeneity. A strong field is necessary to resolve the curvature (i.e., transverse momentum) of high momentum tracks, but various resolutions will be degraded by inhomogeneity in the field.

The magnet produces a very uniform field along the z axis over the range $0.25 < |B_z| < 0.5$ T. The non-uniformity in the radial and azimuthal directions are defined by $|\beta_{r/\phi}| \equiv |\int_{z'=210\,\mathrm{cm}}^{z}(B_{r/\phi}/B_{z'})dz'|$. Over the operating range above, the magnet maintains a uniformity $|\beta_r| \leq 2.3$ mm and $|\beta_\phi| \leq 1.0$ mm over the entire TPC volume. Weighing in at 1100 tons, the magnet also provides support for all other elements of the STAR detector. To maintain the field quality above, tolerances in the magnet structure are less than 1 mm.

One can see the structure of the magnet in Figure 2.3. It consists of 10 Main coils and two Space Trim coils, all of which are connected in series. They draw a current of more than 5000 A at the maximum field (0.5 T). The coils have an inner diameter of 5.3 m and an outer diameter of 6 m. The axial thickness of the Main coils is 0.45 m, and the Space Trim coils measure 0.23 m. To help maintain field uniformity, the Pole-tips also contain Trim Coils, which draw a total of 1330 A at maximum field. All magnet coils are made from rectangular aluminum, insulated with fiberglass and epoxy.

The magnet is water-cooled, and the internal closed-loop cooling system moves 1200 GPM through the heat-exchangers, which are cooled by an external open-loop system. The system must dissipate the 3.5 MW of resistive heat produced in the

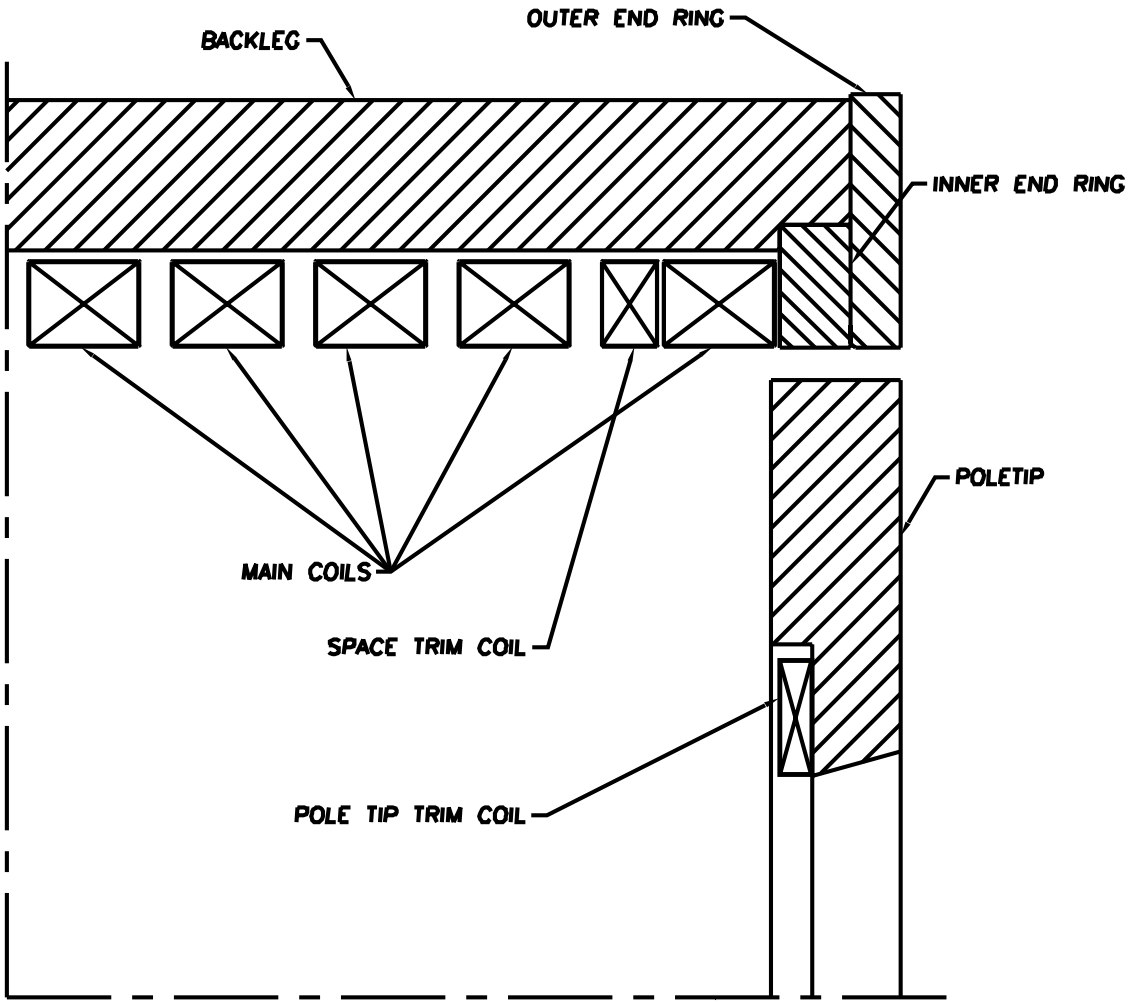

Figure 2.3: Section drawing of magnet steel and coil locations.

magnet and keep it at the normal operating temperature of 29° C. [19]

2.3 Trigger and DAQ

The STAR Data AcQuisition (DAQ) electronics are capable of reading out entire events (ion collisions) at the rate of 100 Hz. As seen above, the bunch crossing rate is about 5 MHz, so some method of detecting events and deciding which ones to read out from DAQ must be found. The actual Au-Au interaction rate is only about 1/3000 of the bunch crossing rate, so the first job of the trigger is to detect whether an interaction occurred during a bunch crossing. This is done mainly in the Level 0, 1, and 2 (L0, L1, L2) triggers. These triggers get input from the "Fast Detectors": a Central Trigger Barrel (CTB) and two Zero Degree Calorimeters (East and West ZDC). These detectors provide per-event information at the rate of 10 MHz, 5 orders of magnitude faster than the "Slow Detectors", which include tracking detectors such as the Time Projection Chamber (TPC), the Silicon Vertex Tracker (SVT), and the Ring Imaging CHerenkov detector (RICH).

The CTB consists of 4 cylindrical bands, each of which contain 60 scintillator slats. (See Figure 2.4.) It surrounds the TPC at a radius of 2 m. It covers the full azimuthal range and the pseudorapidity range $-1 < \eta < 1$. It serves to measure charged particle multiplicity. The more "central" the collision of two gold ions, the higher multiplicity we expect in the CTB. (Higher centrality corresponds to smaller impact parameter.) The ZDCs, common to all RHIC experiments, are hadronic calorimeters that use fiber optics to detect Cherenkov light from the core of the hadronic shower. They are located 18 m away on either side of the interaction region and cover a small solid angle at $\theta = 0$ and $\theta = \pi$. They are behind the dipole magnets, which steer the two RHIC beams back into the ring from the interaction region. Thus, only neutral particles

(primarily neutrons) are detected in the calorimeters. Each ZDC has 3 modules, and both ZDC signals are summed to determine if an interaction occurred. The ZDCs can be used to estimate the longitudinal position of the collision vertex by comparing the timing of the signals from the East and West modules. The least central events will have a low ZDC count because few neutrons will be liberated by the collision. The most central events will *also* have a low ZDC count because there will be few incident neutrons which are *not* involved in the collision (spectators). The ZDC counts peak at moderate centrality, where a number of neutrons are freed in the collision but do not interact strongly enough to divert them from the beam line. (See Figure 2.5.)

These fast detectors provide information to the Trigger hardware every time a bunch crossing occurs. The basic "Hadronic Minimum Bias" (minbias) trigger is an L0 trigger that simply requires coincidence of signals in both the East and West ZDCs. This is designed to collect as many events as possible while introducing little bias with respect to centrality, etc. The "Central" trigger is also a fast L0 trigger; it is designed to capture higher multiplicity events (i.e., more central collisions). It requires high counts in the CTB and low counts in the ZDCs; this maximizes the produced particles and minimizes the spectators. (Recall Figure 2.5.) For more details on the method of determining centrality bins in minimum bias events, see Chapter 5. The L0 trigger is programmed to trigger on a given number of Central and Minbias events in accordance with the data requirements of STAR. Once the conditions for an L0 trigger have been met, the various slow detectors begin digitizing their data. This takes several milliseconds, and during this time, the L1 and L2 triggers perform more comprehensive analysis of the output from the fast detectors. More complicated selections may be made, and the event may be aborted if it does not not meet the

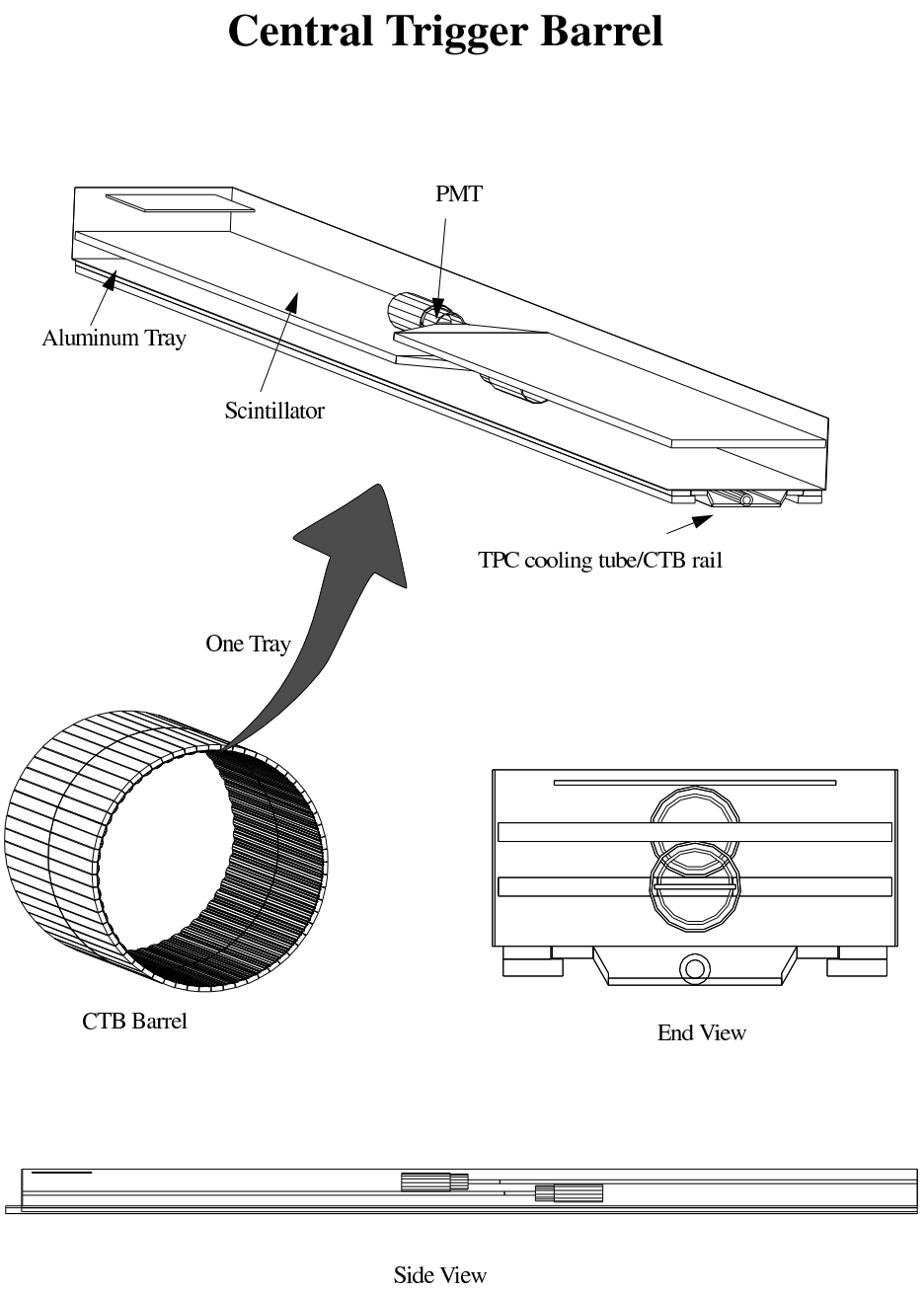

Figure 2.4: Diagram of Central Trigger Barrel

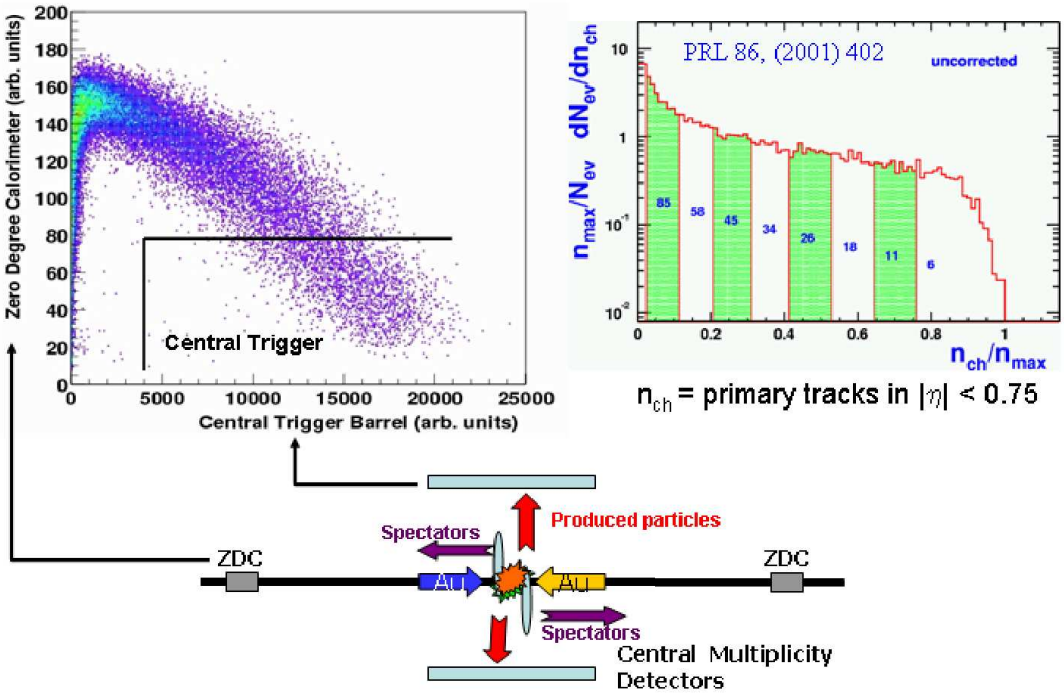

Figure 2.5: Event centrality determination. Shown are the physical interpretations of the CTB and ZDC counts, as well as a schematic of the rough central trigger on the ZDC vs. CTB plot. The n_{ch} plot shows the finer centrality selection made from minbias events.

L1 and L2 trigger requirements. This causes the slow detectors to stop digitizing and prepare for another L0 trigger. [20]

The Level 3 (L3) trigger uses data from the slow detectors once it is digitized and actually performs a fast reconstruction of the event. This means that the L3 trigger software turns the pixel information from the tracking detectors into particle trajectory information, and ultimately particle identification (PID) data. It can then accept or reject the event on more complicated triggers such as the position of the interaction vertex, the particle multiplicity, or individual particle momenta. The L3

reconstruction allows the immediate display of events in the STAR control room. [21]

2.4 TPC

The Time Projection Chamber (TPC) is the main tracking detector in STAR. It is the largest such detector in the world to date, having a diameter of 4 m and a length of 4.2 m. It provides full tracking out to $\pm$ 1.8 units of pseudorapidity and can identify particles with transverse momenta down to 100 MeV/c. As particles traverse the P10 gas (90% Argon, 10% Methane) which fills it, they ionize gas molecules. The central membrane of the TPC is held at -31 kV, and the endcaps are grounded. Joining the endcaps and central membrane are inner and outer field cages that consist of resistive rings; this steps down the voltage in a uniform manner and creates a very uniform longitudinal electric field. The electron from the ionized gas molecule drifts down to the end of the TPC until it reaches the pad planes (see Figure 2.6). The 2 pad planes each consist of 12 sectors. Each sector has 45 rows of pads. The sectors are divided into inner ($60 < R < 127$ cm) and outer ($127 < R < 189$ cm) subsectors.

The pads are in fact MultiWire Proportional Chambers (MWPCs), as shown in Figure 2.7. In normal operation the electron, which has drifted through the main TPC, is accelerated toward the anode wires until it has enough energy to ionize another gas molecule. Both electrons are accelerated, ionizing more gas molecules, and so on. Near the 20 μm anode wires, the electrons are subject to a very high electric field and are strongly accelerated. This avalanche deposits charge on the anode wire, which induces a charge in the pad below the wire; the induced current is the raw data measured by the TPC. The benefit of the Argon in P10 gas is that it is easily ionized. The Methane acts as a quencher. Gas molecules excited by the drifting electrons may revert to a ground state, emitting an energetic photon. Without a quencher,

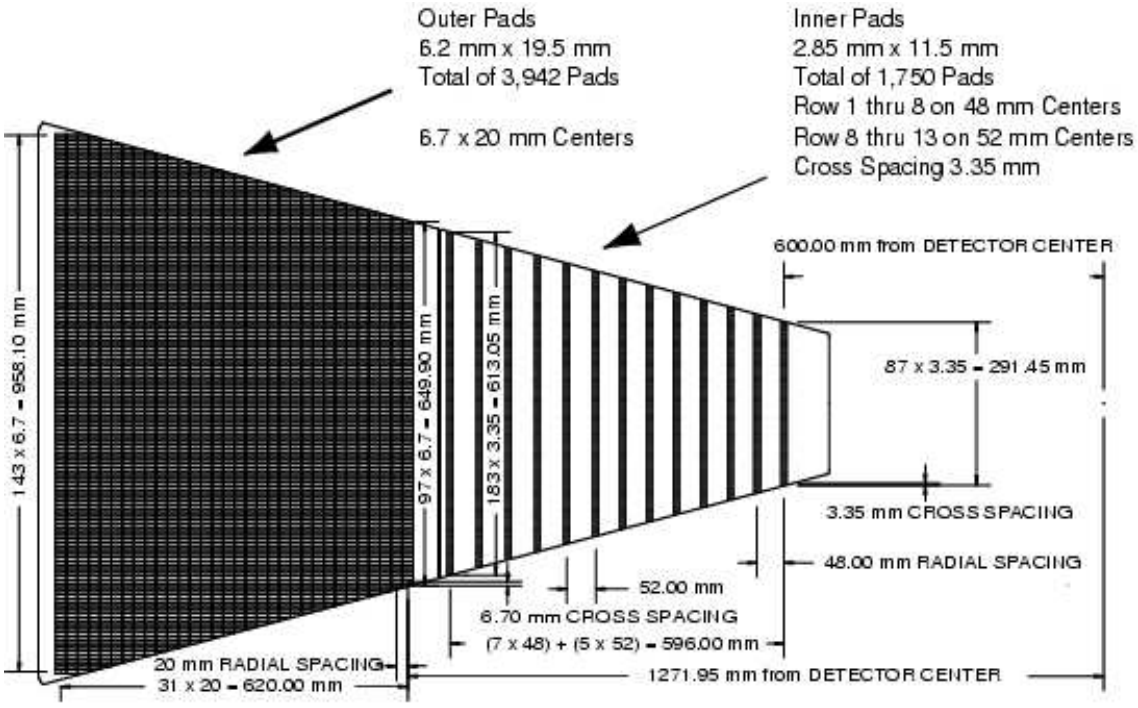

Figure 2.6: The anode pad plane, 1 sector of 24 (12 east and 12 west)

this photon would cause further ionizations in the TPC volume, leading to additional avalanches which were not caused by particles in the event. An organic quencher is a highly efficient absorber of these photons, and it ensures that the only avalanches come from primary electrons due to ionization by a particle produced in the event. The innermost set of wires in the MWPC is the gating grid, which keeps electrons from entering the avalanche region until the TPC is ready to take data and keeps positive ions from the avalanches from drifting into the TPC drift volume, where they could distort the precise electric field. An electron from a primary ionization may have to drift as much as 2 m before reaching the pad plane to be detected. The electric field in the drift volume must be as homogeneous as possible.

These MWPCs operate in proportional mode, meaning that the gain is in a moderate region where the charge deposited on the pad goes linearly with the magnitude

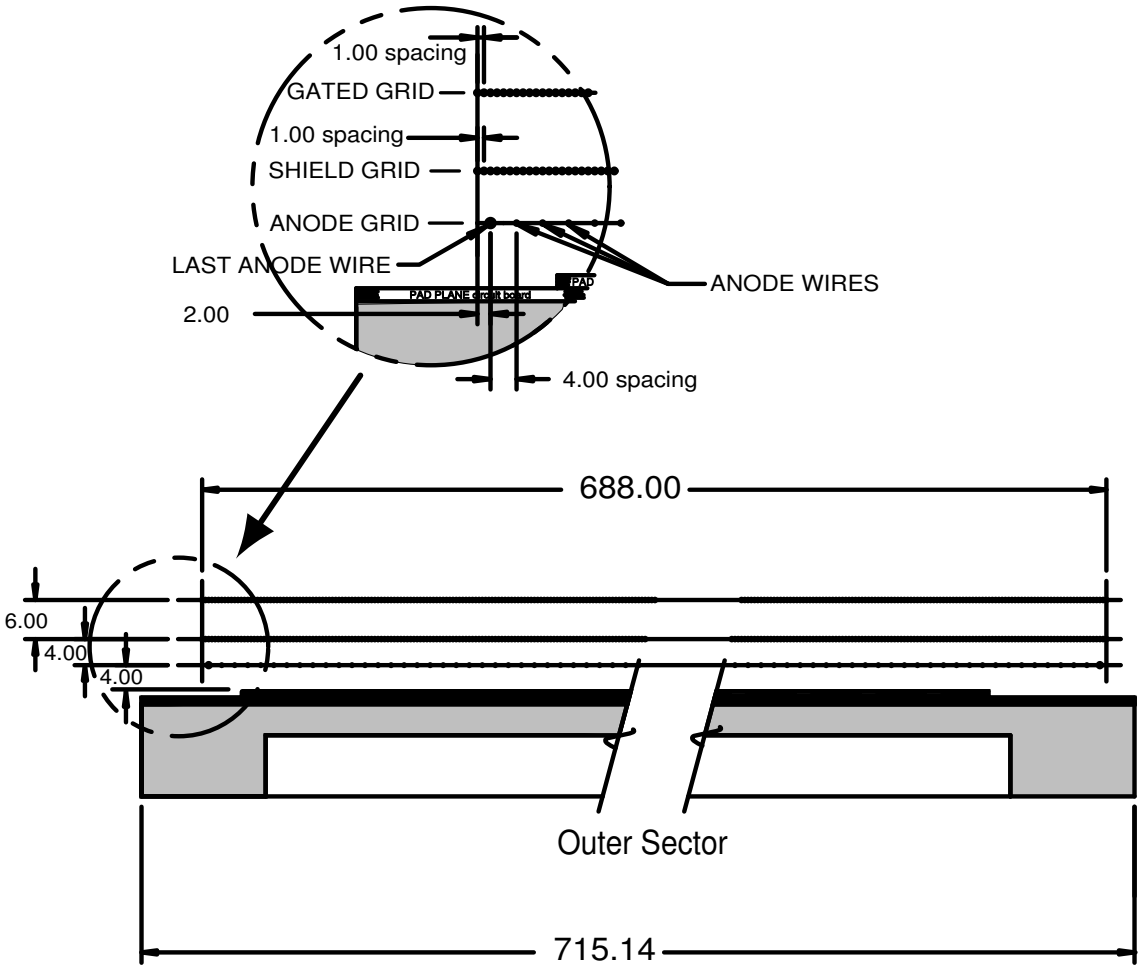

Figure 2.7: The wires in the MWPC for an outer sector pad

of the ionization produced in the drift volume. That means that the total charge deposited by an ionizing particle on the pad plane is proportional to the amount of energy loss (dE/dx) it incurred while passing through the TPC. This quantity depends mainly on the velocity of the particle (not the momentum), and so it can be used with some success to differentiate particle species in the region where the momentum does not greatly exceed the mass.

The TPC provides three dimensional data. The pad spacing along a row is 3.35 mm (Inner sector) or 6.75 mm (outer sector). The spacing of the padrows is 50

mm (inner sector) or 20 mm (outer sector). Total density is limited by electronic readout capability. The geometry above represents a balance between better energy loss (dE/dx) information in the outer sector, and better space point resolution in the inner sector. The high pad density along the inner sector padrows places a limitation on the number of rows which can be served by the readout electronics; thus the density of padrows is lower here. The z position is determined by the time the primary electrons take to drift from the original ionization point. Data is recorded in up to 512 "time buckets", each corresponding to about 100 ns or 0.5 cm in z (based on the drift velocity determined by the electric field; 5.45 cm/μs is a typical value). The spatial information can have higher resolution than the spacing of pads or time buckets. One may fit a Gaussian to adjacent pads or time buckets to find the center of the distribution. Resolution along the padrow is about 0.4 mm in the inner sector and 0.6 mm in the outer sector. That along the drift direction is 0.9 mm in the inner sector and 1.2 mm in the outer. These are for particle trajectories which cross the padrow at right angles. Polar or azimuthal inclination will increase the uncertainty in the drift and padrow directions, respectively, because the distribution of charge at the anode planes will be spread out over several pads or time buckets. The maximum resolution in the radial direction is fixed at the padrow width because no finer position information is available. There is an inherent uncertainty in position because of the diffusion of a cloud of electrons produced by an ionizing particle as it drifts through the TPC to the pad plane. The transverse diffusion is about 3.3 mm for electrons which drift the maximum 210 cm. The longitudinal diffusion is about 5.2 mm. [22]

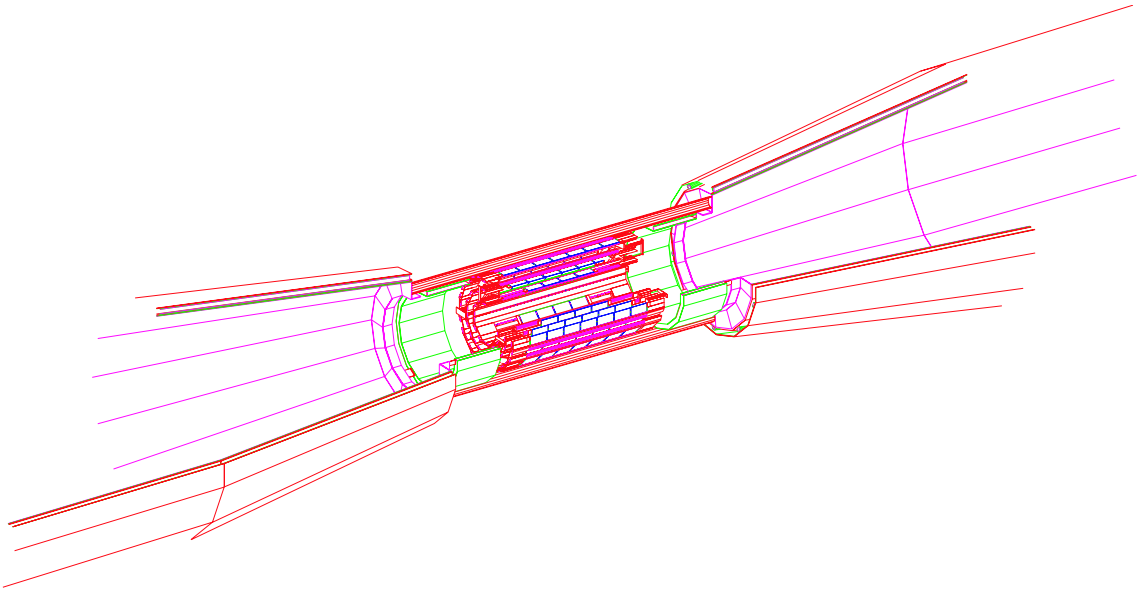

Figure 2.8: The Silicon Vertex Tracker

2.5 SVT

The Silicon Vertex Tracker (SVT) is located near the beam line at mid-rapidity. It is designed to improve the TPC tracking in several ways; it improves the primary vertex resolution, track separation resolution, and energy loss measurement for particle identification. It also adds new capability such as the reconstruction of decays of short-lived particles like strange and multi-strange baryons because it provides secondary vertexing capability very close to the collision vertex. Being at a smaller radius, it also allows the measurement of lower momentum particles by reconstructing particle trajectories solely with the SVT.

The SVT, shown in Figure 2.8, consists of 3 concentric barrels, each covering approximately the same pseudorapidity (-1 $< \eta <$ 1). Each barrel consists of a number (8, 12, or 16 for barrels 1, 2, and 3, respectively) of ladders, which extend in the axial direction, and each ladder contains a number of Silicon Drift Detector (SDD)

wafers (4, 6, or 7 for barrels 1, 2, or 3). Each 63 mm square SDD wafer is effectively a solid state drift chamber. It is made of an n-type Silicon semiconductor 280 μm thick, and several p-type cathode strips (located every 135 μm in the drift direction) are placed on the top and bottom of each wafer. When negative voltage is applied to the cathodes, free electrons caused by ionization from energetic particles passing through the wafer will be attracted to n-type anodes at the edge of the wafers. The anodes are at a 250 μm pitch (perpendicular to the drift direction). The negatively charged p-type cathodes on the top and bottom surfaces constrain the electrons produced through ionization to the center of the wafer.

The cathode pitch maintains a uniform electric field, allowing the determination of position in the drift direction by a measurement of drift time. The overall position resolution of the SVT is 20 μm, much more precise than that of the TPC. [23]

Chapter 3

Event Reconstruction

As impressive as the data collection abilities of the STAR detector are, most physics analysis requires a higher level of abstraction than the "raw" data provided by the DAQ electronics. This process of event reconstruction takes the raw event data and condenses it into information about the particles produced in the collision.

In STAR, this reconstruction software is invoked in a sequential arrangement called a Chain. The Chain consists of several Makers; each Maker is an independent software component which processes the event data. Subsequent Makers may (and usually do) depend on information added to the event by previous Makers.

We will cover in depth the process for reconstruction within the main tracking detector, the TPC. Many elements are similar when considering the SVT or FTPC, but some differences exist due to different track density, detector orientations, and readout capability.

3.1 Cluster Finding

Cluster finding is the process of grouping the raw event data into groups of adjacent charge deposition. The module responsible is called TCL. This is done in the TPC local X-Z plane, i.e. in the plane defined by the drift and padrow directions. Clusters are formed by finding all adjacent non-zero ADC values in the padrow-drift plane. These clusters of charge induced on the pads may be from the ionization track of one or more charged particles. See Figure 3.1.

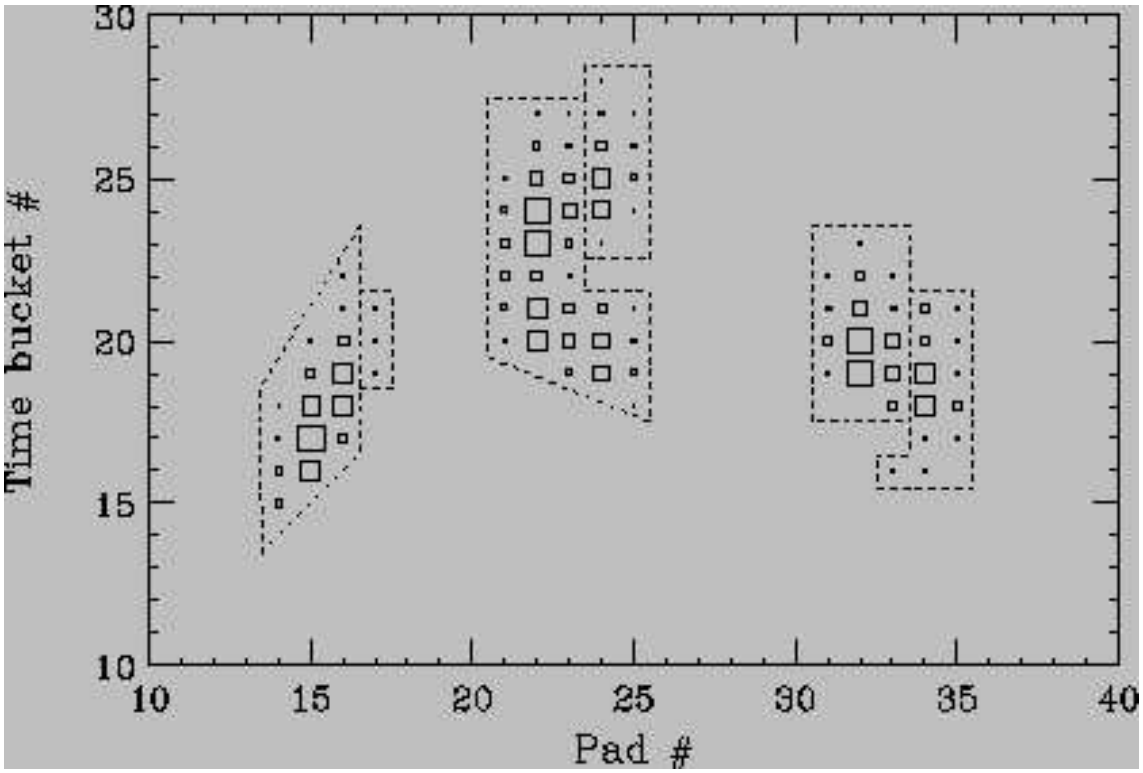

Figure 3.1: ADC values in the X-Z plane. TCL has found 3 separate clusters.

3.2 Hit Finding

As mentioned, each X-Z cluster may contain several "hits", where each hit corresponds to the charge from one particle's ionization track crossing that padrow. Hit finding consists of deconvoluting these clusters into individual hits and then finding the center of the hit based on the charge distribution.

3.2.1 Deconvolution

First, a gross cut is done on the width of the cluster in X and Z. Even if a narrow cluster contains multiple hits, it is unlikely that the deconvolution algorithm, which is processor intensive, will be able to separate them. This first cut saves a great deal of CPU time.

Clusters having a sufficient spread in the padrow and time direction are subjected to a mountain-finding search. Local maxima are identified, and the "valleys" between these maxima are examined to determine if there is significant separation between the two peaks. Figure 3.2 shows potential hits identified by the deconvolution routine.

After hits are identified, they are fit to a centroid in X to determine their centers. Recall that the pad geometry is chosen so that the charge from one ionization trail will be directed almost completely onto 3 pads per row. Assuming a Gaussian distribution, the center can be arrived at analytically using the 3 largest pad ADC values:

$$x = \frac{\sigma^2}{2w} \ln \frac{h_3}{h_1} \,, \tag{3.1}$$

where w is the pad pitch, $h_{1,2,3}$ are the ADC counts on 3 adjacent pads, and the width of the Gaussian is found by

$$\sigma^2 = \frac{w^2}{\ln \frac{h_2^2}{(h_1 h_3)}} \,. \tag{3.2}$$

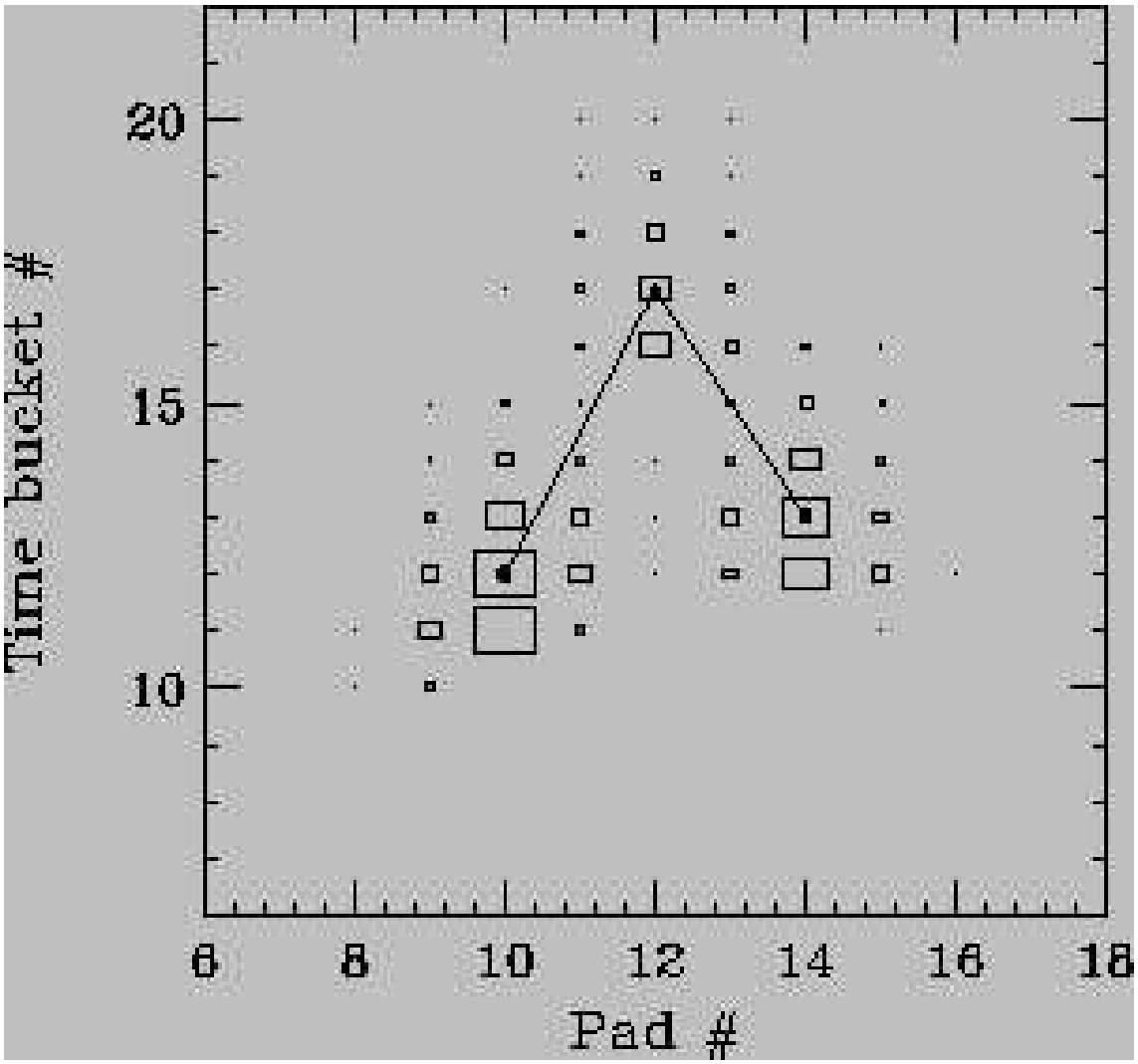

Figure 3.2: The mountain-finding routine has identified 3 candidate hits.

The Z coordinate is found in a similar way, but the relationship between Z and drift time (the quantity which the TPC actually records) is very sensitive to the drift velocity in the TPC and the absolute zero of the timing information. This means that great care must be taken to determine both the correct offset for the time coordinate, as well as the scaling with Z (i.e., drift velocity). [22]

3.3 Global Tracking

Tracking is the process of combining reconstructed hits into tracks, which represent the path of a charged particle through the detector. A charged particle that moves through a uniform magnetic field and suffers no energy loss will have a perfectly helical trajectory. The parameterization of this helix in STAR is defined by the beginning of the helix in the transverse plane (x_0, y_0), the phase (Φ_0), the dip angle (λ), the sense of rotation (h) , and the curvature (k). The phase, Φ_0, is defined as the angle in the transverse plane of the helix starting point relative to the helix center (x_c, y_c). The dip angle measures the deflection of a track from a purely transverse trajectory and is defined by

$$\tan\lambda = \frac{p_z}{p_{\mathrm{T}}} \,. \tag{3.3}$$

Here, $p_{\mathrm{T}} = p\cos\theta$ is the transverse momentum. The sense of rotation does not affect the shape of the helix, only the direction in which the particle is moving (forward or back). The curvature (equal to the inverse of the helix radius) is proportional to the ratio of the magnetic field to the track's transverse momentum:

$$k = K\frac{|ZB|}{p_{\mathrm{T}}} = \frac{1}{R} \,, \tag{3.4}$$

where K is a constant depending on the units used. For B in Tesla, p_{T} in GeV/c, $Z = q/e$ as integer charge, and R in cm, we have $K = 0.00299$ GeV/c/(T cm). Using

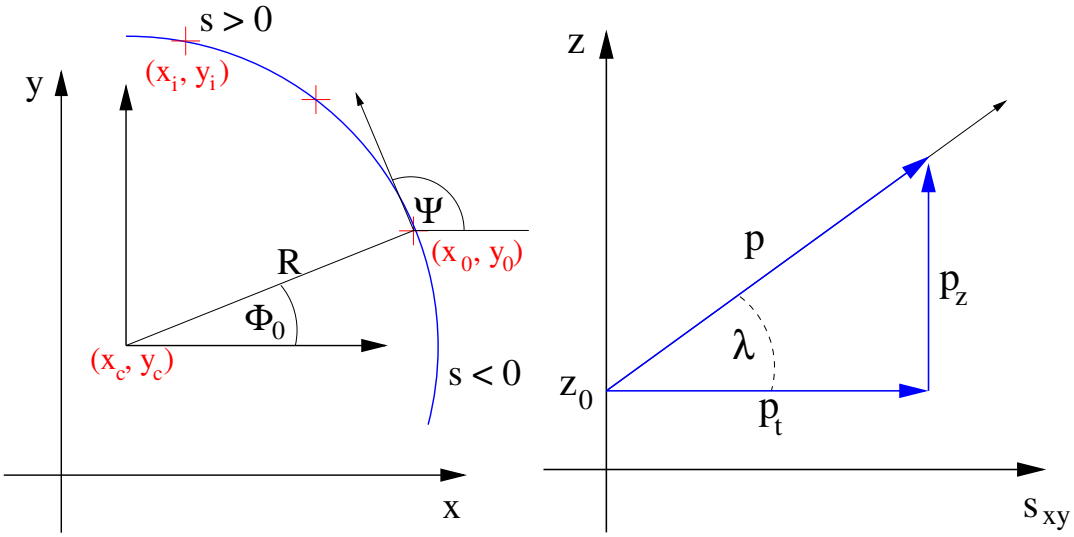

Figure 3.3: The independent (and dependent) helix fit parameters.

these 6 parameters, the helix is described by these parametric equations in terms of the path length s:

$$x = x_0 + \frac{1}{k}(\cos(\Phi_0 - hks\cos\lambda) - \cos\Phi_0) \tag{3.5}$$

$$y = y_0 + \frac{1}{k}(\sin(\Phi_0 - hks\cos\lambda) - \sin\Phi_0) \tag{3.6}$$

$$z = z_0 + s\sin\lambda\ . \tag{3.7}$$

Note that the quantity z_0 is not a free parameter. It is specified completely by the 6 independent parameters.

To begin the process of tracking, a seed for the track must be found. The seed is simply a short series of hits which lie close in solid angle. The most efficient place to look for seeds is the outer padrows of each sector, where the hit density is lowest. Track segments are then found starting with these seeds by recursively extending each segment to collect new hits. After segment finding is done, the tracking software attempts to merge any segments which are so close in phase space that they are

probably from the same particle. This helps eliminate so-called "split tracks", which result when 2 tracks are reconstructed for a single physical particle. The last step in global tracking is to do a Kalman refit. This does not find tracks, only refines the fit parameters using the Kalman method, which takes into account energy loss and multiple scattering between each hit on the track and updates the track parameters at each step.

3.4 Vertex Finding

The tracks above are found simply by connecting points in the TPC. Those tracks which originate from the collision vertex may be refined by determining the position of the interaction point. This primary vertex (as opposed to "secondary" vertices, which are the result of particle decays or other isolated processes) is found using the global tracks above. Each global track is extrapolated to the beam-line (the central axis of the TPC), and the Z bin containing the maximum density of tracks is chosen as a seed for the primary vertex.

Once the seed is found, an iterative process begins. The Distance of Closest Approach (DCA) of each global track to the primary vertex candidate is calculated. Tracks with DCA greater than a certain distance are eliminated, and the vertex candidate is refined by minimizing the DCA of the remaining tracks. This process converges quickly and is only repeated 3 times.

3.5 Primary Tracking

Once the primary vertex is known, tracks which are assumed to come from the interaction point may be refined by including the vertex in the fit. Tracks that have a DCA of more than 3 cm to the primary vertex do not go through a refit. This refit

also uses the Kalman method. Tracks whose quality measure (χ^2) deteriorate with the inclusion of the primary vertex are removed from consideration. Those which improve with its inclusion are kept as primary tracks, and their fit parameters are updated accordingly.

3.6 Particle Identification Using dE/dx

As mentioned earlier, the energy deposited by a particle (as reflected by the number of ionizations it causes) in the TPC is dependent on the particle's velocity. Since a particle's momentum (per charge, p/Z) is known well from tracking, one may plot the dE/dx, which is proportional to the charge induced on the pad planes, as a function of particle momentum. Low momentum particles with different masses but the same momentum will have different velocity, and so different particle species will show in bands on the dE/dx vs momentum plot.

Notice how in Figure 3.4 the lighter particles flatten out at much lower momenta. The lighter the particle, the faster β approaches 1 for a given momentum. This gives better dE/dx particle identification at high momentum for heavier particles. Pions and Kaons may be identified up to momenta of about 600 MeV/c, while Protons may be identified to 1.2 GeV/c .

3.7 Charged Kaon Identification Using Kinks

The relatively low momentum capability of the dE/dx identification of charged Kaons is one of the principal reasons for exploring other PID methods. The focus of this dissertation is on Kaons identified by their decay topology. The method described herein was previously applied to the $\sqrt{s_{NN}} = 130$ GeV Au-Au data. [24] The dominant charged Kaon decays are $K^+ \rightarrow \mu^+\nu_\mu$ (63.5%) and $K^+ \rightarrow \pi^+\pi^0$

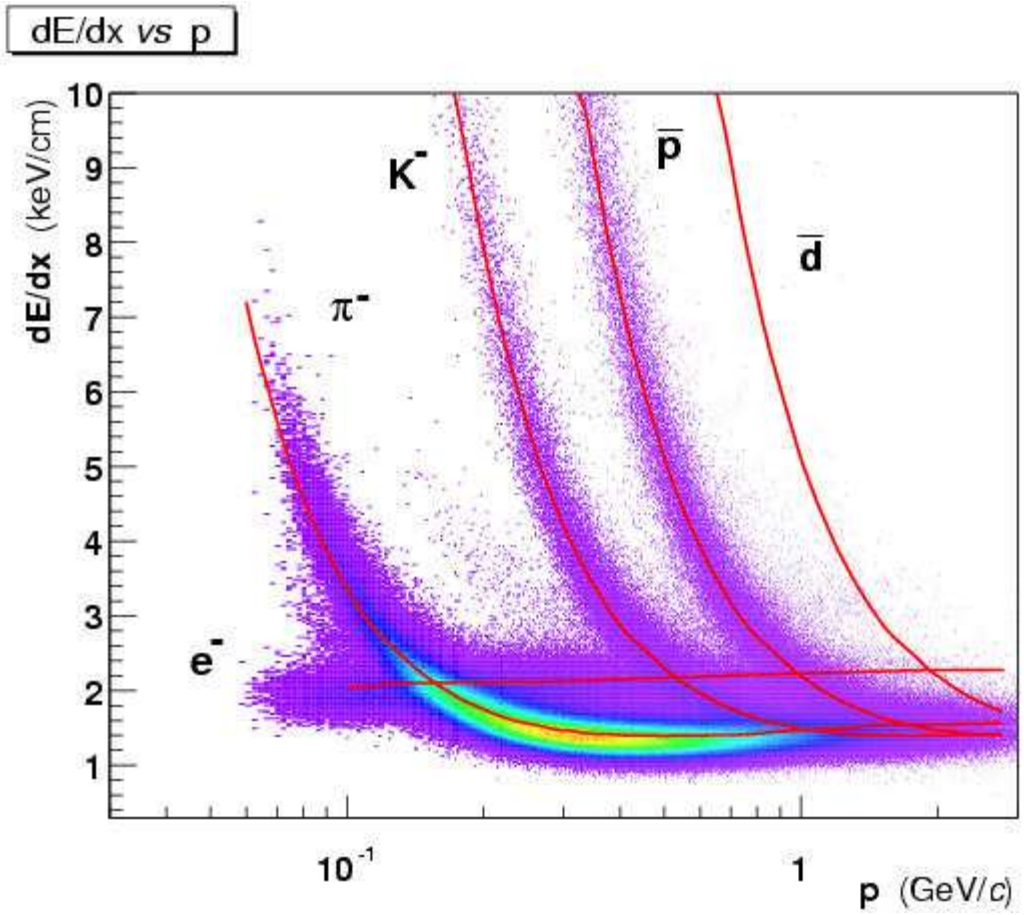

Figure 3.4: Particle identification through dE/dx.

(21.2%). Both of these modes are characterized by a single-pronged decay topology (or "kink") in the TPC. The neutral daughter is not found, and the track appears to instantaneously change direction. A kink candidate is shown in Figure 3.5.

As kink finding is a secondary vertex search, it must come after track finding in the reconstruction chain. The kink finding Maker in the chain simply creates pairs of tracks which meet at a vertex, with no physics cuts. Only the fiducial region 133 cm $<$ R $<$ 179 cm is searched for kinks, because that is in the middle of the densely instrumented outer TPC sub-sectors. This dense space point information aids in pattern recognition. First, all global tracks are searched for candidate parent and daughter tracks that end or begin in the kink fiducial volume, respectively. A number of geometry cuts are chosen to maintain a balance between preserving signal and rejecting background. To remain a parent candidate, a track must have a (3-dimensional) DCA to the primary vertex of less than 2 cm. Daughter candidates, conversely, must have a DCA of more than 2 cm. The charge of a candidate parent and its daughter must be the same, of course. The parent track must end within 14 cm in the transverse plane and 20 cm in z of the beginning of the daughter. If these conditions are met, a mathematical intersection (or solution of closest approach) is found between the parent and daughter helices in the transverse plane. The extrapolated tracks must be no more than 2 cm apart in z at this point. Next, the full 3D DCA between the tracks is found; this must be no more than 0.5 cm. If so, the intersection point is considered as a kink vertex candidate. The last point on the parent and the first point on the daughter must each be within 14 cm in the transverse plane and 20 cm in z of this newly found kink vertex. Finally, the angle between these two tracks must be greater than 1°. Tracking resolution below this angle calls into question whether there are

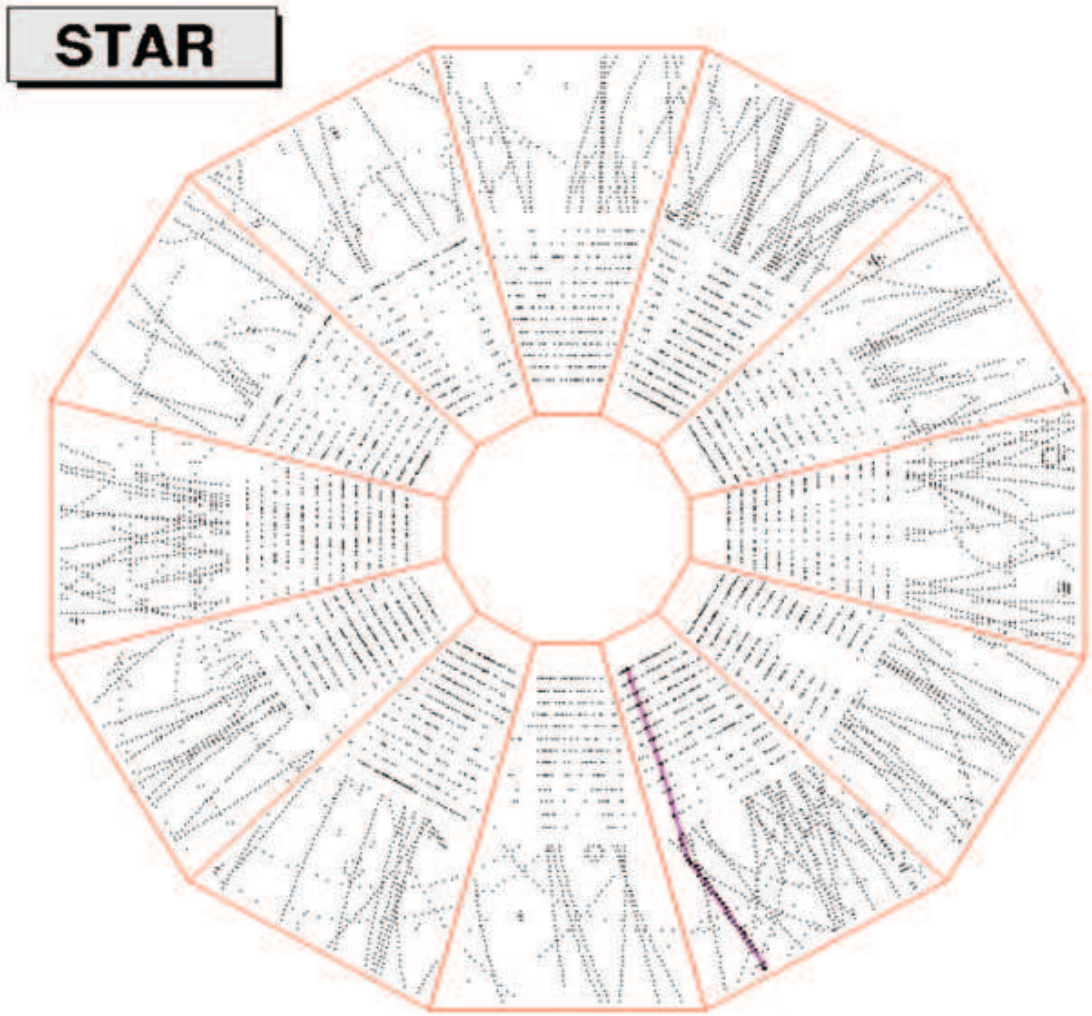

Figure 3.5: A "kink" or charged Kaon decay candidate.

Fiducial volume	$\in$ (133 cm, 179 cm)
Parent DCA to event vertex	$>$ 2 cm
Daughter DCA to event vertex	$<$ 2 cm
Parent p_{T}	$>$ 200 MeV/c
Daughter p_{T}	$>$ 100 MeV/c
Daughter charge	= Parent charge
XY distance between last parent and first daughter points	$<$ 14 cm
Z distance between last parent and first daughter points	$<$ 20 cm
Z distance between parent and daughter projections to kink vertex	$<$ 2 cm
Decay angle	$>$ 1°
Parent-daughter DCA	$<$ 0.5 cm
XY distance between kink vertex and last parent point	$<$ 14 cm
Z distance between kink vertex and last parent point	$<$ 20 cm
XY distance between kink vertex and first daughter point	$<$ 14 cm
Z distance between kink vertex and first daughter point	$<$ 20 cm

Table 3.1: Online reconstruction cuts for kink decays.

really two particles or one track that was split in reconstruction. For a summary of these cuts, please see Table 3.1

Chapter 4

Data Analysis

The kinks, or Kaon candidates, found during reconstruction are simply pairs of tracks which appear to share a common terminus within some fiducial volume. These kinks can come from three different sources. First, they may be actual one-pronged charged Kaon decays ("signal"). Secondly, they may be from another real physical process such as a Pion decay or inelastic hadronic scattering; we refer to this as "correlated background". Lastly, they may not be tied to a physical process at all. This last class includes the pairing of two random tracks, the splitting of one physical track into two reconstructed tracks, and a few rarer cases. We refer to them collectively as "combinatorial background". In this chapter, we shall discuss the tools and techniques used to eliminate the correlated and combinatorial background from the kink population while preserving a maximum of Kaon signal.

4.1 Simulation

One of the most powerful tools in our workshop is STAR simulation software. These packages allow the simulation of entire Au-Au collisions and estimate the response of the STAR detector to those collisions. Such information is invaluable in determining the composition of the background and finding ways to reduce it. It is also necessary for the estimation of the detector efficiency (the percentage of original yield which is reconstructed); no estimate could be made of actual particle yields (as

opposed to raw yields) without this feedback. One may also use the results of simulation to tune the reconstruction software, improving its efficiency. Simulation can be depended on to do some things perfectly, such as reproducing the known lifetimes of common particles. Other things, such as the net response of the STAR detector to collisions, are much more complex and must be viewed as approximations. When using simulation, it is important to constantly compare the results to data. Any discrepancies indicate areas where simulation may not be trusted without question.

4.1.1 Simulation Tools

STAR simulation software may be broken down into event generators, which simulate the collision of heavy ions and the particles produced, material simulators, which simulate the effect of the detector material on the passage of particles, and detector response simulators, which simulate how the detector responds to particle signatures. A fourth tool used in simulation is the Association maker; it provides functionality for comparing the input Monte Carlo (MC) particles and the reconstructed tracks. These four elements are detailed in the following sections

HIJING

HIJING (Heavy Ion Jet INteraction Generator) is a Monte Carlo event generator that is widely used in the study of high energy pp, pA, and AA collisions. It is based on QCD-inspired models for multiple jet production and incorporates mechanisms such as multiple mini-jet production, soft excitation, nuclear shadowing of parton distribution functions, and jet interactions in dense hadronic matter. It has been well tested against data from many high energy and heavy ion experiments and has been chosen by STAR as its main event generator. HIJING is very well established

in the community, and a discussion of its inner workings goes beyond the scope of this dissertation. [25]

GEANT

GEANT is a software tool for 1) representing the materials used to construct a detector system and the fields present in that system, and 2) simulating the effect of this matter and these fields on particles as they pass through it. For example, GEANT simulates energy loss due to ionization, the effects of multiple Coulomb scattering, and hadronic scattering. The framework for running GEANT in STAR is called GSTAR, and it includes a very detailed rendering of all material in the STAR detector from the beam pipe to the EMC, as well as a full map of the magnetic field. Different geometry libraries are available to describe the STAR detector at different stages of its development based upon what subsystems were installed at the time. GEANT can take events (i.e. a list of produced particles with their kinematic information) from HIJING as input and propagate them through STAR. The input need not be a full HIJING event; it may be a list of particles and 3-momenta from any source.

TPC Response Simulator (TRS)

TRS is the software used in STAR to simulate the response of the TPC to the passage of charged particles. Once the trajectories of simulated particles are known from GEANT, TRS takes over the simulation chain. The drifting of electrons from the ionized gas down to the pad planes, showers near the anode wires, the response of the pad plane, and more, are simulated in this intricate package. Everything necessary to generate the raw DAQ signals, analogous to those produced in a real event, is simulated. The output of the simulation chain after TRS is equivalent to what is

read out as a raw event from the STAR detector, and this output may be passed to the standard reconstruction software for cluster finding, hit finding, and tracking.

Association

The data coming out of the reconstruction ("reco") chain after simulation is richer than that coming out of a real event. It still contains information on the MC particles that were initially produced in the collision. It is very useful to draw relationships between the input MC particles and the final reco tracks. This is done on the level of hit comparison. The hits produced by a MC particle are known in TRS, where those hits are initially constructed. If a reco track has a requisite number of hits in common with a MC track, the two are "associated"; this step comes after track finding/fitting in the reco chain. This association information is available to offline analysis software.

The Association Maker also performs secondary vertex association, which is very useful for kink analysis. If a reco kink's parent track is associated with an MC track whose daughter is associated with that same reco kink's daughter track, then an association is made between that reco kink and the MC vertex. That vertex could represent signal or correlated background, but that is easily determined by checking the MC process for the vertex and the identity of the MC parent.

4.1.2 Modes of operation

The simulation tools above may be used in different modes. First, they may be used to simulate entire collisions. Secondly, they may be used to embed simulated tracks (which have passed through GEANT and TRS) in a real event. The two methods are appropriate for different studies, as discussed below

MC Events

In this mode, entire ion collisions are simulated in HIJING and passed through GEANT, TRS, the reco chain, and the association maker. This provides high statistics of reconstructed particles with known identity. For kink analysis, this is important when understanding the combinatorial and correlated backgrounds. Kinks which are associated with MC Kaon decays are easily tagged as signal, those which are associated with other MC vertexes are correlated background, and those which are not associated with any MC vertex are pure combinatorial background.

Embedding

In embedding, one wishes to have the benefits of association between reco tracks and MC particles, but in an environment as close as possible to a real STAR event. It is a concern, for example, that efficiency might not be well reproduced in reconstructing a full MC event from HIJING. The solution is to embed MC tracks into a real STAR event. For kink analysis, for example, we can embed only charged Kaons which decay in the fiducial volume. Furthermore, we can ask that the multiplicity of these Kaons be a few percent of the total event multiplicity. This is much higher than found in a real event, where charged Kaons make up about a tenth of a percent of the total multiplicity, but it is not so high as to significantly affect the realistic environment provided by the STAR event.

Embedding is particularly useful for studying efficiency and acceptance. These are factors which represent what percentage of all produced charged Kaons we reconstruct. Acceptance is defined as the ratio of all charged Kaons decaying in the fiducial volume to all charged Kaons which are produced in an event. In terms of

embedding, this is

$$Acceptance \equiv \frac{\#\text{ of MC Kaons decayed by GEANT in fiducial volume}}{\#\text{ of MC Kaons given to GEANT as input}} . \tag{4.1}$$

This factor could, in theory, be calculated. It would require knowledge of the lifetime distribution, which is well known, and an estimate of the effect of the inter-sector boundaries on the acceptance. In practice, it is simpler and more accurate to get this factor from embedding.

The efficiency factor is a measure of how well the STAR detector and software are able to reconstruct particles which decay in the fiducial. It is the ratio of all reconstructed Kaons to all Kaons decaying in the fiducial. In other words, it is

$$Efficiency \equiv \frac{\#\text{ of reconstructed MC Kaons passing kink analysis cuts}}{\#\text{ of MC Kaons decayed by GEANT in fiducial volume}} . \tag{4.2}$$

The numerator counts only kinks which pass all the analysis cuts designed to improve the signal to background ratio. These correction factors as found for the kink analysis will be discussed in the following section.

A summary of the differences in the reconstruction software chain between data and simulation are shown in Figure 4.1.

4.2 Corrections

The sample of Kaons we reconstruct with the kink method is very different than the population produced in the collision. First, the STAR detector does not cover all of space; this means that not all charged Kaons will decay within the fiducial volume of the detector. This, as we mentioned above, is called acceptance. Secondly, not all Kaons decaying in the fiducial are reconstructed; this is efficiency. Lastly, not all kinks which pass the analysis cuts are really Kaons; they may be combinatorial or correlated background.

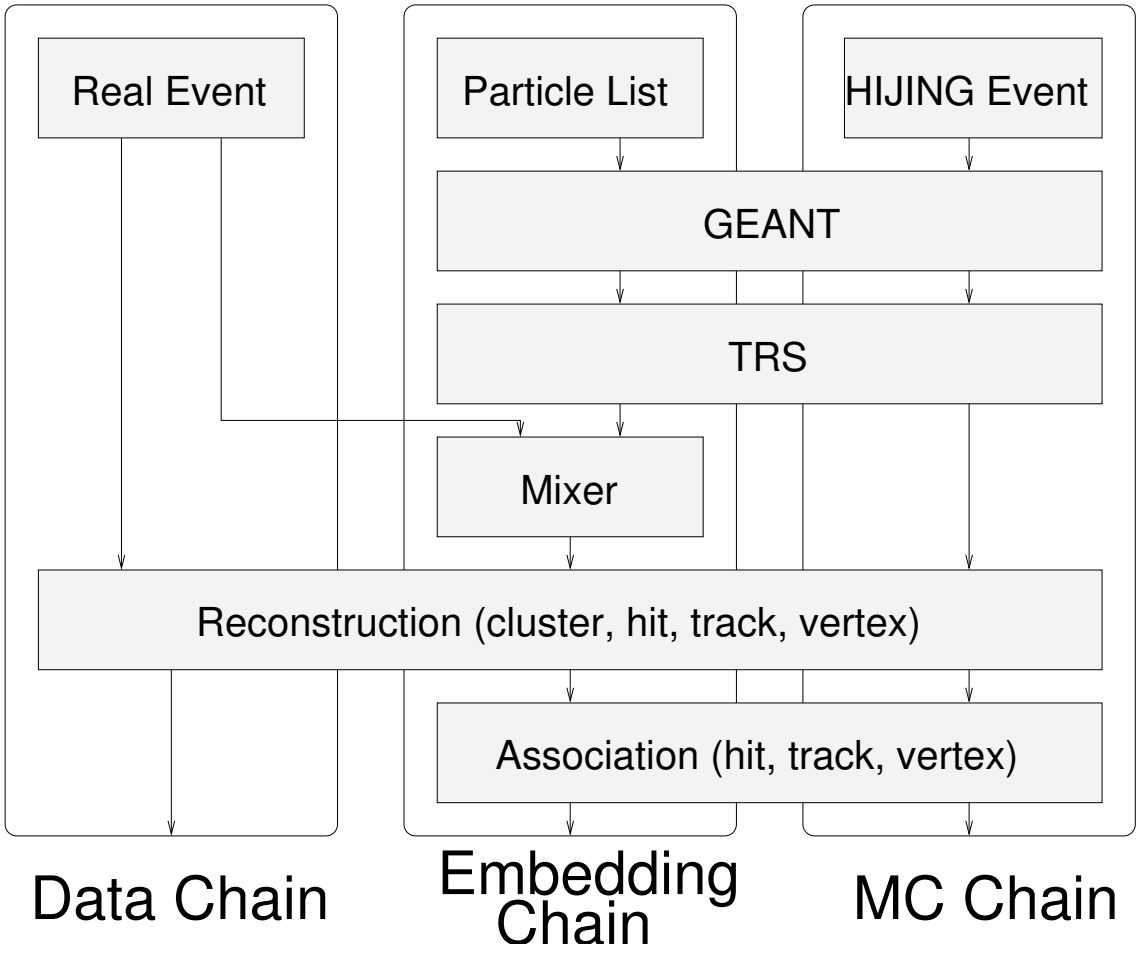

Figure 4.1: The three main configurations of the STAR software chain.

In the following sections, we explore the necessary correction factors for each case above. Since our principal goal in this analysis is the spectra of charged Kaons, these correction factors must be determined as a function of the quantity of interest (m_{T}, p_{T}, etc.)

4.2.1 Acceptance

As mentioned above, this factor may be estimated with simple calculations or by studying embedded Kaons. The latter is more thorough and accurate, but it is interesting to examine both approaches as a cross-check.

Approximate Calculation

For the purposes of this calculation, we shall ignore gaps in the acceptance at sector boundaries. This would depend on the curvature (i.e. momentum) of the track and, being a higher order correction, would unnecessarily complicate the discussion. Thus acceptance at a given p_{T} is dependent only on the mean lifetime, the radii defining the fiducial volume and the magnetic field magnitude. In terms of particle yields, the acceptance correction is

$$\frac{1}{Acceptance} = \frac{\int_0^{\infty} \frac{d^2N}{dp_{\mathrm{T}}dr} dr}{\int_{r_{min}}^{r_{max}} \frac{d^2N}{dp_{\mathrm{T}}dr} dr} , \tag{4.3}$$

where r is the radius (in STAR coordinates) at which decay occurs, and $r_{max/min}$ reflect the fiducial volume 133 cm $< r <$ 179 cm. The lifetime distribution is well known ($\frac{dN}{dt} = \frac{1}{\tau} e^{-t/\tau}$, where $c\tau = 371.3$ cm is the charged Kaon mean lifetime). This motivates the recasting of the expression in terms of lifetime.

$$\frac{1}{Acceptance} = \frac{\frac{dN}{dp_{\mathrm{T}}} \int_0^{\infty} \frac{dN}{dt} dt}{\frac{dN}{dp_{\mathrm{T}}} \int_{t_{min}}^{t_{max}} \frac{dN}{dt} dt} = \frac{\int_0^{\infty} \frac{dN}{dt} dt}{\int_{t_{min}}^{t_{max}} \frac{dN}{dt} dt} \tag{4.4}$$

The numerator is readily integrated.

$$\int_0^\infty \frac{dN}{dt}dt = \int_0^\infty \frac{1}{\tau}e^{-t/\tau}dt = 1 \tag{4.5}$$

The integral in the denominator will not be analytic unless we make some approximations. We will show here that they are not unreasonable, and it will be demonstrated later that they yield a surprisingly good result. The first approximation is dr/dt. It is easy to show that $s = t\frac{p}{m}$, where s is the path length traversed by the Kaon before it decays. But $\frac{s_T}{s} = \cos(\lambda) = \frac{p_T}{p}$, where λ is the dip angle. This means that $s_T = t\frac{p_T}{m}$. One can see from Figure 4.2 that $r = 2R\sin(\frac{s_T}{2R})$, where $R = \frac{p_T}{qB}$ and the charge $q = .003\ \frac{\text{GeV/c}}{\text{T·cm}}$. In terms of lifetime and momenta,

$$r = 2\frac{p_T}{qB}\sin(t\frac{qB}{2m})\ . \tag{4.6}$$

The argument to the sine function for a mean lifetime Kaon in a 0.5 Tesla field is 0.56 . The sine of 0.56 is 0.53, so we see that by approximating $\sin x \simeq x$, we are only sacrificing about 5% accuracy for mean lifetime Kaons ($\langle p_T \rangle \simeq 600$ MeV). Recall that the outer radius of the kink fiducial volume is 179 cm, and the maximum extent in z from the origin is 210 cm. One can see, therefore, that the maximum pathlength for a charged Kaon originating from the origin is on the order of $\sqrt{(\frac{\pi}{2}179\text{ cm})^2 + (210\text{ cm})^2} = 351$ cm. This means that almost all Kaons that we detect have lifetime less than the mean, and our error at this step is considerably less than 5%.

In this approximation, $r \simeq 2R\frac{s_\perp}{2R} = s_\perp$, and so we have simply $r \simeq t\frac{p_T}{m}$. This enables us to do the integral in the denominator of the acceptance correction. The lifetime limits are $t_{max/min} \simeq r_{max/min}\frac{m}{p_T}$.

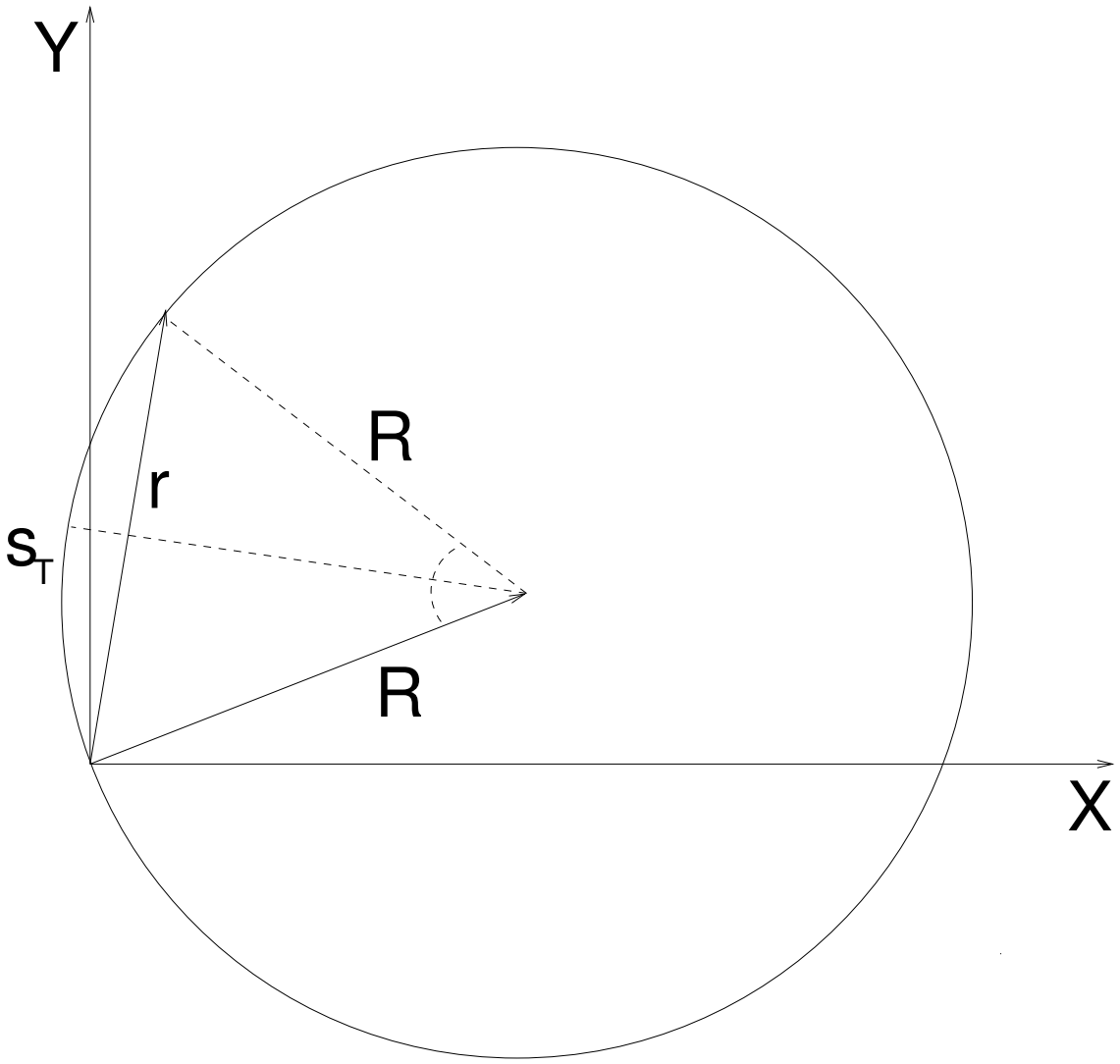

Figure 4.2: Path length in the transverse plane.

$$\int_{t_{min}}^{t_{max}} \frac{dN}{dt} dt \simeq \int_{r_{min}\frac{m}{p_T}}^{r_{max}\frac{m}{p_T}} \frac{1}{\tau} e^{-t/\tau} dt = e^{-r_{min}\frac{m}{p_T\tau}} - e^{-r_{max}\frac{m}{p_T\tau}} \tag{4.7}$$

At this point, another approximation is warranted. Here, the arguments to the exponential are large, and second order terms must be included in the approximation. It is useful to factor out these terms and define the alternate coordinates $x_{max/min} \equiv r_{max/min}\frac{m}{p_T\tau}$, $x \equiv 0.5(x_{max} + x_{min})$, and $\Delta \equiv 0.5(x_{max} - x_{min})$. For mean p_T charged Kaons, we have $x_{max} = 0.397$, $x_{min} = 0.295$, $x = 0.346$, and $\Delta = 0.051$. Thus expanding the exponentials to second order is good within 8%.

$$\begin{aligned} e^{-r_{min}\frac{m}{p_T\tau}} - e^{-r_{max}\frac{m}{p_T\tau}} &= e^{-x_{min}} - e^{-x_{max}} \simeq 2\Delta(1-x) \\ Acceptance\,\Big|_{\langle p_T \rangle} &= e^{-0.295} - e^{-0.397} = 0.0722 \\ &\simeq (0.397 - 0.295) + \frac{1}{2}(0.295^2 - 0.397^2) = 0.0667 \end{aligned} \tag{4.8}$$

With this somewhat crude approximation, we can now examine the functional form of the acceptance correction. We see that the expansion to second order is good to 4% for mean p_T.

$$\begin{aligned} \frac{1}{Acceptance} &= \frac{1}{2\Delta}\frac{1}{1-x} \\ \frac{1}{Acceptance}\,\Big|_{\langle p_T \rangle} &= 15.0 \\ &\simeq \frac{1}{2\Delta}(1 + x + x^2) = 14.4 \end{aligned} \tag{4.9}$$

Finally, we have a relatively simple approximation for the acceptance correction:

$$\begin{aligned} \frac{1}{Acceptance} &\simeq \frac{1}{2\Delta}(1 + x + x^2) \\ &= \frac{1}{r_{max} - r_{min}}\left(\frac{\tau}{m}p_T + \frac{1}{2}(r_{max} + r_{min}) + \frac{1}{4}\frac{m}{\tau}(r_{max} + r_{min})^2\frac{1}{p_T}\right) \\ &= 16.3 p_T + 3.39 + 0.704\frac{1}{p_T} \end{aligned} \tag{4.10}$$

With this estimate established, we will compare this simple result with the more comprehensive study from embedded Kaons.

Embedding Acceptance Correction

The more robust and accurate method is to use data with embedded MC Kaons. To simplify the discussion, we will introduce some terminology related to embedding in the particular context of kink analysis.

Embedded: Charged Kaons which are input to GEANT. They have not yet been propagated through STAR.

MC: Embedded Kaons which have been propagated through the STAR volume by GEANT and decaying in the kink fiducial volume.

Reco: A reconstructed kink; this is found using tracks which may contain hits from embedded or real tracks.

Reco Assoc: A Reco kink which is associated with a MC Kaon decaying in the fiducial volume.

This somewhat simplifies our definitions of efficiency and acceptance. Note that, in order to recover the original spectra, we need to multiply our raw spectra by the inverse of these factors. For example, the factors in a given transverse momentum bin would be

$$\begin{aligned} \frac{1}{Acceptance} &\equiv \frac{Embedded}{MC} \\ \frac{1}{Efficiency} &\equiv \frac{MC}{Reco\ Assoc} \\ Correction &\equiv \frac{Embedded}{Reco\ Assoc} = \frac{1}{Acceptance \cdot Efficiency} . \end{aligned} \tag{4.11}$$

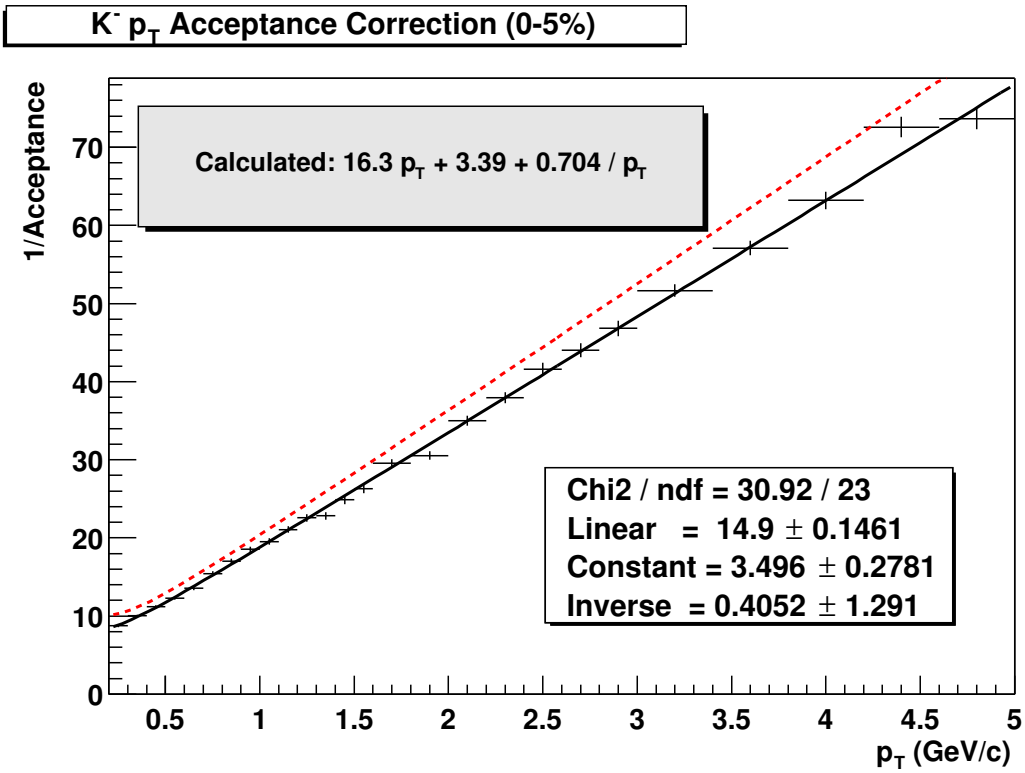

Figure 4.3: Calculated acceptance correction (dashed) and the actual correction from embedded Kaons (solid).

A representative example of the acceptance correction factor is shown in Figure 4.3. This shows the almost linear form of the acceptance in the region $0.2 < p_{\mathrm{T}} < 5$ GeV/c. It also shows the result of fitting this to an expression with the form found above. The function fits well, and the curve differs by less than 10% from the rough estimate made above.

For the simple acceptance factor we calculated, there should be no dependence on centrality. The only factors are the lifetime of the particle, its transverse momentum, and the boundaries of the fiducial volume. In the inter-sector gaps, one expects to lose more high p_{T} particles because they have straighter tracks and can miss the active pad volume entirely. Since this is a higher order effect, though, we expect our

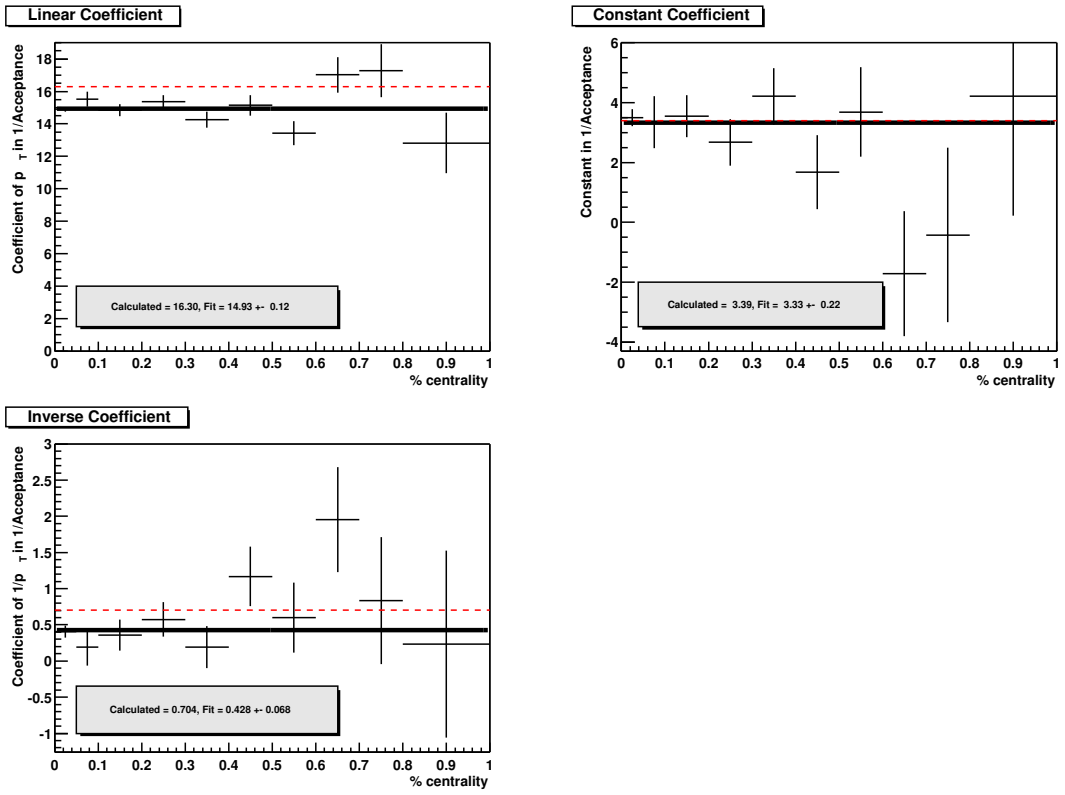

Figure 4.4: The three parameters of the acceptance correction fit vs. centrality. The dashed line is the calculated value, and the solid line is the fit (mean) over all centrality.

acceptance correction to be fairly uniform across centrality. Figure 4.4 shows the parameters found when fitting the acceptance correction in each of the ten centrality bins. One sees that the linear term is fairly uniform across centrality, where the smaller contributions are somewhat less well determined. In all cases, though, the mean across centrality of the fit parameter is close to the estimated value. These mean fit parameters are shown below:

$$\frac{1}{Acceptance} = 14.9 p_{\mathrm{T}} + 3.33 + .428 \frac{1}{p_{\mathrm{T}}} \tag{4.12}$$

4.2.2 Efficiency

Efficiency (or lack thereof) may be a result of the detector hardware, cluster finding, hit finding, track finding, secondary vertex (kink) finding, and analysis cuts. These varied sources are beyond estimation with simple models, so we continue with the embedded Kaons. We calculate the correction factor in Equation 4.11 as a function of p_{T} or m_{T}. As is the case with Acceptance, calculating the correction histograms for each spectrum independently is much more accurate than calculating the p_{T} factor from the m_{T} correction or the reverse.

The p_{T} efficiency correction for the most central bin is shown in Figure 4.5. One sees that the maximum efficiency is about 12%, going below 3% for higher momenta. This unfortunate effect is due to the fact that the individual parent and daughter tracks for the kink are not well resolved for decay angles below 6 degrees. In fact, the majority of such kinks are never reconstructed because the short daughter track is merged with the parent during track-finding. Because of the Lorentz boost from the parent, the mean decay angle becomes smaller for higher momentum kaons. At momenta above 3 GeV, most kaons have decay angles below 6 degrees. Work is under way to address this issue, as it seriously impacts the ability of STAR to measure high momentum charged kaons from their decay topology. The efficiency also dips at lower p_{T}; this decrease in the kink-finding efficiency reflects the drop in single track reconstruction efficiency at lower momenta.

4.2.3 Background Correction

The efficiency and acceptance corrections compensate for real Kaons that we miss in reconstruction. Now we move on to the study of background, i.e. reconstructed

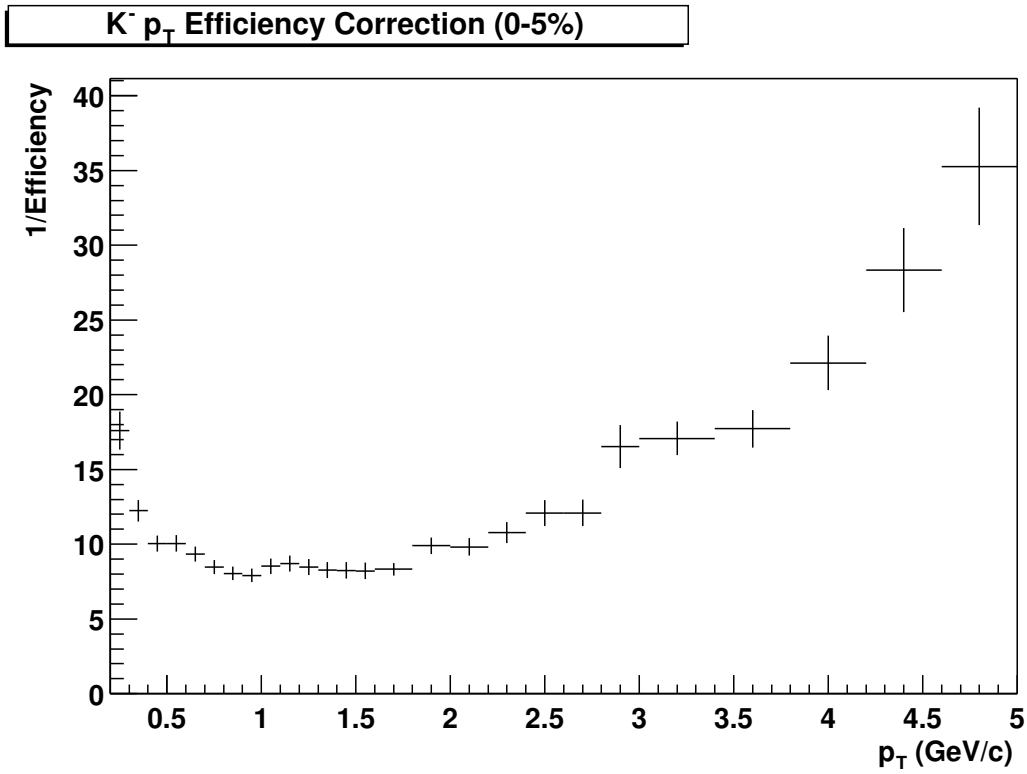

Figure 4.5: Kink-finding efficiency versus transverse momentum, calculated using embedded Kaons.

kinks that are not really Kaons. Again, simulation is the most powerful tool we have for understanding background, because it is the only one which allows us to know what was really a Kaon in the first place. In order to get the necessary statistics, one normally examines pure HIJING events instead of embedded data.

Association plays a key role once more when examining the background. Kinks which are associated with MC Kaon decays are signal. Those which are associated with some other MC process are correlated background. Finally, those not associated with any MC vertex are pure combinatorial background. Once the magnitude of the background in HIJING is known, we are faced with two questions: 1) What method should be used to subtract the estimated background from the data? 2) How reliable is the background correction obtained from HIJING?

Comparison of HIJING with data

We shall address the latter question first. The best way to evaluate the accuracy of HIJING in this respect is to compare it to the results from data. The kink decay angle is one good probe, because its theoretical distribution is easily calculated from first principles. This allows us to compare both data and HIJING to the theoretical result. The result of this comparison is shown in Figure 4.6. The details of the charged Kaon decay kinematics are covered in Appendix B. Knowing the distribution of decay angles in the lab frame from Equation B.2, we can easily throw random decay angles in the CM frame. These values can then be boosted into the lab frame using Equation B.3. In order to transform them into the lab frame, however, we must use a realistic momentum distribution. The best way to do this is to generate a theoretical decay for each reconstructed Kaon in the data. One can then use this momentum to boost the CM decay angle into the lab. Now the procedure to calculate

the theoretical decay angle distribution is clear:

1. Generate a lab decay angle θ in [0, π] and a probability ρ_θ in [0, 1].

2. If $\rho_\theta \leq \frac{\sin\theta}{2}$, proceed to step (3). Otherwise, repeat step (1). This selects the area under the curve $p(\theta)$, reproducing the correct probability distribution for θ.

3. Take the magnitude of the momentum from a kink candidate in data. Use this momentum to boost the CM decay angle into the lab frame using Equation B.3.

Figure 4.6 shows the decay angle distributions in the mean p_{T} bin ($.55 < p_{\mathrm{T}} < .65$ GeV/c). They are normalized to have the same integral. One notes the longer tail of the calculated distribution. This can be attributed to lower kink reconstruction efficiency at higher decay angle. The data and HIJING curves agree fairly well, with their centers being offset by approximately 5 degrees. The high angle tails are in very good agreement.

One sees even better agreement between MC and data in the parent-daughter DCA distribution shown in Figure 4.8. HIJING is slightly shallower, differing by about 5% at the peak and 50% in the tail.

Another kinematic variable to examine is the invariant mass obtained if one assumes the Muon ($K^+ \to \mu^+\nu_\mu$) decay channel. One uses 3-momentum conservation in the lab to determine the momentum of the missing daughter and solves for the parent mass:

$$\begin{aligned} \overrightarrow{p_\nu} &= \overrightarrow{p_K} - \overrightarrow{p_\mu} \\ \text{Invariant Mass} &= \sqrt{m_\mu^2 + p_\mu^2 + p_\nu^2 - p_K^2} \end{aligned} \tag{4.13}$$

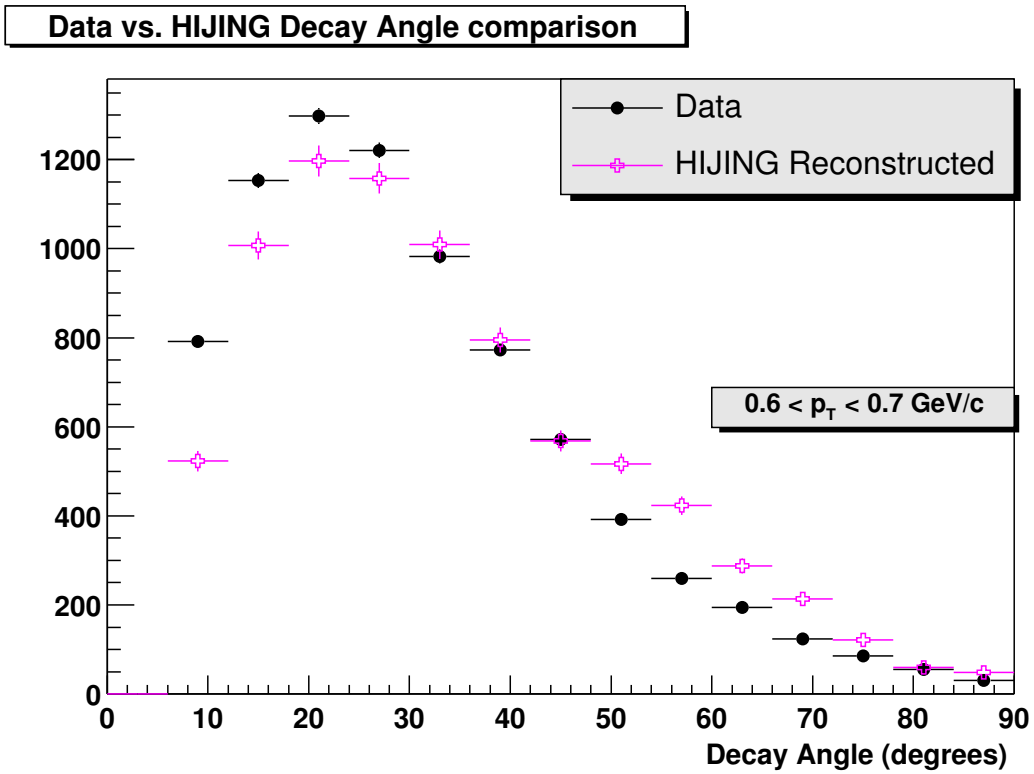

Figure 4.6: Comparison of decay angle from HIJING and data.

This distribution should be peaked at the charged Kaon mass. This is seen in the HIJING spectra shown in Figure 4.7. Note that the other decay modes are visible. The 2 Pion channel ($K^+ \to \pi^+\pi^0$) is peaked slightly below the Muon channel, and the 3 Pion channels ($K^+ \to \pi^+\pi^+\pi^-$ and $K^+ \to \pi^+\pi^0\pi^0$) are peaked at a much lower invariant mass. Looking at the invariant mass from data, we see a very similar shape, with an obvious pion contribution to the low invariant mass peak.

Background Subtraction

Since we have convinced ourselves that HIJING can reproduce with reasonable accuracy the distributions found in real data, we now focus on a method of applying the background estimate from HIJING to the data. Figure 4.8 shows the parent-daughter DCA distributions for data and reconstructed HIJING kinks after all other analysis cuts (integrated over p_{T}). It also shows the combinatorial and correlated background from HIJING. We see that we are dominated by combinatorial background in all regions; the total background is less than 10% of the reconstructed kinks.

The correlated background peaks at low DCA, as would be expected for a real physical process, and the combinatorial background is mostly flat with a small rise at lower DCA. Even in the tail, the Kaon signal dominates out to 5 mm. We desire a method which will allow us to estimate the background in the low DCA region, where the Kaon signal is strongest. Since the background is more dominant at high DCA, it is natural to use the reconstructed yield in this region as an estimate of the background. For the best estimation possible, we seek a DCA_{cut} such that the integral of all reconstructed tracks from DCA_{cut} to 0.5 cm closely approximates the integral of the background in the region from 0 cm to DCA_{cut}.

The method of background subtraction for each bin in p_{T} is as follows:

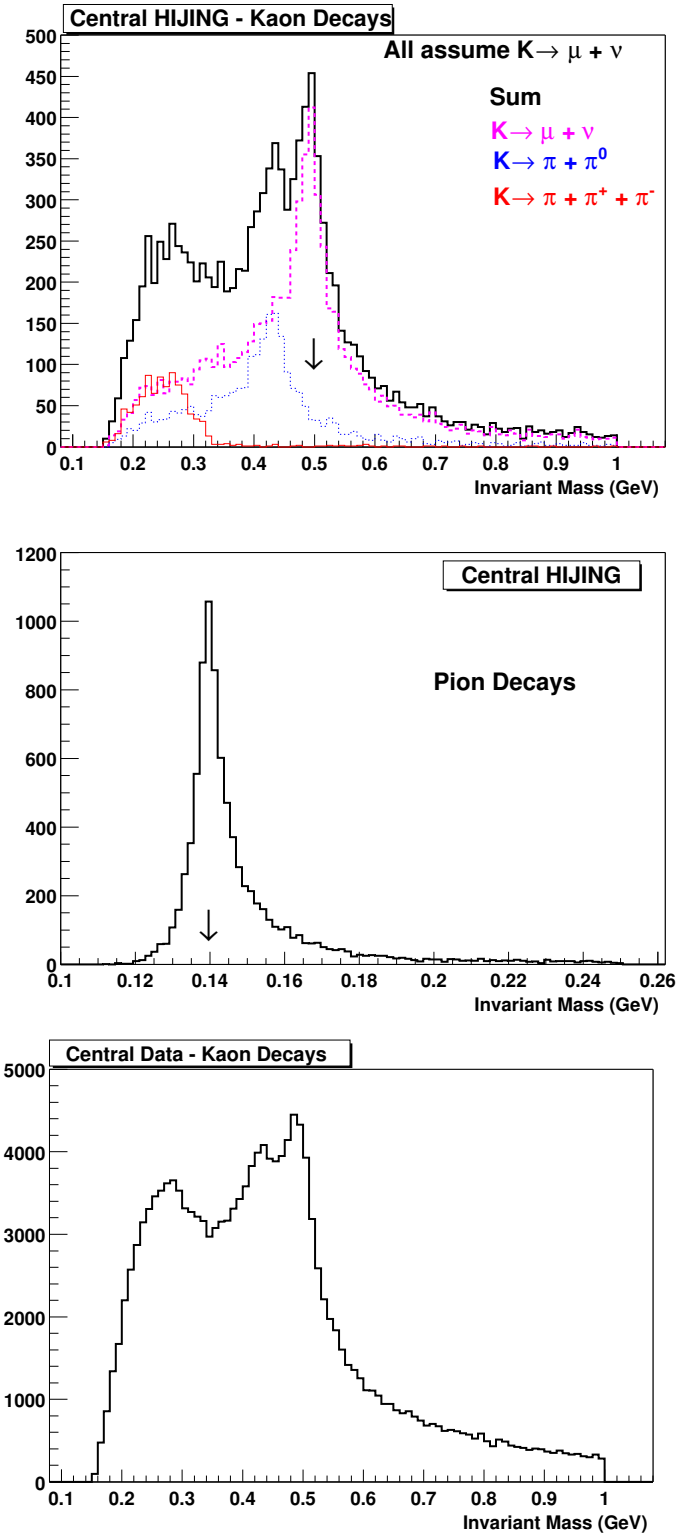

Figure 4.7: Invariant mass distributions from data and HIJING.

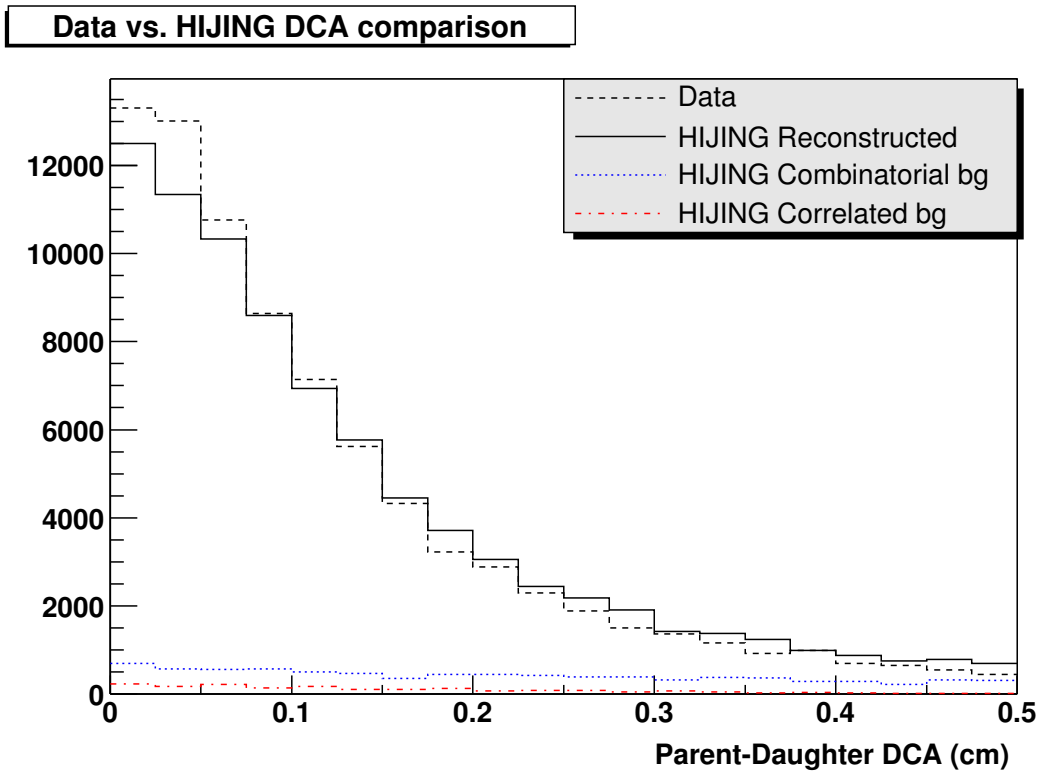

Figure 4.8: Comparison of parent-daughter DCA from HIJING and data.

1. Make the $dN_{reco}/d(\mathrm{DCA})$ and $dN_{background}/d(\mathrm{DCA})$ histograms.

2. Search for DCA_{cut} such that

$$\int_{\mathrm{DCA}_{cut}}^{0.5\ \mathrm{cm}} \frac{dN_{reco}}{d(\mathrm{DCA})} d(\mathrm{DCA}) = \int_{0\ \mathrm{cm}}^{\mathrm{DCA}_{cut}} \frac{dN_{background}}{d(\mathrm{DCA})} d(\mathrm{DCA}) \tag{4.14}$$

3. Fit the resulting DCA_{cut} to a smooth function of p_{T}.

4. For data, kinks with DCA $\leq \mathrm{DCA}_{cut}$ are labeled as signal. Those with DCA $> \mathrm{DCA}_{cut}$ are labeled as background. The "background" spectra is then subtracted from the "signal" spectra to form corrected m_{T} or p_{T} spectra. (This step is done before efficiency and acceptance corrections, of course.)

The cut DCA varies considerably with p_{T}, as one might expect. The higher the p_{T}, the straighter is the track, and the more compressed is the DCA distribution of Kaon signal. The cut DCA can be seen in Figure 4.9. One sees that it ranges from 0.45 cm for the lowest p_{T} to about 0.25 cm for the higher p_{T}. The cut DCAs for the individual p_{T} bins are fit to an empirical functional form. It has no physical motivation, but serves to smooth the curve at higher p_{T}, where low statistics from HIJING cause uncertainty in the cut DCA. This curve fits very well the low p_{T} region and is effectively flat above 2 GeV/c. This is quite reasonable, as tracks above 2 GeV/c are for all intents and purposes straight lines. One important point is that the DCA cut does not vary significantly over centrality. Comparison of DCA distributions for central and peripheral data show no substantial difference. So the DCA cut function may be used without regard for centrality. Its functional form is $\mathrm{DCA}_{cut}(p_{\mathrm{T}}) = 0.160\ \mathrm{cm} + (0.0949\ \mathrm{cm})/p_{\mathrm{T}}^{0.701}$. The errors from the fit are propagated to the final background-subtracted spectra.

It should be noted that the background is slightly different for K^+ and K^-. The combinatorial background is the same for both, but the correlated background differs due to the different physical processes and the abundances of the particles contributing to the background. The combinatorial background makes up about 8% of the data for each charge sign, and the average of the correlated background is about 2%. The K^+ correlated background is 20% higher than that for K^-, which propagates to less than a 0.5% effect on the corrected spectra. That being the case, we estimate the background by summing both charges to increase statistics and improve the precision of the DCA cut.

4.3 Analysis Cuts

Background subtraction is a useful tool, but it is only an estimate and is only as good as the simulation software one uses. In the analysis, it is important to reduce the background as much as possible while preserving Kaon signal. One only uses the background subtraction to compensate for background which cannot be eliminated by a suitable analysis cut. What follows are the set of offline analysis cuts we use to reduce the background from over 90% to 10% while preserving most of the signal.

For each cut, we show HIJING kinks after all other cuts have been made. This gives a good idea of the net effect of each cut. The first plot shows actual Kaon decays from HIJING (signal). The other two show the correlated and combinatorial background from HIJING. All of the analysis cuts are summarized in Table 4.1.

4.3.1 DCA Cut

As mentioned above, Figure 4.9 shows the parent-daughter DCA cut along with the HIJING signal and background. One can see that the DCA distribution narrows

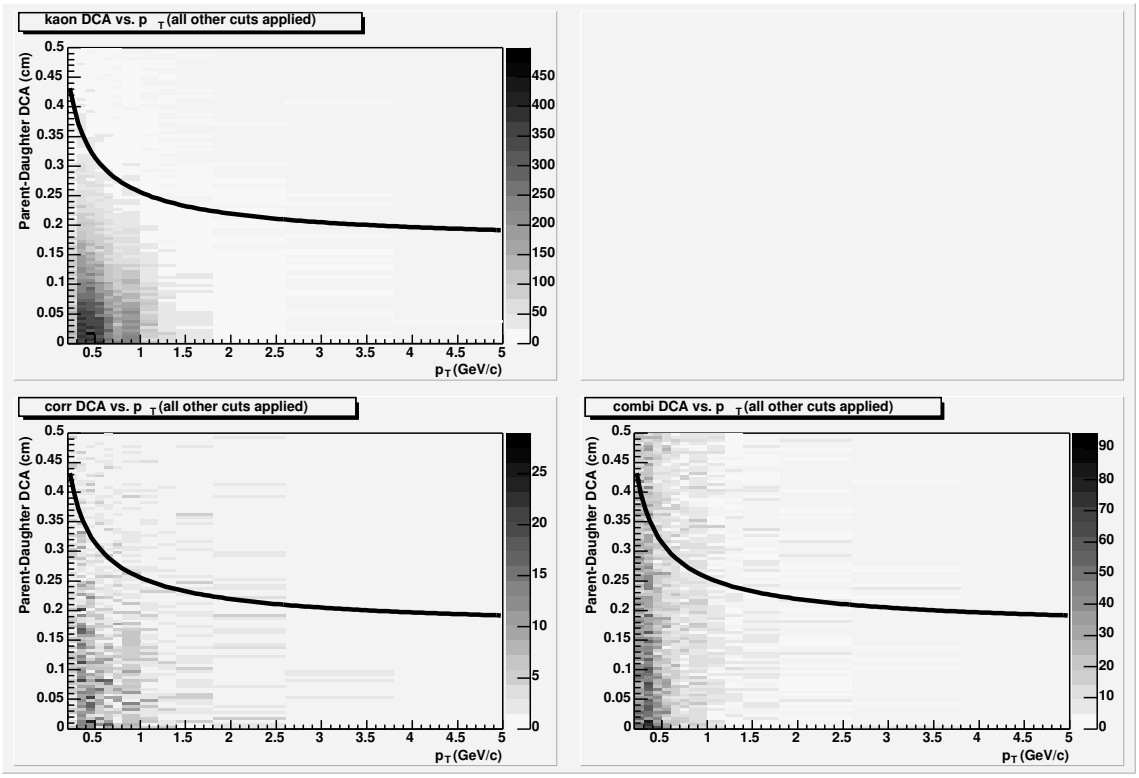

Figure 4.9: HIJING Parent-daughter DCA vs. p_{T} for signal, correlated background, and combinatorial background.

with increasing p_{T}. The relatively flat distribution of the combinatorial background is also seen. This cut does not significantly reduce background; we use it principally to estimate the background in the low DCA region.

4.3.2 Local ϕ Cut

The boundaries between sectors cause considerable problems with track reconstruction. Tracks are often split, creating one track in each sector. These track pairs are easily reconstructed as kinks with low decay angle. The majority of these split tracks may be eliminated from our analysis by cutting on the local azimuthal angle relative to the center line of the TPC sector in which the decay occurred. One sees that the majority of the combinatorial background is outside this cut. The cut, shown

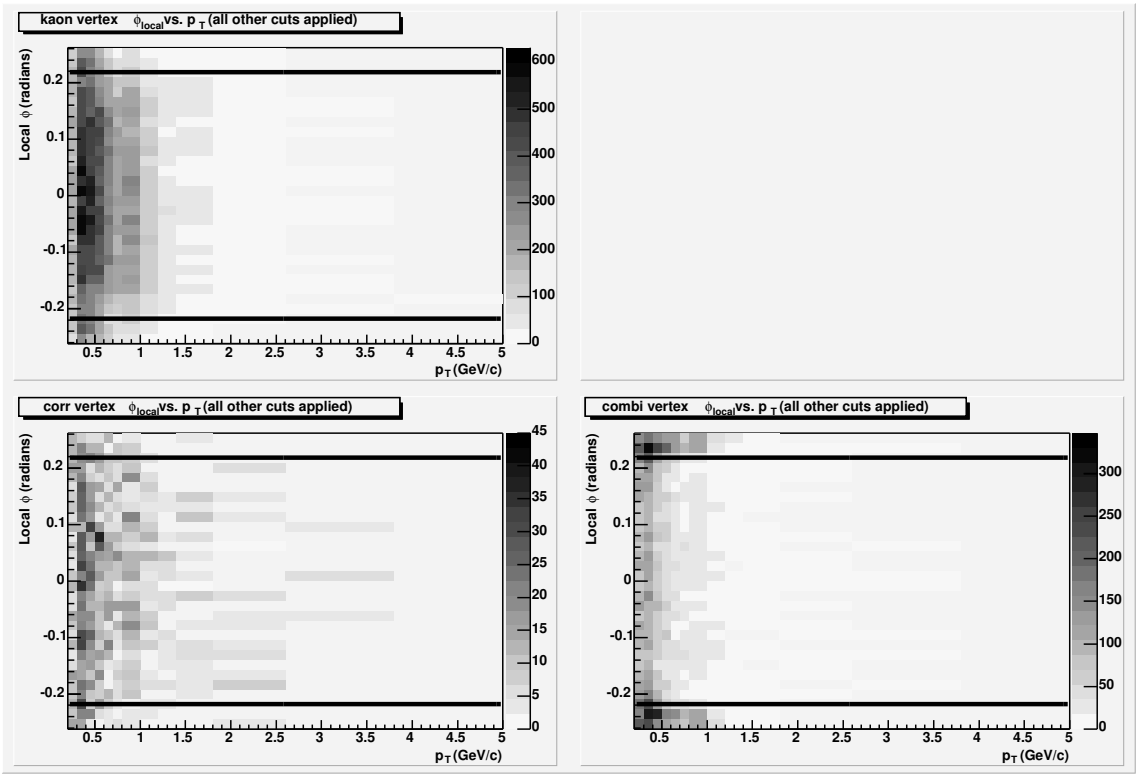

Figure 4.10: HIJING sector-local ϕ vs. p_{T} for signal, correlated background, and combinatorial background.

in Figure 4.10, preserves the inner 25 degrees (out of 30) in each sector and removes kinks within 2.5 degrees of the sector boundary. It is not momentum-dependent.

4.3.3 Daughter Momentum

One quality cut is on the momentum of the daughter particle. We cut at 100 MeV/c, which removes a great deal of combinatorial background. One source of this background is the random intersection of a primary track with a low momentum spiral. Another is intersection with a low momentum artificially reconstructed "ghost" track.

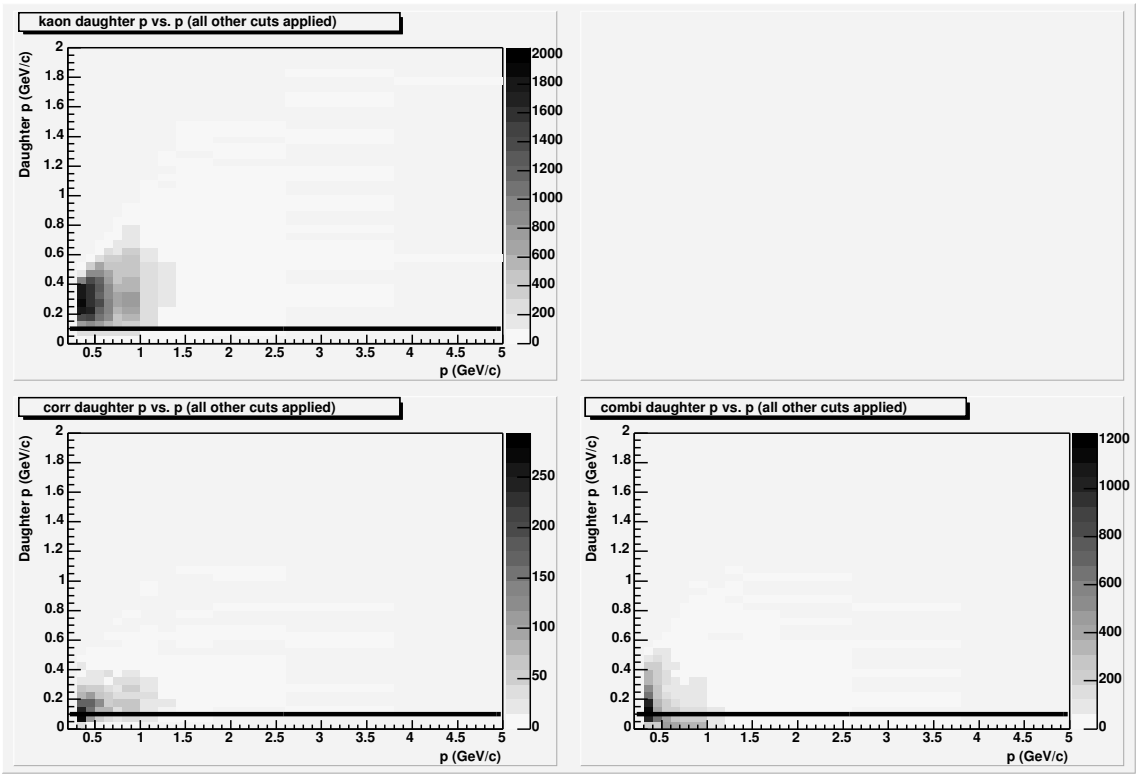

Figure 4.11: HIJING daughter momentum vs. parent momentum for signal, correlated background, and combinatorial background.

4.3.4 Decay Angle

This is one of our most powerful tools for reducing Pion contamination. A decaying particle provides a Lorentz boost to its daughters. In the CM frame, the magnitude of the daughter momentum has a single, unique value. If the momentum of the parent is high enough, then the Lorentz boost is so strong as to limit the possible decay angle in the lab frame. It is boosted so far forward that it cannot decay at larger angles. This is easily quantified for the $\pi^+ \to \mu^+\nu_\mu$ and $K^+ \to \mu^+\nu_\mu$ decays, where the neutral daughter is massless. Following the method in Appendix B, we calculate the maximum decay angle as a function of parent momentum for both the pion and Kaon decays. The former we use as a lower cut, and the latter an upper. One can see that the lower cut eliminates almost all Pions (correlated background) remaining in our sample. The upper cut does little. Our actual lower cut is about 4 degrees above the theoretical maximum for Pion decays to compensate for momentum resolution and other effects. One sees that this reduces a great deal of combinatorial background at higher momentum while having little impact on the signal.

4.3.5 dE/dx cut

Energy loss is another way of removing Pions from our sample. We cut around the Bethe-Bloch curve for charge Kaons, removing very little signal but eliminating much of the correlated (mostly Pion) background. Interestingly, this cut also removes a great deal of combinatorial background. This is due to the fact that the majority of combinatorial background at low momentum still has a pion as the kink parent. (This is just statistical; Pions make up the majority of low momentum particles.) See Figure 4.13.

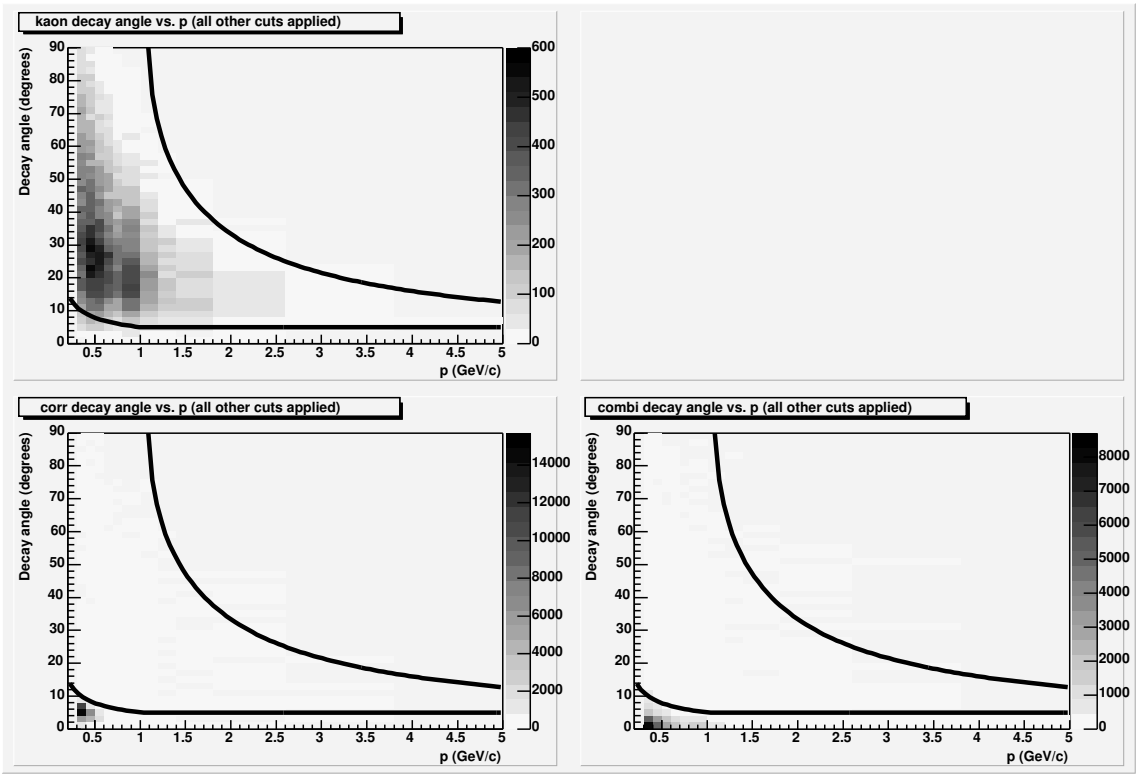

Figure 4.12: HIJING decay angle vs. momentum for signal, correlated background, and combinatorial background.

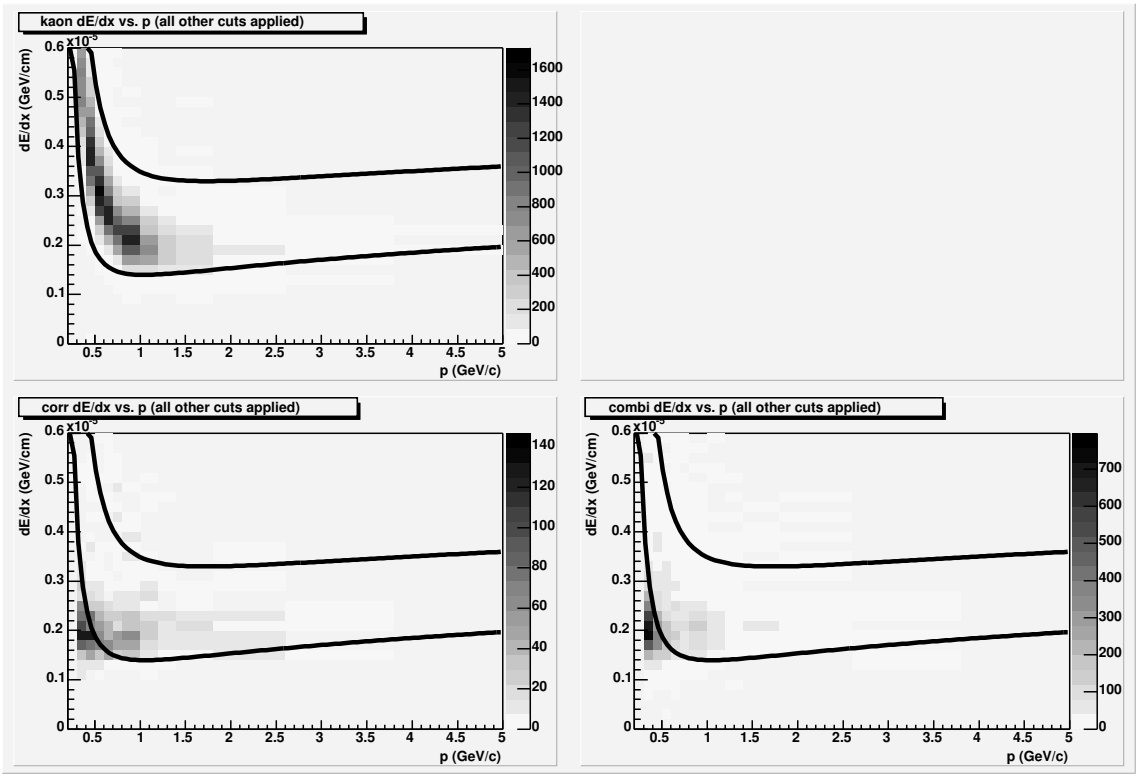

Figure 4.13: HIJING $\frac{dE}{dx}$ vs. momentum for signal, correlated background, and combinatorial background.

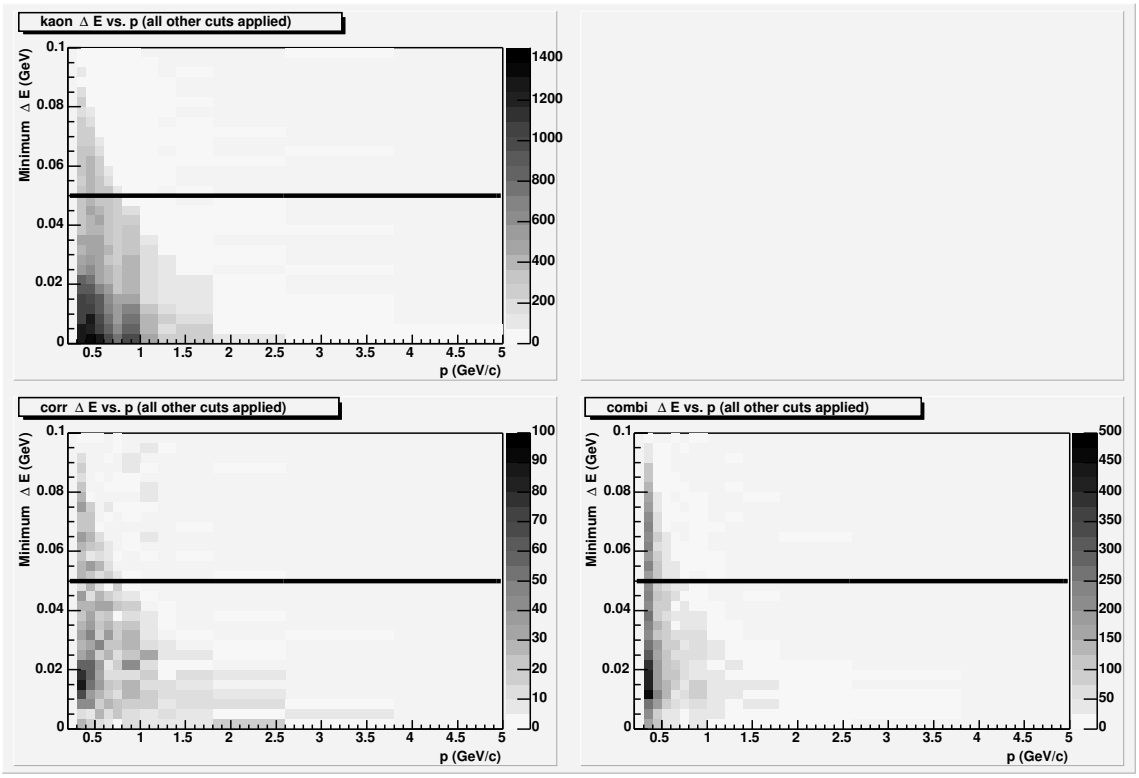

Figure 4.14: HIJING minimum ΔE vs. momentum for signal, correlated background, and combinatorial background.

4.3.6 Minimum ΔE

In the analysis of the $\sqrt{s_{NN}}$=130 GeV data, the kinematic cut used was the "minimum ΔE", a quantity formed by finding the minimum degree of energy non-conservation among various decay hypotheses. For each kink, energy and momentum are conserved based on several Kaon and Pion decay hypotheses. The hypothesis which results in the best degree of energy conservation is chosen, and the amount by which it differs from zero is its Minimum ΔE. One can see on Figure 4.14 that the cut does little to reduce background. Both signal and Background are concentrated at low ΔE.

Rapidity, y	$\|y\| < 0.5$ for p_{T}, m_{T} spectra
Parent-daughter DCA	Upper limit used to estimate background
Local ϕ	Avoid 5° region around sector boundaries
Daughter momentum	> 100 MeV/c
Decay Angle, θ	θ_{max} for $\pi \rightarrow \mu\nu < \theta < \theta_{max}$ for $K \rightarrow \mu\nu$
dE/dx	Within Kaon band
Minimum ΔE	Used in 130 GeV Au-Au
Invariant mass	Used in 200 GeV Au-Au, improved background reduction

Table 4.1: Online reconstruction cuts for kink decays.

4.3.7 Rapidity

We choose the region of mid-unit-rapidity ($|y| < 0.5$) to conduct our analysis because that covers most of the TPC fiducial volume while avoiding the higher rapidity region where the acceptance is smaller (and the correction is larger and more difficult to estimate accurately). We shall see that the charged Kaon distribution in this region is flat as a function of rapidity (i.e., boost invariant).

4.3.8 Invariant Mass

The search for a better kinematic cut resulted in choosing invariant mass. This is calculated by assuming the $K^+ \rightarrow \mu^+\nu_\mu$ decay channel for a kink, as shown in Equation 4.13. The distribution of this value is shown in Figure 4.15. For the Kaon signal, one sees clearly the two peaks for the three dominant decay modes. The Muon channel is centered at the Kaon mass. The two Pion channel is peaked only slightly below this and appears as part of the same peak. The lower peak is due to the three Pion channels. One sees that most of the combinatorial and correlated background is below 0.3 GeV/c^2, so we sacrifice the least significant Kaon decay mode in the signal and drastically improve our signal to noise ratio. There is also a loose upper cut at 1 GeV/c^2.

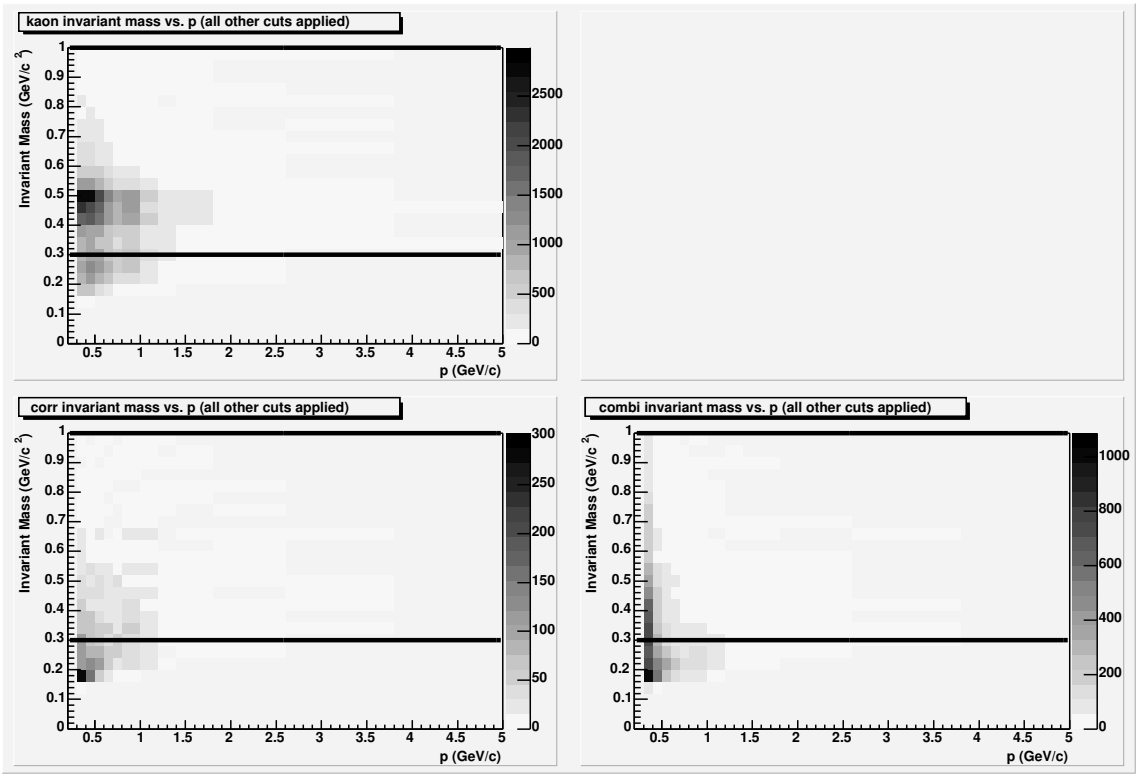

Figure 4.15: HIJING invariant mass vs. momentum for signal, correlated background, and combinatorial background.

4.4 Systematic Error

Systematic error is determined using several methods. First, differences in corrected spectra as a function of detector geometry (azimuth or reflection in z) indicate a systematic uncertainty. Secondly, variation of the analysis cuts should not affect the corrected spectra; any effect reflects a systematic uncertainty. Thirdly, a systematic error for the background estimation technique may be inferred from the difference between the signal to background ratio in data vs. that in HIJING simulation. A fourth source of systematic uncertainty is momentum resolution. Finite resolution will cause momentum spectra to "bleed" to higher momenta, assuming that resolution is roughly symmetric. See Figure 4.16 for the momentum resolution, which is defined as the difference between the reconstructed and input momenta divided by the input momentum. The net effect of these systematic uncertainties is 7% at $p_{\mathrm{T}} =$ 1 GeV/c and 15% at $p_{\mathrm{T}} = 2.5$ GeV/c.

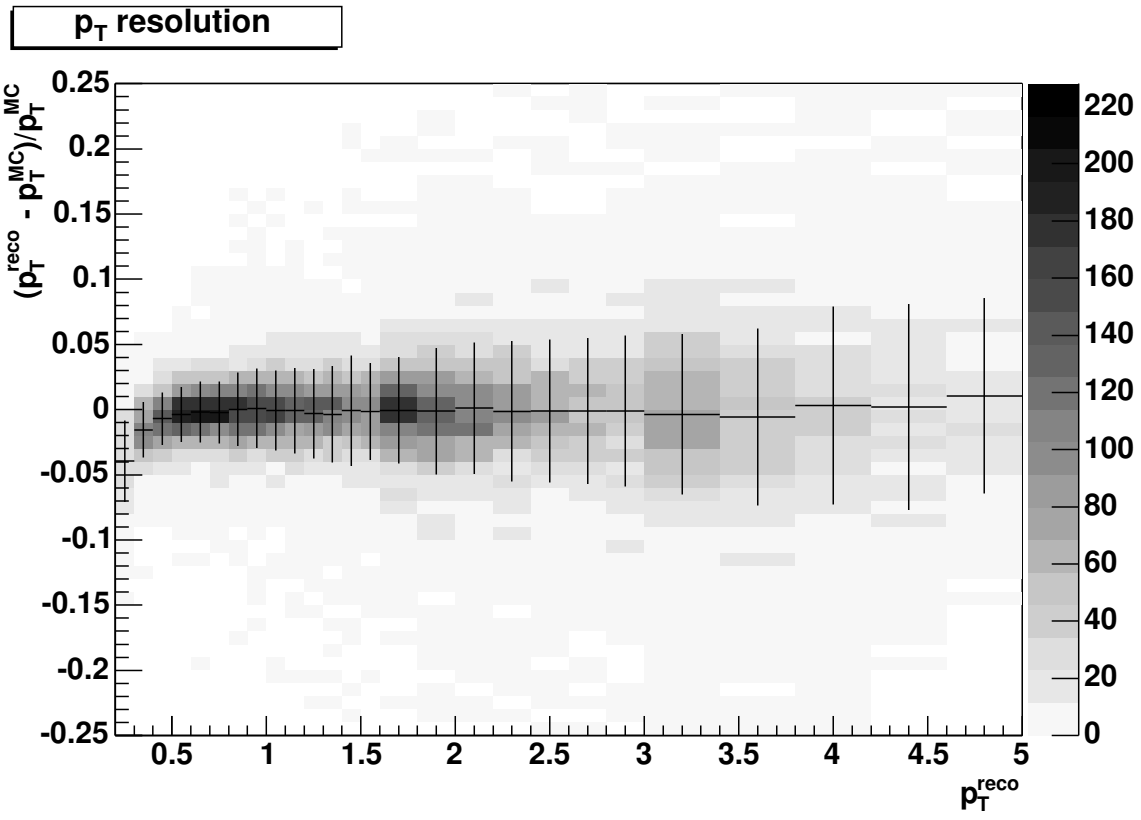

Figure 4.16: p_{T} resolution calculated from embedded data.

Chapter 5

Results and Discussion

5.1 Event Selection

The events analyzed were selected based on collision centrality and factors related to data quality. For example, a small percentage of events were eliminated from the analysis due to transient detector problems discovered during STAR's comprehensive quality assurance procedures. The data in these events could not be reliably analyzed. Similarly, events which had an interaction point outside the center 50 cm of the TPC were not analyzed because of biases introduced in centrality determination. Results are presented in terms of collision centrality, which is determined from analysis of the minimum bias triggered data. The standard in STAR is to base collision centrality on the number of primary tracks in mid unit pseudorapidity ($|\eta| < 0.5$); this is commonly called nCharge. The values of nCharge used for centrality bins and the corresponding fraction of the total Au-Au cross section of 7.2 barn are shown in Table 5.1. A Glauber model can be used to relate nCharge to the impact parameter, the number of participating nucleons, and the number of binary collisions. [17]

Unless otherwise indicated, the data shown for the 5% most central bin is from events with the ZDC central trigger. These ZDC triggered events are the 10% most central according to ZDC measurements. Refer to Figure 2.5 for details of this cut.

The other centrality bins are taken from the minimum bias triggered data. One final event cut is required to ensure a minimum of centrality bias. The ZDCs are used for a rough determination of the collision vertex by comparing the times at which

Fraction of total cross section (7.2 b)	nCharge $\geq$
0.8	14
0.6	56
0.4	146
0.3	217
0.2	312
0.1	431
0.05	510

Table 5.1: Fraction of total Au-Au cross section (from a Glauber model calculation) as a function of nCharge (the number of primary tracks with $|\eta| < 0.5$).

neutrons are detected on each end of the experimental hall. This ZDC coincidence measurement has some dependence on centrality for large vertex z positions. As a result, we are required to limit the vertex z position to ± 25 cm for all events.

5.2 K-/K+ ratio

Particle ratios provide useful probes of the chemical composition of the collision fireball at different stages. [1] Anti-particle to particle ratios are of particular experimental interest because many of the measurement uncertainties are divided out. For example, the acceptance for K^+ and K^- are functions only of the detector geometry and the particle lifetime; thus this factor is the same for both species in the STAR TPC. Regarding background, it has been discussed that the difference between the correlated background in K^+ and K^- results in less than a 0.5% effect in the ratio. Therefore all correction factors are effectively cancelled out of the ratio except for efficiency. That is because K^- ($\bar{u}s$) has a higher inelastic cross section for interaction with nucleons than K^+ ($u\bar{s}$) [26]; it is more prone to absorption in the detector before it can be reconstructed. All the ratios we present here are absorption-corrected, meaning that the projected difference in the ratio due to absorption is accounted for. The acceptance correction and the non-absorption part of the efficiency correction

are not applied, as these are the same for both signs.

The anti-meson/meson ratio is of particular interest for charged Kaons. Charged Kaons are produced by two means. First, the strange and anti-strange quarks may be pair-produced in the initial stage of the collision. If this were the only source, and the $s/\bar{s}$ quark ratio completely determined K^-/K^+, we would expect a ratio of exactly 1.0 . Since the K^+ also carries the valence up quark, however, it can also be made in "associated production" along with a strange baryon (hyperon) such as $\pi^+ n \rightarrow K^+\Lambda$. Thus the net baryon density (baryons - anti-baryons) is also important because that determines the relative abundance of the (anti-)up quarks. If the net baryon density is greater than zero, K^+ is more likely to be produced because it contains the more common up quark. Therefore in environments with high baryon density the K^-/K^+ ratio is expected to be very low. The net proton yield (protons - antiprotons) as a function of $\sqrt{s_{NN}}$ is shown in Figure 5.1. [27] One can see the clear decrease in the net baryons, while particle production is strongly increasing.

A simple model which provides insight into the charged Kaon ratio is the "constituent quark" or "quark coalescence" model [28], in which the relative abundances of final state hadrons are related to the abundances of their valence quarks. Using simple quark counting, for example, we can predict the K^-/K^+ ratio:

$$\frac{K^-}{K^+} = \frac{(s\bar{u})}{(u\bar{s})} = \frac{(\bar{u}\bar{u}\bar{d})}{(uud)} \cdot \frac{(uds)}{(\bar{u}\bar{d}\bar{s})} = \frac{\bar{p}}{p} \cdot \frac{\Lambda}{\bar{\Lambda}} \tag{5.1}$$

The ratio we measure for the 5% most central data is $K^-/K^+ = 0.90 \pm 0.002(\text{stat.}) \pm 0.05(\text{syst.})$. (See Figure 5.4.) The $\bar{p}/p$ and $\bar{\Lambda}/\Lambda$ ratios are also measured in STAR; they are 0.75 ± 0.05 and 0.82 ± 0.06, respectively.[29] That predicts a charged Kaon ratio of 0.91 ± 0.13, in very good agreement with the measured value. The value measured for $\sqrt{s_{NN}} = 130$ GeV Au-Au collisions at RHIC in STAR was $0.88 \pm 0.01(\text{stat.}) \pm 0.05(\text{syst.})$.

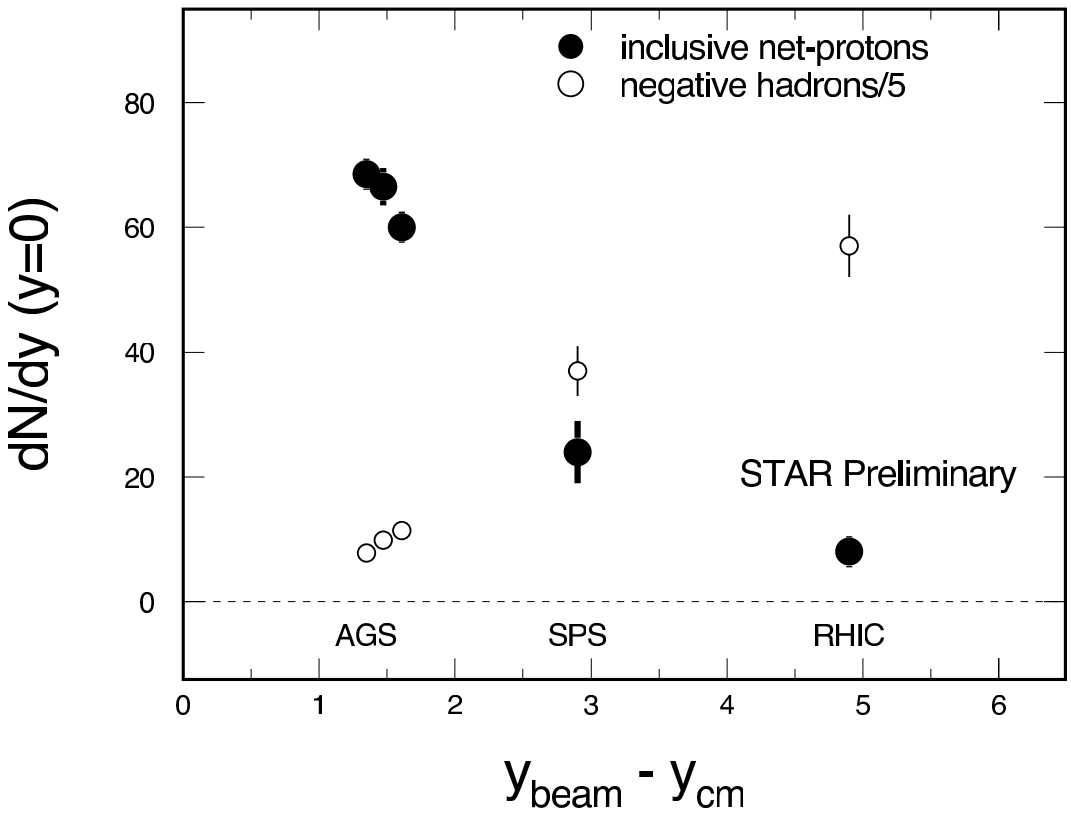

Figure 5.1: Net protons as a function of $\sqrt{s_{NN}}$. The strong decrease of net baryon density is readily apparent.

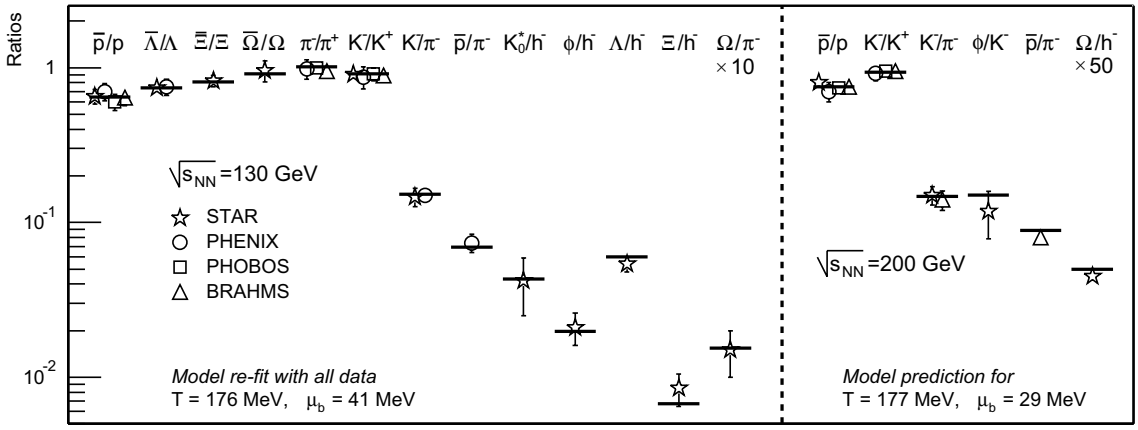

Figure 5.2: Left panel: comparison between RHIC experimental particle ratios for $\sqrt{s_{NN}} = 130$ GeV and statistical model calculations with $T_{\rm ch} = 176$ MeV and $\mu_{\rm B} = 41$ MeV (from [1, 2]). Right panel: comparison between RHIC ratios at $\sqrt{s_{NN}} = 200$ GeV and prediction discussed in the text (also [1, 2]).

We see a slight increase in the ratio, suggesting some decrease in the net baryon density for $\sqrt{s_{NN}} = 200$ GeV. Since the measured value is approximately 1, we conclude that the mid-rapidity RHIC environment is almost, but not totally, baryon free. This is expected since, at these energies, it is quite difficult to transport baryon number 5 units of rapidity from the incident beam. It is interesting, though, to see that the baryon transport over this large range of rapidity is still finite at RHIC energies; this warrants further study.

Another model which does very well at describing particle ratios at RHIC is a statistical thermal model. [1] A wide variety of particles are well matched, as shown in Figure 5.2. We see that the chemical freezeout temperature ($T_{\rm ch}$) is virtually unchanged between 130 GeV and 200 GeV Au-Au collisions (176 MeV $\rightarrow$ 177 MeV), but the baryon chemical potential ($\mu_{\rm B}$) drops considerably (41 MeV $\rightarrow$ 29 MeV).

5.2.1 K^-/K^+ vs. rapidity

It is important to remember that the results presented here are only at mid unit rapidity. The simple quark counting model above is only valid for integrated 4π yields. This is because the conservation of quantum numbers is only necessary when considering all particles produced in an interaction. The fact that we observe excellent agreement with the model is due in no small part to the fact that the charged Kaon yields (and ratios) are very close to being independent of rapidity. The ratio as a function of rapidity is shown in Figure 5.3. This flatness also indicates that the assumption of local quantum number conservation can be applied around mid-rapidity. At higher rapidities this ratio should decrease due to higher baryon density; the closer one is to beam rapidity, the stronger will be the effect of participant nucleons on the baryon density.

In the symmetric environment of STAR, we expect symmetry across y=0. Any variance between corresponding bins in positive and negative rapidity is due to systematic errors and can be used as a tool in estimating them.

5.2.2 K^-/K^+ vs. p_{T}

At higher p_{T}, where pQCD sets in, we expect to see this ratio decrease due to valence quark fragmentation. [30] Figure 5.4 shows the K^-/K^+ ratio as a function of p_{T} for the 5% most central collisions. The K^-/K^+ ratio as a function of transverse momentum is flat within statistical error out to 4.2 GeV/c. The lack of dependence of the ratio on p_{T} may indicate a complex interplay among different factors affecting the shape of the individual momentum spectra such as radial flow and valence quark fragmentation.

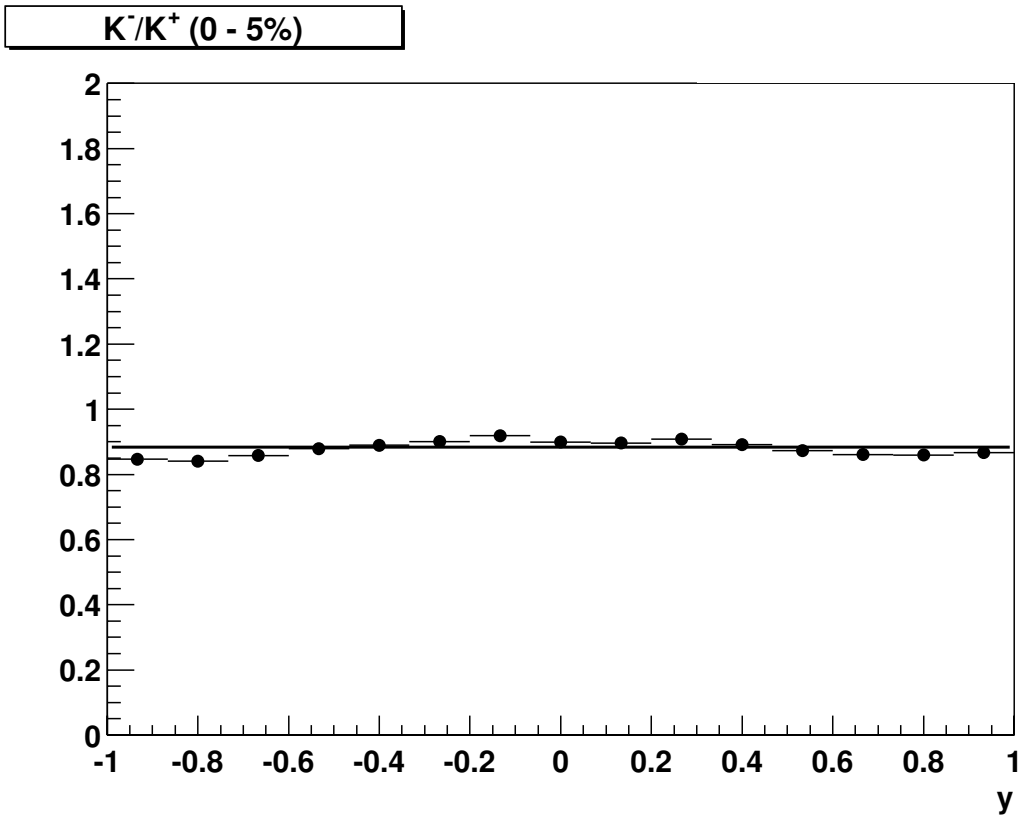

Figure 5.3: The ratio K^-/K^+ as a function of rapidity for the 5% most central collisions.

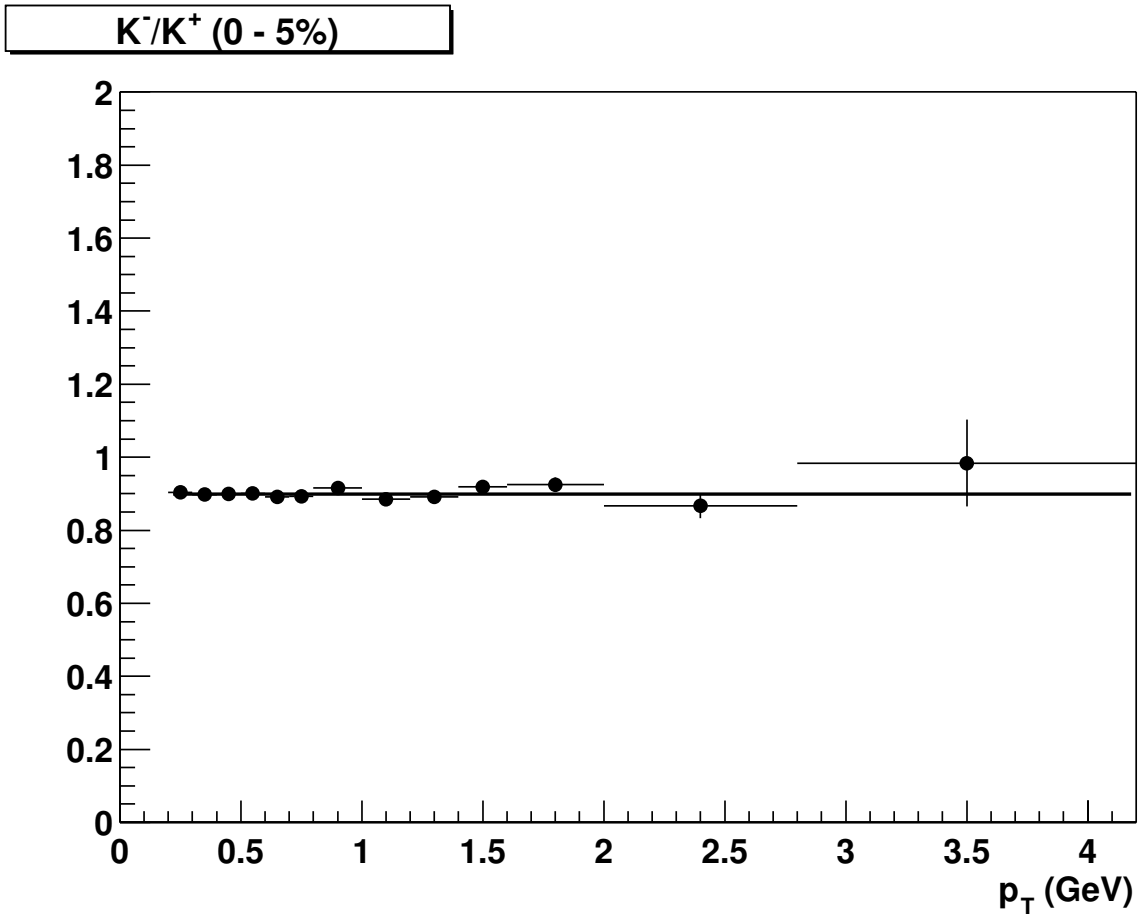

Figure 5.4: The ratio K^-/K^+ as a function of transverse momentum for the 5% most central collisions.

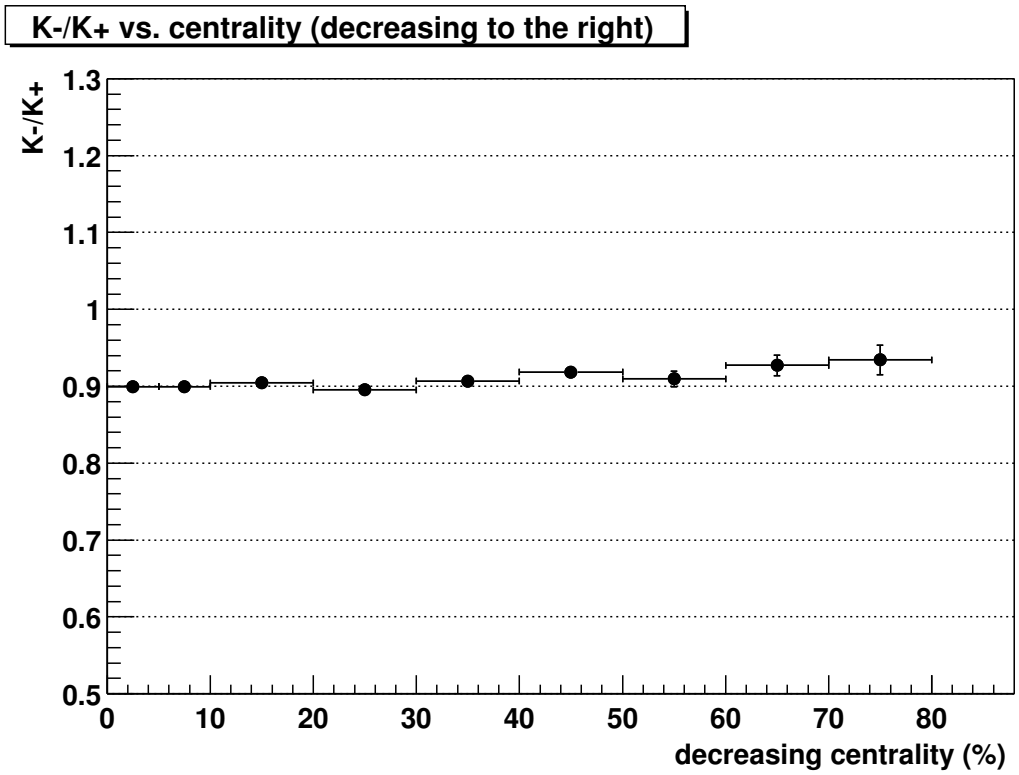

Figure 5.5: The ratio K^-/K^+ as a function of the collision centrality. The centrality is determined by the number of primary tracks at mid-rapidity

5.2.3 K^-/K^+ vs. collision centrality

Figure 5.5 shows the charged Kaon ratio as a function of collision centrality, defined as the percentage of the total Au-Au cross section of 7.2 b. The ratio displays little dependence on centrality. Since peripheral collisions closely resemble nucleon-nucleon collisions, it appears that at RHIC energies p-p collisions show a similar amount of baryon transport (stopping) as heavy ions. Naively, one would assume more baryon stopping in central heavy ion collisions, i.e. a decreasing K^-/K^+ ratio. We do see this trend somewhat, but it is not significant when systematic errors (not shown, see Chapter 4) are taken into account.

5.3 K^+ and K^- spectra

The transverse mass and transverse momentum spectra of particles are of particular interest in high energy physics. The transverse momentum is primarily generated during the collision and so provides a probe of the dynamics of the interaction. The transverse momentum is also simple to work with because it is Lorentz boost invariant. Transverse mass is defined as $m_{\mathrm{T}} = \sqrt{m^2 + p_{\mathrm{T}}^2}$.

The shape of the spectra owes its origin to two effects. First, if the initial fireball is locally thermalized, the measured particles should have a Boltzmann distribution of energy [31]:

$$\frac{1}{N}\frac{d^3N}{dp^3} = \frac{1}{4\pi m^2 T K_2(\frac{m}{T})} e^{-\frac{E}{T}} \ . \tag{5.2}$$

Using $dy/dp_z = 1/E$ and $d^2N/dp_{\mathrm{T}}^2 = d^2N/dm_{\mathrm{T}}^2$, this simplifies to

$$\frac{1}{N}\frac{d^3N}{dp^3} = \frac{1}{N}\frac{1}{Em_{\mathrm{T}}}\frac{d^3N}{dm_{\mathrm{T}}dyd\phi} = \frac{1}{N}\frac{1}{2\pi Em_{\mathrm{T}}}\frac{d^2N}{dm_{\mathrm{T}}dy} \ . \tag{5.3}$$

K_2 here is the Bessel function of the second type. The next step is to integrate over the longitudinal degrees of freedom. Various approximations are appropriate in different cases, depending on the collision details. Whatever approach we take, the result has the form

$$\frac{1}{2\pi m_{\mathrm{T}}}\frac{d^2N}{dm_{\mathrm{T}}dy} = A(m_{\mathrm{T}})^a e^{-\frac{m_{\mathrm{T}}}{T}} \ . \tag{5.4}$$

For example, if we assume that the ratio m/T is large, the power a is approximately 1/2. In a very narrow region about y=0, we can take dN/dy to be a constant. In the same region, we can also approximate $E = m_{\mathrm{T}}\, cosh(y) \approx m_{\mathrm{T}}$, which yields a power a of 1. A more realistic scenario is to consider a superposition of fireballs along the z axis, which is representative of the situation in a RHIC collision. This results in an

exponent a of 0, and we are left with a normalized pure exponential distribution of the form

$$\frac{1}{2\pi m_{\mathrm{T}}}\frac{d^2N}{dm_{\mathrm{T}}dy} = \frac{\frac{dN}{dy}}{2\pi T(T+m)}e^{-\frac{m_{\mathrm{T}}-m}{T}} \tag{5.5}$$

The thermal effect is not the only influence on the distribution, however. The interaction region has a very high hadronic density but is finite in size. As the initial fireball makes the transition back to cold hadronic matter, it is subject to large pressure gradients and begins to expand. This can lead to collective velocity, i.e. flow. Transverse flow will have more effect on the transverse spectra of heavier particles because the same collective velocity will influence their momenta more than that of lighter particles. The temperature, then, which is derived from a Boltzmann or exponential fit should not blindly be interpreted as the equilibrium temperature at thermal freeze out. In fact, in nonrelativistic terms, the temperature is increased by the kinetic energy of each particle species for the given transverse flow velocity [32]:

$$T = T_{kin} + m\langle\beta_r\rangle^2 \tag{5.6}$$

Qualitatively, this says that the temperature one measures by fitting the particle spectra has components due to the thermal freeze out temperature of the fireball and the collective transverse velocity generated by the pressure gradients in the collision region.

5.3.1 Transverse momentum spectra

The plain dN/dp_{T} spectra are in many ways the most honest way of examining the particle yields. First, they show clearly on a linear axis how much statistical error is present in the measurement and how well any fits agree with the data. Secondly, they provide a simple way to count the total particle yield, irrespective of any model.

Centrality (%)	dN/dy	$\langle p_T \rangle$
0-5	54.7708±0.570183	0.669069±0.00442267
5-10	44.474±0.635251	0.667676±0.00657332
10-20	33.1036±0.347136	0.666786±0.0046732
20-30	23.1499±0.264789	0.657877±0.00506035
30-40	15.1389±0.19856	0.649762±0.00575077
40-60	7.88472±0.105115	0.620265±0.00560017
60-80	2.31785±0.0517241	0.588098±0.00887952

Table 5.2: $\langle p_T \rangle$ in GeV and integrated yield for $(K^+ + K^-)/2$.

In Figure 5.6, we see the charge-averaged p_T spectra for seven different centrality bins. The data are smooth out to 2 GeV/c, and they are well-fit to an m_T exponential.

While the temperatures from the exponential fit do not have a direct physical interpretation, the $\langle p_T \rangle$ values and integrated yields at midrapidity (dN/dy) are very interesting quantities. The results of the fits for all seven centrality bins are shown in Table 5.3.1 and Figure 5.7. As expected, both the mean transverse momentum and integrated yield drop as the collision becomes less central. The mean p_T for the exponential distribution in Equation 5.5 is

$$\langle p_T \rangle = \frac{m^2}{m+T} e^{\frac{m}{T}} K_2(\frac{m}{T}) \tag{5.7}$$

Preliminary fits to the RHIC 200 GeV proton, pion, and Kaon spectra are consistent with a simultaneous fit of the spectra with parameters $\beta_r = 0.7 \pm 0.2$ and $T_{kin} = 110 \pm 23$ MeV. The errors are mostly systematic. [33] This explosive radial flow has a marked effect on the Boltzmann temperature (and $\langle p_T \rangle$) measured for spectra of particles with different masses. A common flow velocity corresponds to different momenta for different particle masses. This trend is seen very clearly in a plot of $\langle p_T \rangle$ vs. mass, as seen in Figure 5.8. [27]

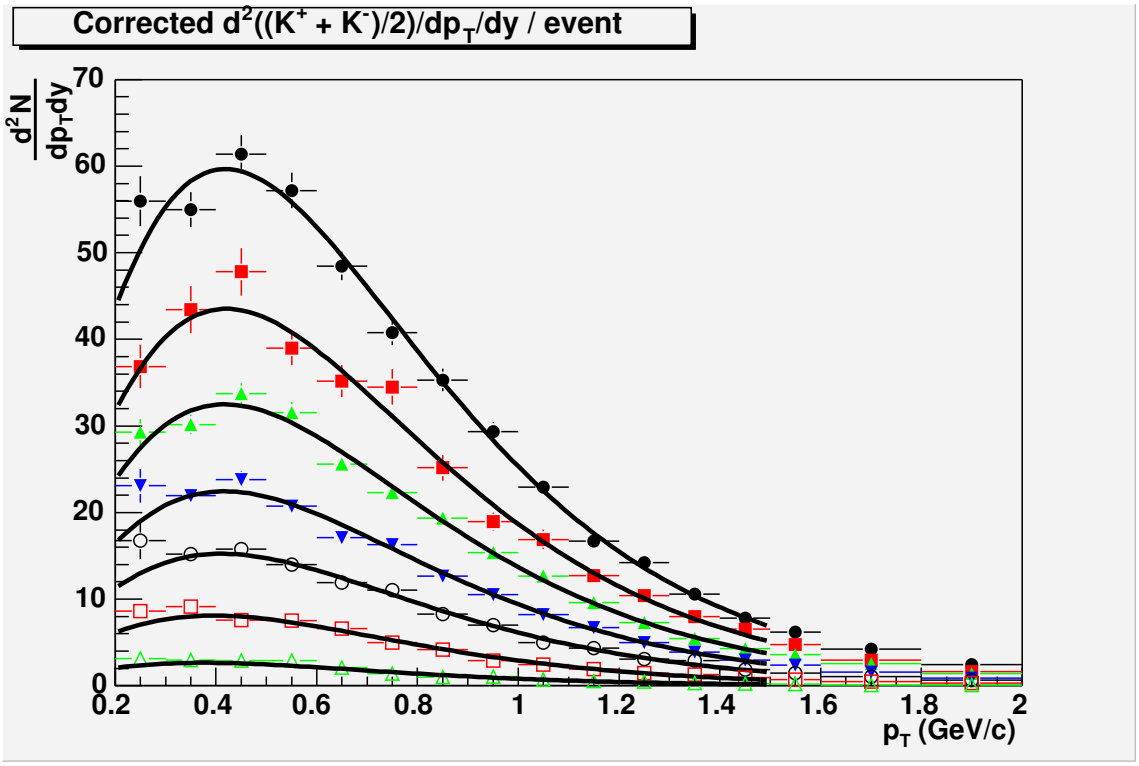

Figure 5.6: Transverse momentum spectra for different centralities. Shown are 0-5%, 5-10%, 10-20%, 20-30%, 30-40%, 40-60%, and 60-80%.

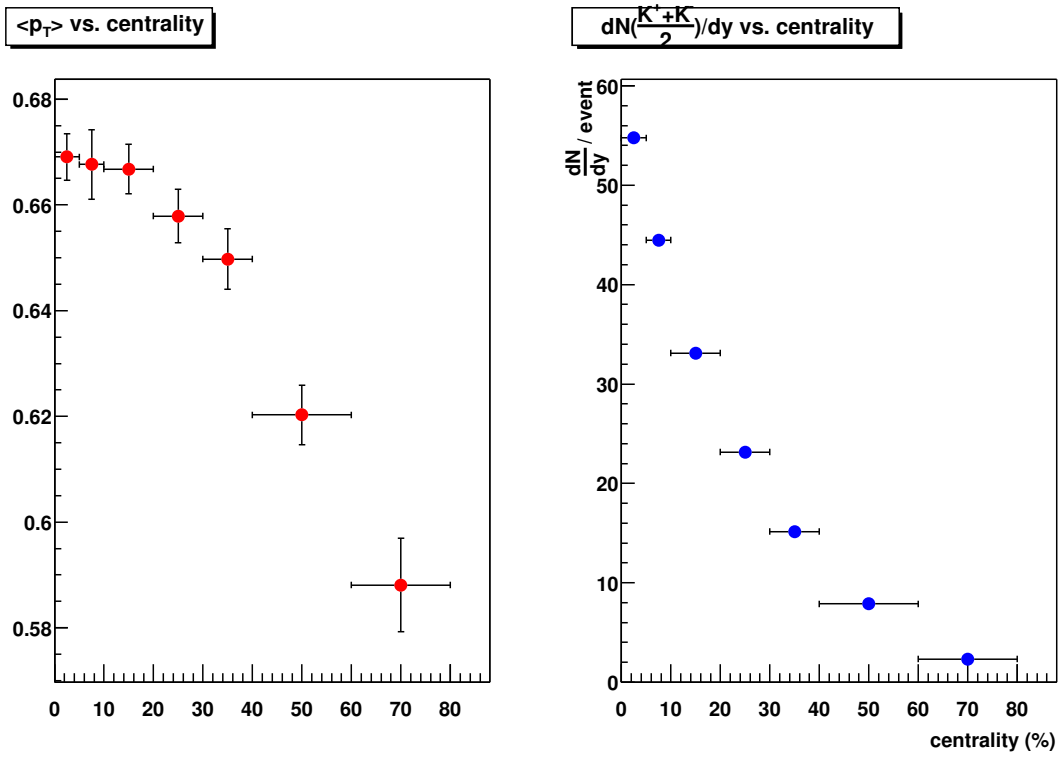

Figure 5.7: $\langle p_{\mathrm{T}} \rangle$ in GeV and integrated yield for $(K^+ + K^-)/2$. Shown are 0-5%, 5-10%, 10-20%, 20-30%, 30-40%, 40-60%, and 60-80%. Note that the horizontal axis of the $\langle p_{\mathrm{T}} \rangle$ plot is zero-suppressed, and the centrality *decreases* to the right.

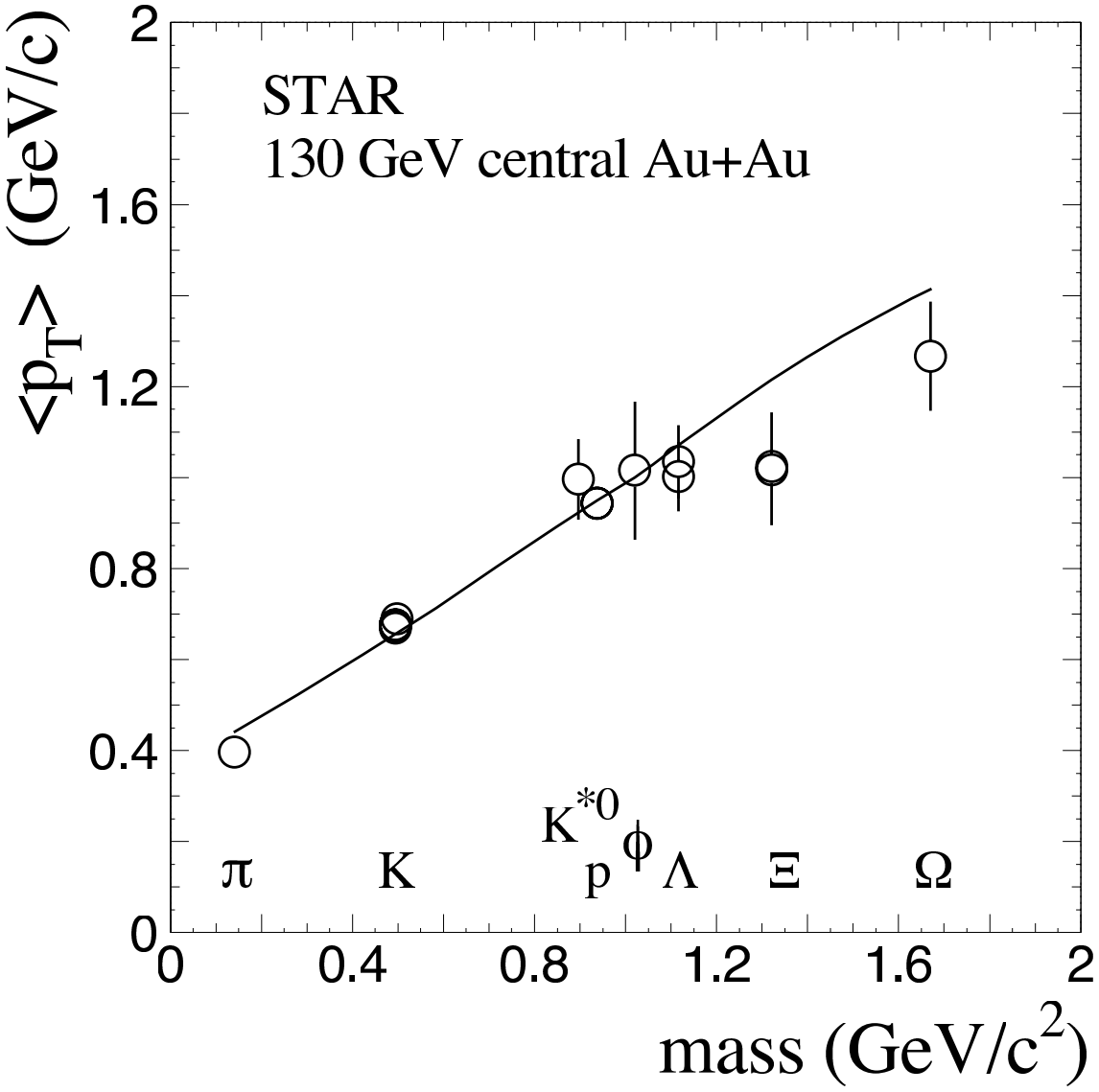

Figure 5.8: $\langle p_{\mathrm{T}} \rangle$ vs. particle mass for $\sqrt{s_{NN}}$ =130 GeV STAR data. Note the clear effect of a common velocity boost from radial flow.

5.3.2 Transverse mass spectra

The transverse mass spectra plotted on logarithmic axes give a good feel for the "temperatures" (inverse slopes) found from fits. Figure 5.9 shows the charge-averaged m_{T} spectra for the seven centrality bins. One immediately sees that the exponential fits are good out to about 1.5 GeV in p_{T} (1.1 GeV in $m_{\mathrm{T}} - m$), above which the spectra move up and away from the fit. This tail at higher transverse mass is well fit by a QCD-inspired power law. [34] Figure 5.10 shows this transition between the m_{T} exponential and the p_{T} power law. The exponent for the power law $(1/(2\pi m_{\mathrm{T}})dN/dm_{\mathrm{T}} = A(p_{\mathrm{T}})^{-B})$ is 7.8 ± 0.9(stat). This value is not compatible with $2 \rightarrow 2$ hard parton scattering; this reflects the complexity of the Au-Au collision fireball and the inevitable rescattering that occurs. [35]

5.3.3 Rapidity spectra

We have already alluded to the fact that the rapidity spectra are flat near mid-rapidity. This is shown in Figure 5.11 for the 7 centrality bins. The spectra are flat in $|y| < 0.6$ to the 10% level. Reflected across y = 0, we see at most a 5% disagreement between corresponding bins. These bins should be equal, so this 5% is a good estimate of systematic error on dN/dy.

5.3.4 Kaon to Pion ratio

The Kaon to Pion ratio, being the ratio of the lightest (and thus most numerous) strange and non-strange mesons, provides a useful probe of the relative strangeness content of the system. For more theoretical discussion, see Chapter 1.

Recall the charged Kaon production methods discussed in Chapter 1. The K^-/π^- ratio is not influenced by associated production, because the valence s quark of the

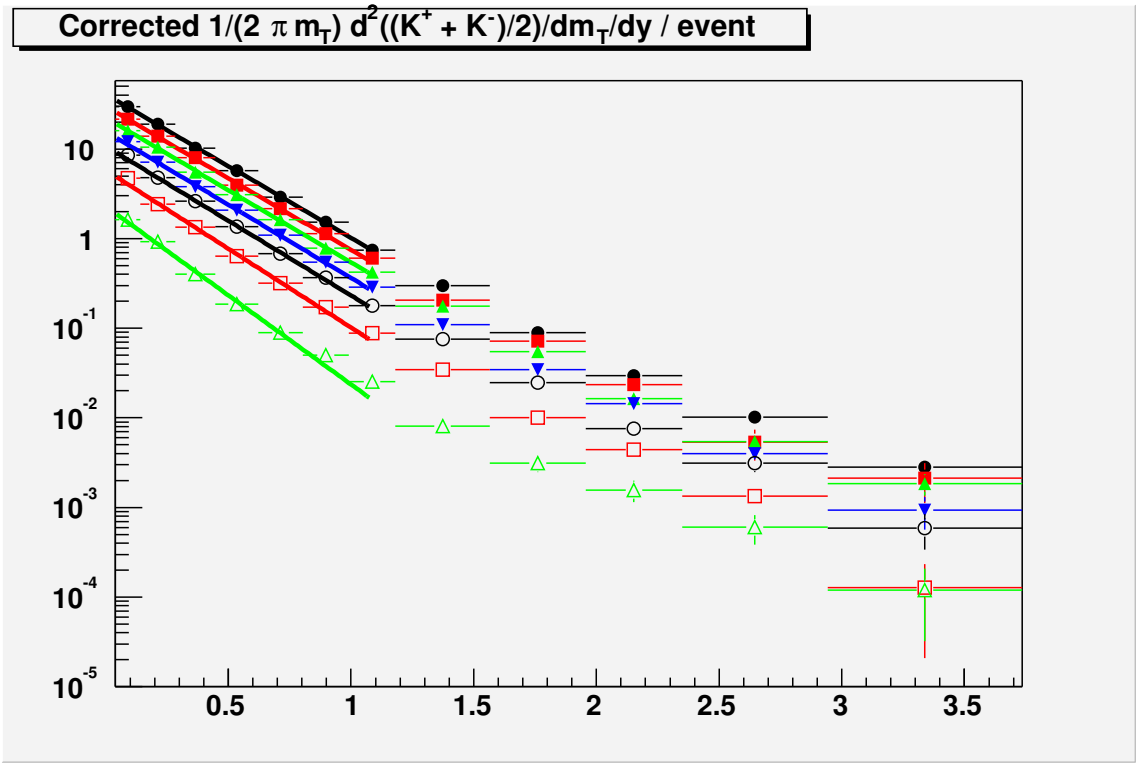

Figure 5.9: Transverse mass spectra for different centralities. Shown are 0-5%, 5-10%, 10-20%, 20-30%, 30-40%, 40-60%, and 60-80%.

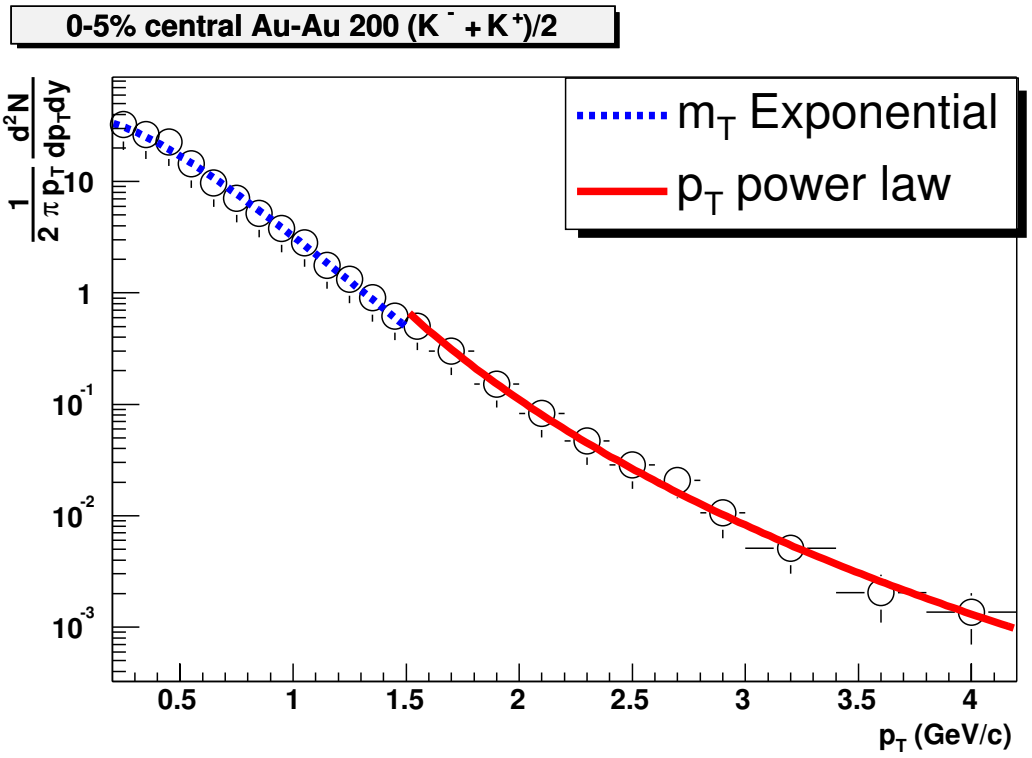

Figure 5.10: Two different fits shown to emphasize the m_{T} exponential shape of the spectra at low momentum and the p_{T} power law at high momentum.

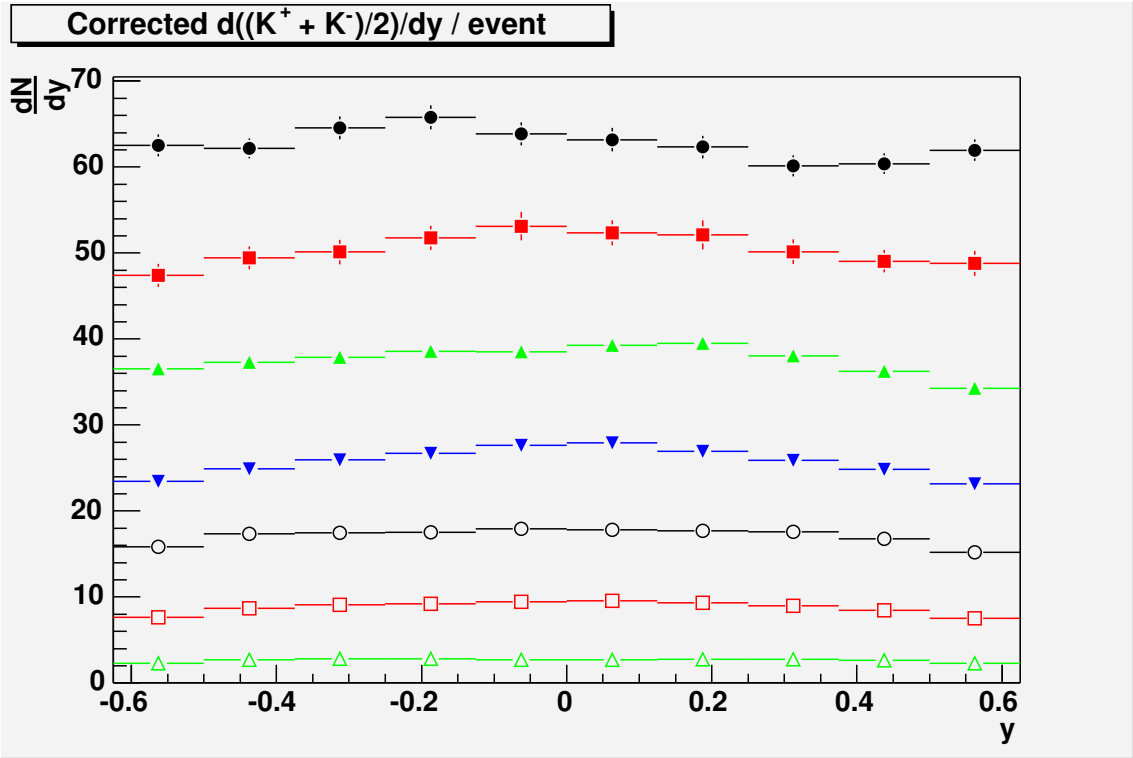

Figure 5.11: Rapidity spectra for different centralities.

K^- does not come from transport of baryon number from the initial collision (in contrast with the valence u quark of the K^+). That ratio, then, is determined entirely by the increase of pair production and should increase monotonically with collision energy. K^+/π^+, on the other hand, has contributions from both the increasing temperature and decreasing baryon density. Both ratios are shown in Figure 5.12. We see the monotonic behavior of K^-/π^- with respect to the CM energy, and the more complicated behavior of K^+/π^+ as the baryon number decreases with increasing $\sqrt{s_{NN}}$ after initially peaking. In addition to preliminary STAR p-p data at 200 GeV and Au-Au data at 130 [36] and 200 GeV, Figure 5.12 also shows parameterized p+p data (curves) and data from p+p [3, 4] and $\overline{\text{p}}$+p [37] at higher energies. Our measurement indicates a 50% enhancement over $(K^+ + K^-)/2\langle\pi\rangle$ in p+p and $\overline{\text{p}}$+p collisions at similar energies. The enhancement in K^-/π is similar at SPS and RHIC, while that in K^+/π is larger at lower energies due to the effect of a changing net-baryon density. We see the monotonic behavior of K^-/π^- with respect to the CM energy, and the more complicated behavior of K^+/π^+ as the decreasing baryon number quenches the rapid increase seen at low $\sqrt{s_{NN}}$.

This picture is consistent with the observed decrease in baryon density with increasing $\sqrt{s_{NN}}$ in heavy ion collisions. [38] The K^+/π^+ ratio peaks at $\sqrt{s_{NN}}$ of 6-7 GeV, indicating a maximum in the baryon density there. This maximum strangeness enhancement in the light mesons can be described by the effect of *canonical suppression*. [39] This refers to the suppression of strange particles in systems of small size or low temperature, where canonical statistics must be used to accurately represent the strangeness content. It is more difficult to make strange particles with exact local quantum number conservation (canonical ensemble) than with global conservation

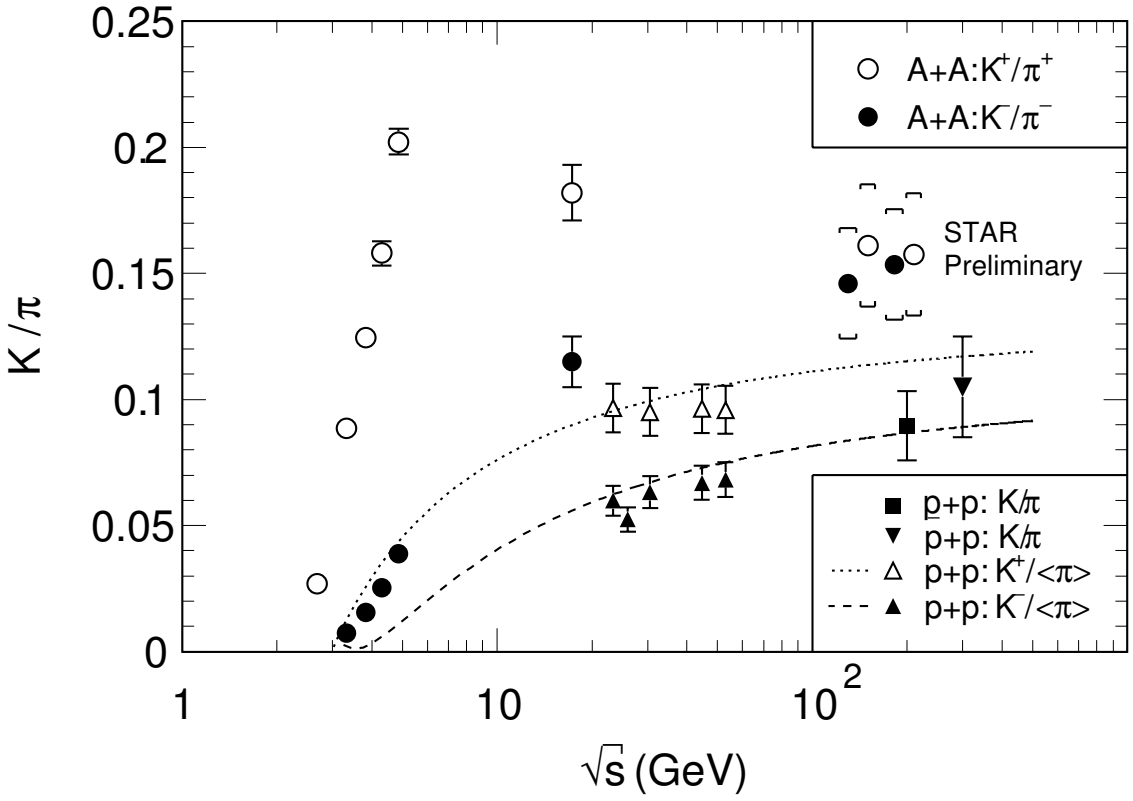

Figure 5.12: Kaon to Pion ratios versus center of mass energy.Mid-rapidity K/π ratios versus $\sqrt{s_{NN}}$. The curves are parameterizations to p+p data [3, 4]. The error bars show statistical errors. The systematic errors on the STAR data are indicated by the caps. The STAR Au-Au K^+/π points are displaced in $\sqrt{s_{NN}}$ for clarity.

(grand canonical ensemble).

5.4 Central to peripheral comparison

One very interesting probe of particle production mechanisms is to examine the momentum spectra of particles as a function of centrality. This has the effect of switching on and off any effects that may be due to the medium. The most central collisions should show the largest influence of the medium, if any such effect is present. As a concrete example, let us form the ratio of central to peripheral spectra. Each spectrum is scaled by the number of binary nucleon-nucleon collisions (NBC) for that centrality bin, which is found from Glauber model calculations. This model yields $\langle N^{\text{central}}_{\text{binary collisions}} \rangle = 351.96^{+1.53}_{-1.04}$ and $\langle N^{\text{peripheral}}_{\text{binary collisions}} \rangle = 19.75^{+3.8}_{-5.66}$.

$$R_{CP}(p_{\mathrm{T}}) = \frac{\langle N^{\text{peripheral}}_{\text{binarycollisions}} \rangle}{\langle N^{\text{central}}_{\text{binarycollisions}} \rangle} \frac{d^2N^{\text{central}}/dp_{\mathrm{T}}dy}{d^2N^{\text{peripheral}}/dp_{\mathrm{T}}dy} \tag{5.8}$$

At low momentum, we expect bulk effects to dominate, so the spectra should scale as the number of participant nucleons (N_{part}). At high momentum, hard scattering is more important, so scaling with binary collisions should dominate. What we show in Figure 5.13 is the ratio of the 0-5% central p_{T} spectra divided by the 60-80% spectra for charged Kaons. The two bands represent the binary and participant scaling lines and the error from the Glauber model. The ratio and both scaling lines are normalized to the number of binary collisions.

One quantity such a ratio can probe is the opacity of the initial fireball to hard scattered partons. High momentum hadrons are produced by the fragmentation of parton jets; one might naively expect the number and magnitude of these jets to increase with increasing collision centrality. This is exactly what was was observed at the SPS [40], in that R_{CP} continued to increase with increasing p_{T}. There is an

effect which can counter the higher energy density, however. If the medium of the fireball exhibits some degree of color deconfinement, the hard scattered partons lose significant energy before fragmentation into hadrons because they radiate gluons in the color-charged medium.

At RHIC, one observes definite suppression of high momentum hadrons in central Au-Au data. The effect is present in all identified particle species individually. We see it clearly in the Charged Kaon spectra presented here.

The changeover from soft to hard physics with increasing momentum, however, provides a number of complications in understanding the source of this suppression. [41] For example, collective radial flow as mentioned above may result in a significant modification of transverse momentum spectra in Au-Au collisions relative to N-N. To separate this effect from a QCD hard processes, it is important to look at N-Au collisions. We expect the coming STAR d-Au data to be very important in this respect.

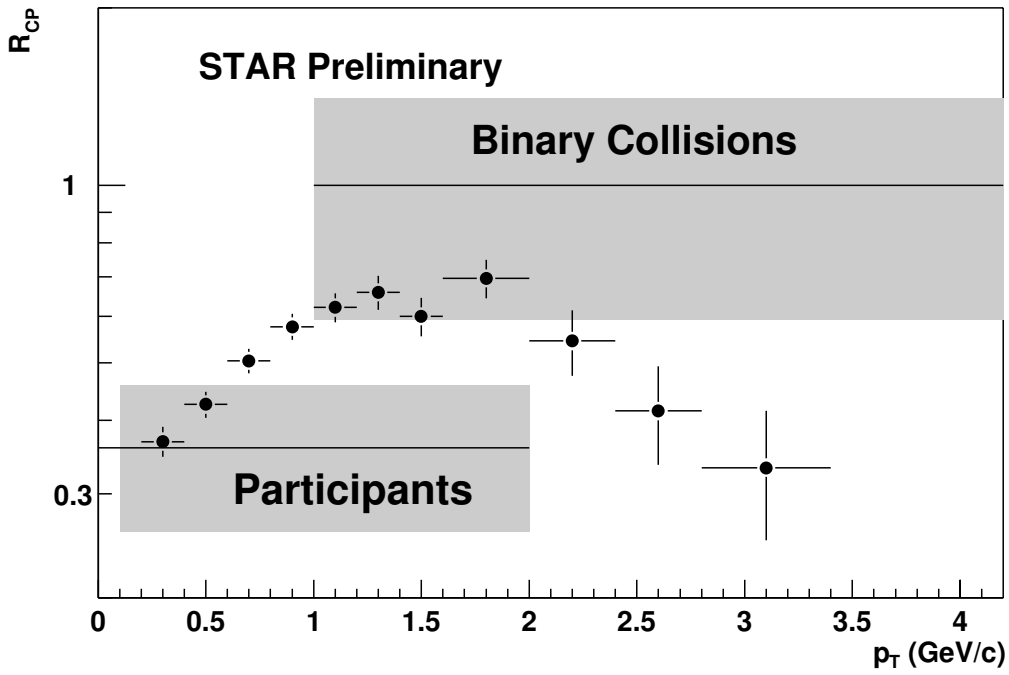

Figure 5.13: R_{CP} for $K^+ + K^-$: Central $\equiv$ 0-5%, Peripheral $\equiv$ 60-80%. Shaded bands are binary scaling (upper) and participant scaling (lower).

Conclusions

We have discussed the results of charged Kaon production in Au-Au collisions of $\sqrt{s_{NN}}$ =200 GeV at RHIC. These results stand out because they offer high quality particle spectra to transverse momentum beyond 4 GeV. The salient points are as follows:

- A ratio K^-/K^+ of 0.9 in central data indicates a nearly baryon-free environment at RHIC.
- This ratio is flat out to p_{T} of 4 GeV/c.
- Thermal fits to particle ratios result in $\mathrm{T_{ch}}$ =177 MeV and μ_{B} =29 MeV.
- Kaon spectra exhibit a high apparent temperature. The increase of $\langle p_{\mathrm{T}} \rangle$ with centrality indicates radial flow. Simultaneous fits to particle spectra result in $\mathrm{T_{kin}}$ =110 MeV and $\langle \beta \rangle$ =0.7, indicating explosive radial expansion
- The K/π ratio is approximately 60% higher in Au-Au than p-p at RHIC. The RHIC heavy ion ratio is about the same as that seen at the SPS.
- High p_{T} Kaons are suppressed in central collisions relative to peripheral, a signal of a possible strong medium effect. d-Au data will help determining whether this is an initial or final state effect.

Appendix A

Reconstruction of the Charged Kaon Lifetime

A.1 Introduction

The determination of the proper mean lifetime for charged Kaons in STAR is complicated by both limited lifetime acceptance and momentum-dependent cuts. A number of more elegant mathematical approaches were investigated to compensate for these effects, but in the end it was seen that the simplest and most reliable approach is a thorough analysis of simulated tracks embedded in a real event. This approach should be effective in any collider experiment.

A.2 Lifetime Acceptance in STAR

The proper lifetime of a particle is simply related to its lifetime, t_L, and velocity, v, in the laboratory by

$$t_0 = \frac{t_L}{\gamma}, (\gamma \equiv \frac{1}{\sqrt{1-\beta^2}}, \beta \equiv \frac{v}{c}) \ . \tag{A.1}$$

The time in the laboratory is related to the distance traversed by the particle by $t_L = s/v = s/(\beta c)$, so the proper lifetime can be expressed in terms of the distance traversed in the laboratory and the particle's mass, m, and momentum, $p = mv\gamma$, as:

$$ct_0 = \frac{s}{\beta\gamma} = s\frac{mc^2}{pc} \ . \tag{A.2}$$

The mean proper lifetime of the charged Kaon is $c\tau = 371.3$ cm. The fiducial volume in STAR that is searched for kink decays is 133 cm $<$ r $<$ 179 cm. Given these radial

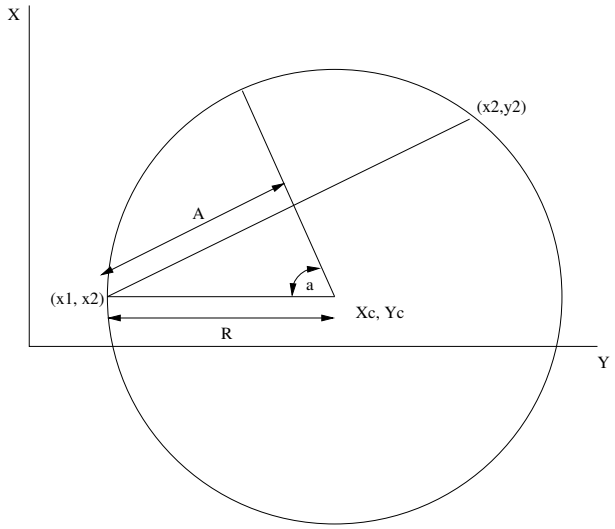

Figure A.1: Transverse projection of helix

limits, it is useful to find a simple expression for the path length traversed between two points by a helix representing a particle with charge q, total momentum p, and transverse momentum $p_{\mathrm{T}} \equiv |\overrightarrow{p} \times \hat{z}|$ given a magnetic field $\overrightarrow{B} = B\hat{z}$. The *dip angle* of the helix is $\lambda = \arccos \frac{p_{\mathrm{T}}}{p}$.

As a practical matter, STAR tracking does not find tracks which cover more than half the period of the helix. This is because track finding is done from the outside of the TPC in, and so all tracks are monotonically increasing in the radial direction. This greatly simplifies the task of finding path length along a track; we need only know their separation in the transverse plane ($2A$ in Figure A.1). It is easy to see that the azimuthal angle between the points $(x1, y1)$ and $(x2, y2)$ relative to the helix axis is $a = \arcsin \frac{A}{R}$ and so the path length in the transverse plane is $s_t = 2R \arcsin \frac{A}{R}$. $R = p_{\mathrm{T}}/qB$ here is the radius of curvature of the helix. The full path length then is just

$$s = \frac{s_t}{\cos\lambda} = 2\frac{p_{\mathrm{T}}}{qB} \arcsin A\frac{qB}{p_{\mathrm{T}}}\frac{p}{p_{\mathrm{T}}} = \frac{2p}{qB} \arcsin A\frac{qB}{p_{\mathrm{T}}} \,. \tag{A.3}$$

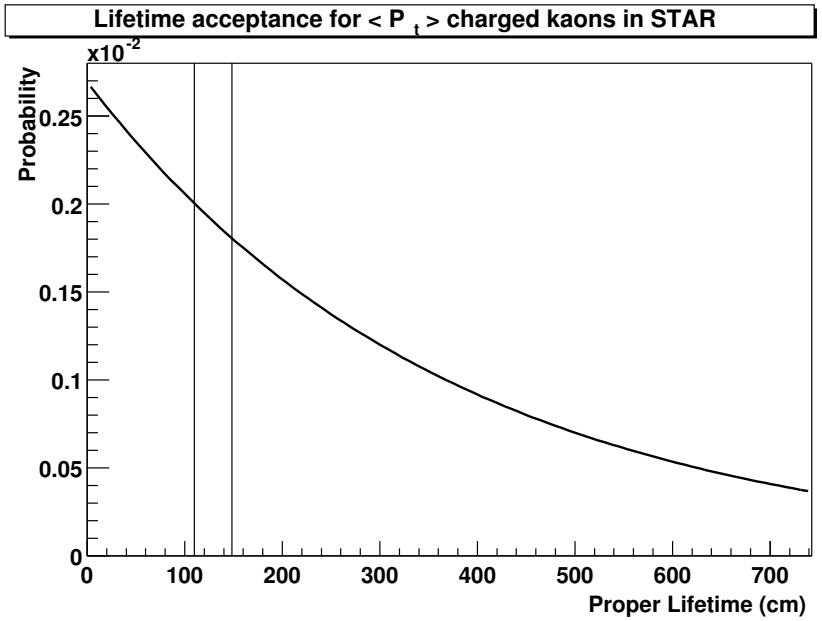

Figure A.2: STAR lifetime acceptance for $\langle p_{\mathrm{T}} \rangle$ charged Kaons

This translates readily into lifetime:

$$ct = \frac{mc^2}{pc}\frac{2p}{qB}\arcsin A\frac{qB}{p_{\mathrm{T}}} = \frac{2mc}{qB}\arcsin A\frac{qB}{p_{\mathrm{T}}} \,. \tag{A.4}$$

Note: This formula assumes nonzero p_{T}. The TPC doesn't see tracks with $p_{\mathrm{T}} = 0$, so this is fine.

Full magnetic field strength in STAR is $B = 0.5$ T $= 5$ kG $= 5\mathrm{x}10^{-14}$ $\frac{\mathrm{GeV\,s}}{\mathrm{cm}^2} = 0.0015$ $\frac{\mathrm{GeV/c}}{\mathrm{cm}}$. Thus a mid-rapidity charged Kaon in STAR that originates at the beam line and has mean p_{T} ($\langle p_{\mathrm{T}} \rangle \approx 600$ MeV) will enter and leave the fiducial volume after traveling 133.6 cm and 180.5 cm, respectively.

Since the charged Kaon mass is $m = 493.7$ MeV$/c^2$, these correspond to proper lifetimes, ct_0, of 109.9 cm and 148.5 cm, or 0.3 and 0.4 of the mean proper $c\tau$ for charged Kaons. One can see in Figure A.2 how limited this range of 0.1 $c\tau$ is. We shall see later on how this renders ineffective some techniques for finding the lifetime.

A.3 Fitting with Maximum Likelihood

This is a summary and application of the Maximum Likelihood fitting method described in Reference [42]. Note that the example in the book deals with V_0 particles in a fixed target experiment, where one typically has shorter lifetimes and larger acceptances. First we look at the probability of one *event* , an observed particle in the detector, has a lifetime t_i. (*Proper* lifetime will be implied for the rest of the discussion.) We factor the probability in terms of observation probability and lifetime probability. The probability of observing a particle with mean lifetime τ, momentum $\overrightarrow{p_i}$, and position $\overrightarrow{r_i}$ multiplied by the conditional probability that the observed particle has a given lifetime is equal to the probability that the particle has a given lifetime (whether observed or not):

$$P(observation)P(observation \mid lifetime\ t_i) = P(lifetime\ t_i) \tag{A.5}$$

$$\Rightarrow P(observation \mid lifetime\ t_i) = \frac{1}{P(observation)} P(lifetime\ t_i) \tag{A.6}$$

$$\Rightarrow P_i = A_i \frac{e^{-\frac{t_i}{\tau}}}{\tau}\ , \tag{A.7}$$

where A_i is a factor representing the detector efficiency. In this case A_i^{-1} is the probability that a particle having mean lifetime τ, momentum $\overrightarrow{p_i}$, and position $\overrightarrow{r_i}$ will be observed to decay in the detector. $e^{-\frac{t_i}{\tau}}/\tau$ is the probability that a particle having mean lifetime τ will live time t_i.

Since an event *did* occur (we observed a particle with properties τ, $\overrightarrow{p_i}$, $\overrightarrow{r_i}$), we can say that the integral of P_i over all observable lifetimes for a given τ, $\overrightarrow{p_i}$, and $\overrightarrow{r_i}$ must be unity. This allows us to determine A_i:

$$1 = \int_{t_i^{min}}^{t_i^{max}} P_i dt \tag{A.8}$$

(A.9) $$\Rightarrow A_i^{-1} = (e^{-\frac{t_i^{min}}{\tau}} - e^{-\frac{t_i^{max}}{\tau}}) \ .$$

The upper and lower limits on the integral are functions of $\overrightarrow{p_i}$, $\overrightarrow{r_i}$, and the detector *fiducial volume* , the region where particles may be detected. Let us examine the specific example of charged Kaon decays in STAR. Here, the fiducial volume, as mentioned above, is $133\,\mathrm{cm} < r < 179\,\mathrm{cm}$. That means that we can express the integral limits using Equation A.4 as

(A.10) $$ct_i^{min} = \frac{2mc}{qB} \arcsin\,(\frac{r^{min}}{2}\frac{qB}{p_{\mathrm{T}}^i})$$

(A.11) $$ct_i^{max} = \frac{2mc}{qB} \arcsin\,(\frac{r^{max}}{2}\frac{qB}{p_{\mathrm{T}}^i}) \ .$$

Now that the individual decay probabilities have been determined, we can look at the *joint probability* associated with a set of events. This is just the probability of N events occurring concurrently and is called the the *likelihood function*:

(A.12) $$L \equiv \prod_{i=1}^{N} P_i = \tau^{-N} e^{\frac{-1}{\tau}\sum_{i=1}^{N} t_i} \prod_{i=1}^{N} A_i \ ,$$

As a practical matter, this number will be very small for large N, and on a computer it is more useful to consider the logarithm of the likelihood function:

(A.13) $$M \equiv \ln L = -N \ln \tau - \frac{1}{\tau}\sum_{i=1}^{N} t_i + \sum_{i=1}^{N} A_i \ ,$$

The likelihood function can be used to determine any parameter in the probability distributions. For our purposes, we wish to find which value of the mean lifetime τ maximizes L (or M). We know that the observed events *did* occur and so the τ' which maximizes M is the most probable value. Furthermore, for a large number of events L is Gaussian around the most probable value of a parameter,which allows one

to extract the uncertainty in the parameter as well:

$$L(\tau) \propto e^{-\frac{(\tau-\tau')^2}{2\sigma^2}} \tag{A.14}$$

$$M(\tau) = -\frac{(\tau-\tau')^2}{2\sigma^2} + constant\ , \tag{A.15}$$

The general procedure when looking at experimental data is as follows:

1. Select a set $\{\tau_j\}$ of trial mean lifetimes in the vicinity of the hypothesized value of τ.

2. For each τ_j, calculate $M(\tau_j)$ as shown in Equation A.15.

3. Take the exponential of M to get L and fit L to a Gaussian near its peak. This will yield the most likely value, τ', for the mean lifetime and the uncertainty in that value.

In Figure A.3, we show the results of the method applied to simple one dimensional Monte Carlo data which was thrown with flat momentum and a mean lifetime of τ_K. In many situations, this give excellent results. If the range of experimentally observed lifetimes is large relative to the mean lifetime, the correct mean lifetime can be extracted from a small number (1000) of events. This can be seen in the topmost figure. For very narrow lifetime acceptance, however, as many as a million events are needed for the method to converge. One can from the bottom figures see the that the correct lifetime is not reproduced for even 100 thousand events.

There is even more to the story, however, as the method described above assumes perfect efficiency within the detector fiducial volume. This is not the case

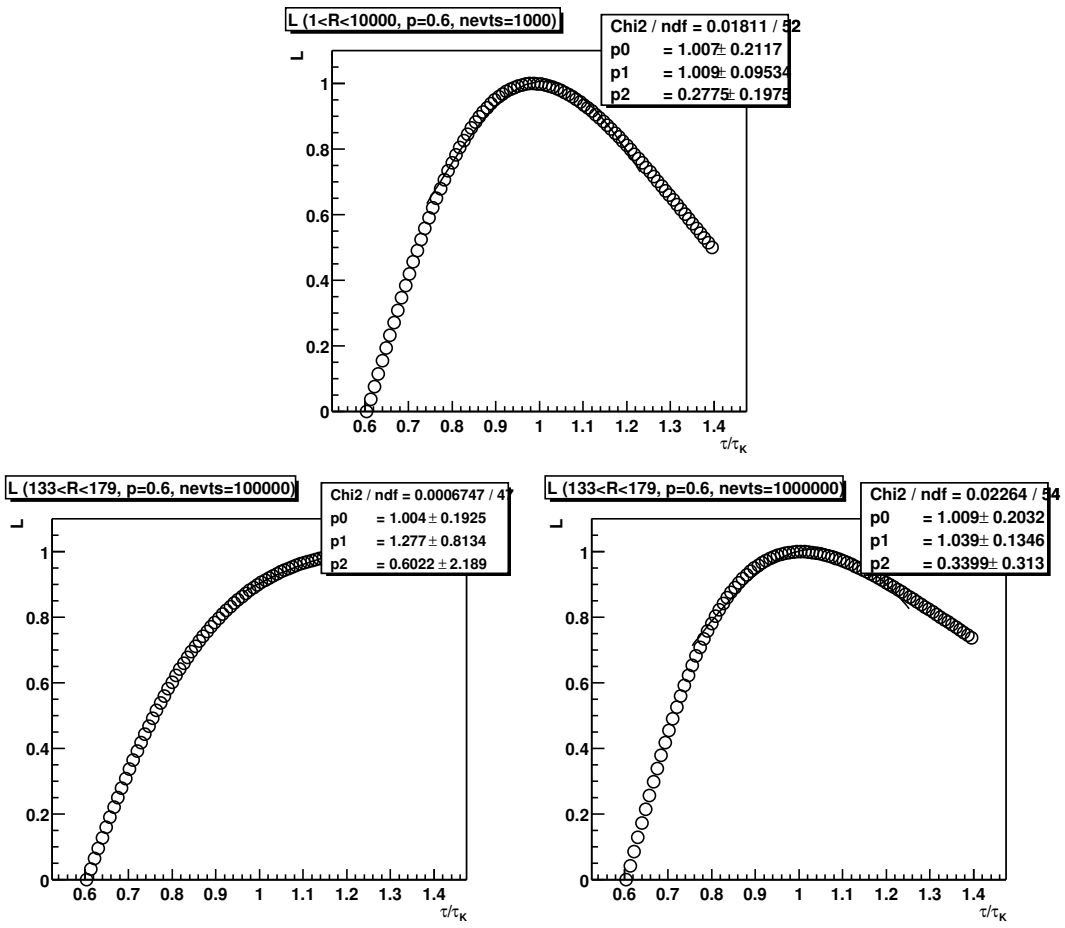

Figure A.3: Gaussian fits to likelihood function (p1=center, p2=width)

in STAR because 1) not all decays in the fiducial are reconstructed and 2) momentum dependent cuts are applied in order to separate Kaon signal from correlated and combinatorial background. The second factor in particular biases the observed lifetime distribution a great deal because momentum dependence translates directly into lifetime dependence for a fixed acceptance.

A.4 Fitting with Virtual Particles

This method attempts to restore the signal which is lost outside of the fiducial volume. It proceeds as follows:

1. For each event (detected Kaon), calculate the lifetime acceptance based on its momentum and the coordinate-space acceptance. In STAR, for example, this involves finding the upper t_{max} and lower t_{min} lifetime limits based on the outer and inner radii of the fiducial volume using Equation A.4.

2. Using simple Monte Carlo, generate two virtual particles using the ideal lifetime distribution (Equation A.7) and the accepted value for the charged Kaon mean lifetime. The first particle should have lifetime $0 < t_{under} < t_{min}$ and the second should have lifetime $t_{max} < t_{over} < \infty$. These particles will represent particles which have fallen outside the detector acceptance

3. Weigh the three particles by the integral of the probability distribution in each region:

(A.16) $$w = \int_{t_{min}}^{t_{max}} \rho(t)dt$$

(A.17) $$w_{under} = \int_{0}^{t_{min}} \rho(t)dt$$

$$w_{over} = \int_{t_{max}}^{\infty} \rho(t)dt \tag{A.18}$$

4. Fill the lifetime histogram (dN/dt) with the lifetimes for the real event and the two virtual particles, weighted as above. The weights above ensure that the virtual particles will fall into the ideal lifetime distribution relative to the weight of the ideal particles. Fitting this histogram will extract the mean lifetime.

This method reproduces the ideal lifetime distribution for ideal Monte Carlo events, but it faces certain complications for real data. Firstly, it shares the problem of efficiency with the Maximum Likelihood method above because it assumes 100% reconstruction of particles in the fiducial volume. Secondly, it is seriously affected by the limited lifetime acceptance of STAR. The virtual particles which are generated for each real particle have weights much greater than the weight of the real particle. That means that the real signal is overpowered by the virtual particles, and the hypothesized mean lifetime is always reproduced, regardless of the lifetime of the real particles.

This situation can be seen in Figure A.4, which shows the results of applying this method to simple Monte Carlo data in the STAR fiducial volume. Particles with monochromatic momentum were thrown according to an input mean lifetime. Acceptance cuts were then applied to coincide with the fiducial. This data is labeled "uncorrected" in the histograms. The data labeled "corrected" includes both the input particles and virtual particles thrown according to the hypothesized mean lifetime. The histograms on the right show the result of an input mean lifetime τ_K equal to the hypothesized mean lifetime. Those on the left show the same exercise with an input mean lifetime of 3 times that of the hypothesized lifetime. In both

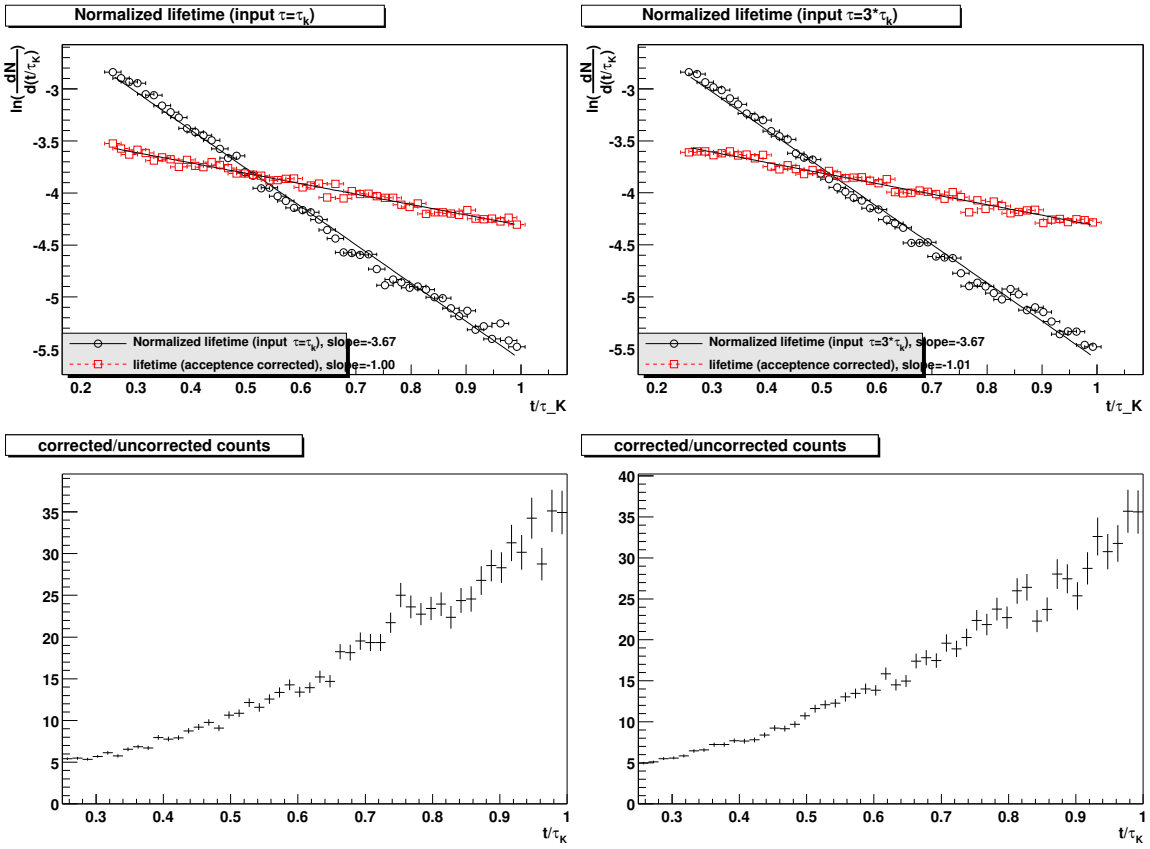

Figure A.4: Results of Fitting with Virtual Particles

cases, the lower histograms show that the sum of the virtual and input particles is much greater than the input particles alone. This is seen clearly in the upper figures, which show that in both cases, the "corrected" data follows the hypothesized lifetime distribution. The mean lifetime of the input particles is not recovered.

A.5 Fitting with Momentum Integral Weighting

This is one method which is not susceptible to the limited lifetime acceptance in STAR, but it does make certain assumptions. For each input particle, we calculate its momentum acceptance from its lifetime and the coordinate space acceptance. This

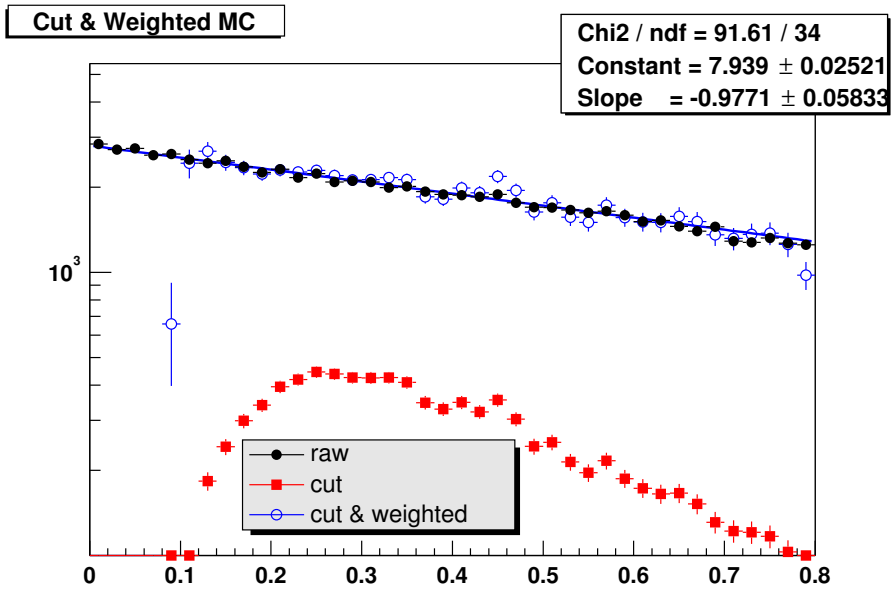

Figure A.5: Lifetime distribution ($c\,\tau$) after momentum integral weighting to recover input slope ($c\,t_0 = 1$)

requires knowledge of the input momentum distribution:

$$P(p_{min} < p < p_{max}) = \int_{p_{min}(r_{min},t)}^{p_{max}(r_{max},t)} \rho(p)dp \tag{A.19}$$

Then we simply weigh the lifetime of each particle with the inverse of this probability when filling the lifetime histogram, effectively correcting for the coordinate space acceptance in momentum space. If the input momentum distribution is know, this approach works, as see in Figure A.5. The closed circles are the input Monte Carlo distribution. The closed squares are that distribution after fiducial cuts. The open circles are the cut distribution after weighting by the momentum integral. The slope is fit from this weighted distribution, and comes out very close to 1 (the input slope).

The weakness of this approach is that in practice the input momentum distribution is not known, in particular when momentum Dependant cuts are applied. It fails when applied to STAR data.

A.6 Correcting Data Using Embedding

Besides the problem of limited lifetime acceptance, a common flaw in the approaches presented above is that they assume perfect efficiency in the fiducial volume. Since we do not have perfect detection efficiency, we must use simulated data to calculate it. One can use embedded data (Monte Carlo tracks propagated through the detector and placed inside real events) to determine the efficiency by looking at how many of the Monte Carlo tracks in the fiducial volume are reconstructed. One could, for example, determine the coordinate space efficiency and then use the maximum likelihood method. Or the momentum efficiency could be calculated and used with the momentum weighting method above. But one could just as easily calculate the lifetime efficiency directly ($dN_{reconstructed}/dN^{Decayed}_{Embedded}$) and use that to correct the raw lifetime distribution without any more effort. In the end, this was our approach. Figure A.6 shows our results using the embedding lifetime efficiency correction applied to year 2000 data. The ratio of the mean lifetime from the fit to the PDG lifetime is very close to 1. Note that Kaons with shorter proper lifetime only reach the STAR fiducial volume if they have high p_{T}. For example, Equation A.4 shows that a Kaon with $ct = 20$ cm must have $p_{\mathrm{T}} = 3.3$ GeV/c to reach the fiducial volume ($R = 133$ cm). The Kaon signal at larger momentum has higher contamination and is eliminated from the lifetime fit here.

A.7 Summary

Several analytical methods were investigated to recover the mean proper lifetime for charged Kaons including Maximum Likelihood, Virtual Particles, and Momentum

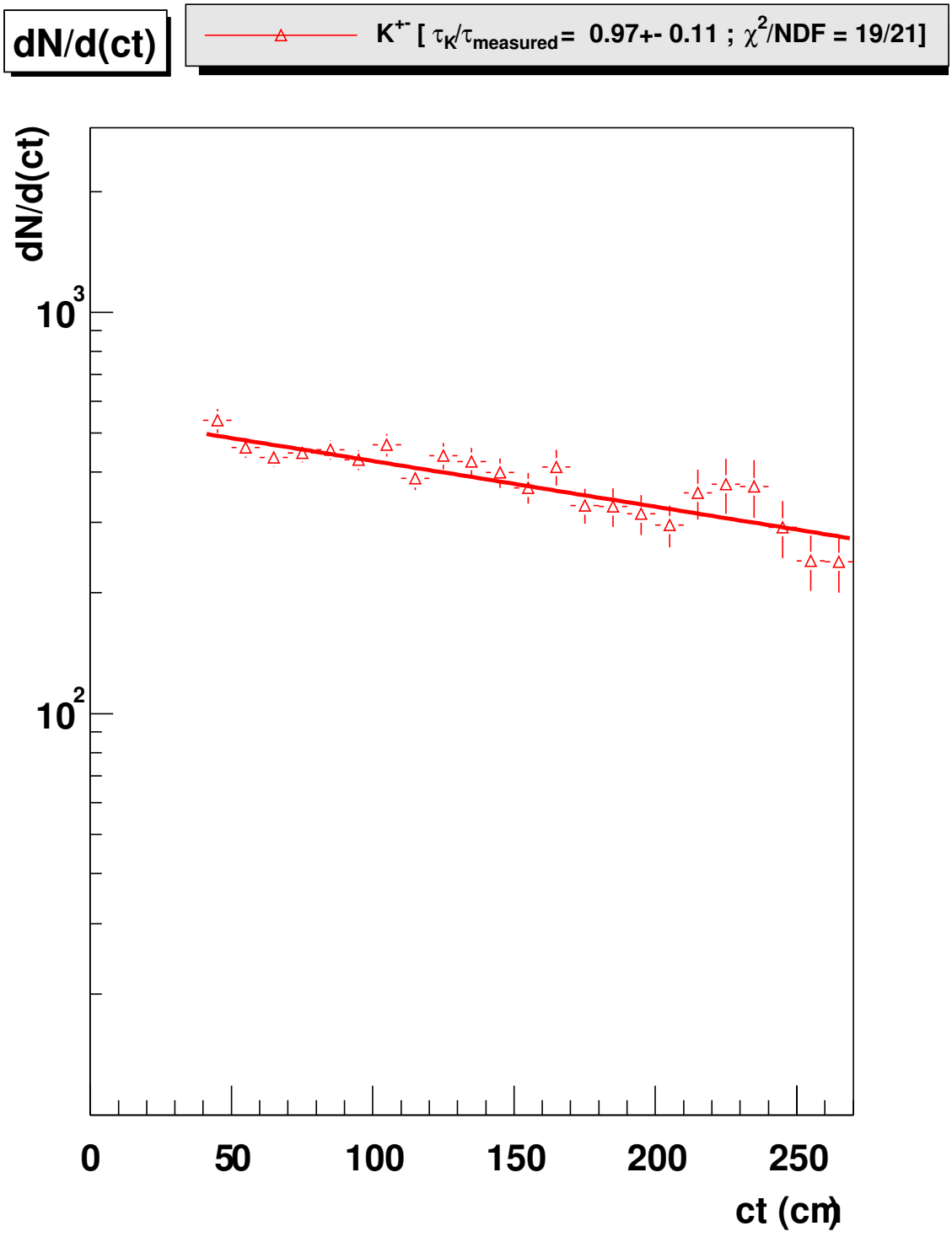

Figure A.6: Results of Efficiency/Acceptance Correction from Embedding

Integral Weighting. Due to limited acceptance and complicated momentum dependencies of the analysis cuts, none of these methods produces satisfactory results. The weighting function must be produced from detailed simulation of Kaon decays; this method reproduces very well the accepted value of the proper mean lifetime and should be applicable for any collider experiment.

Appendix B

Kinematics of the Charged Kaon Decay

B.1 Introduction

Understanding the kinematics of the charged Kaon decay is very important to isolating that decay from the numerous sources of background. Here we study the decay kinematics for the dominant $K^+ \to \mu^+\nu_\mu$ (63.5%) decay mode.

B.2 Center of Mass Frame

In the CM frame (where the parent Kaon has zero momentum), the momenta of the daughter Muon and Neutrino are equal and opposite. Furthermore, the magnitude of the daughter momenta is fixed by the particle masses. The following relations, which are found by energy and momentum conservation in the CM frame, are good for any 2 body decay where one daughter is massless, such as $\pi^+ \to \mu^+\nu_\mu$.

$$\begin{aligned} p^{CM}_{daughter} &= \frac{m^2_{parent} - m^2_{daughter}}{2m_{parent}} \\ E^{CM}_{daughter} &= \frac{m^2_{parent} + m^2_{daughter}}{2m_{parent}} \,. \end{aligned} \tag{B.1}$$

Note that the decay angle is homogeneous over 4π solid angle in the CM frame. I.e., $\rho(\Omega)d\Omega = \frac{1}{4\pi}d\Omega$, where $d\Omega = \sin\theta d\theta d\phi$. For simplicity, we take z to be the direction of parent motion. Thus the probability of a certain CM decay angle (for the charged, massive daughter) is

$$\rho(\theta)d\theta = \int_0^{2\pi} \frac{1}{4\pi}\sin\theta d\theta d\phi = \frac{\sin\theta}{2}d\theta \,. \tag{B.2}$$

B.3 Lab Frame

We shall now focus on the charged daughter decay angle in the lab frame, as this is the easiest observable with which to characterize the decay. Given a parent momentum (and associated Lorentz factors $\beta = p/E$ and $\gamma = 1/\sqrt{1-\beta^2}$), it is a simple matter to boost the CM momentum of the daughter and determine the lab decay angle.

$$\begin{aligned} \tan\theta^{lab} &= \frac{p_{\mathrm{T}}^{lab}}{p_z^{lab}} = \frac{p_{\mathrm{T}}^{CM}}{\gamma(p_z^{CM} + \beta E^{CM})} \\ &= \frac{\tan\theta^{CM}}{\gamma(1 + \beta\coth y^{CM})} \end{aligned} \tag{B.3}$$

Here we have used the rapidity variable $\tan y = p_z/E$ for the daughter in the CM frame. This quantity differs from the *pseudo*rapidity, $\eta = -\ln\tan\theta/2$, by terms of order $m^2/4p^2$. Since the daughter CM momentum is fixed, this correction is always 12%. If we approximate y with η, we can simplify the expression:

$$\tan\theta^{lab} \simeq \frac{\tan\theta^{CM}}{\gamma(1 - \beta(\ln\tan\theta^{CM}/2))} \ . \tag{B.4}$$

Even with this simplification, however, it is impossible to algebraically solve for θ^{CM} as a function of θ^{lab}, so we cannot write down an analytic expression for the distribution of decay angles in the lab frame for a fixed parent momentum. If the parent momentum is high enough, however, there can be an upper limit on the lab decay angle. Since the CM daughter momentum is fixed, a large boost from the parent will disallow large decay angles. We can see this by setting the derivative of θ^{lab} with

respect to θ^{CM} equal to zero.

$$\frac{d}{d\theta^{CM}} \tan\theta^{lab} = \frac{p^{CM}\sin\theta^{CM}}{\gamma(p^{CM}\cos\theta^{CM} + \beta E^{CM})} = 0 \tag{B.5}$$

$$\Rightarrow \tan\theta^{lab}_{max} = \frac{p^{CM}}{\gamma\sqrt{(\beta E^{CM})^2 - (p^{CM})^2}} \tag{B.6}$$

$$\Rightarrow \sin\theta^{lab}_{max} = \frac{\beta^{CM}\gamma^{CM}}{\beta\gamma} \tag{B.7}$$

In the last line, we have recast the expression for the maximum decay angle in terms of the parent Lorentz variables (β, γ) in the lab frame and the daughter Lorentz variables in the CM frame (β^{CM}, γ^{CM}). We have asserted that this is a maximum, and this can be proven by taking the second derivative. Note that there is no maximum decay angle below a certain parent momentum:

$$\beta < \beta^{CM} \quad \text{or} \quad p < m\frac{p^{CM}_{daughter}}{m_{daughter}} = \frac{m^2_{parent} - m^2_{daughter}}{2m_{parent}m_{daughter}} \tag{B.8}$$

References

[1] P. Braun-Munzinger et al. Hadron production in au-au collisions at rhic. *Phys. Lett. B*, 518:41–46, 2001.

[2] D. Magestro. Conference poster and private communication, 2002.

[3] A.M. Rossi et al. *Nucl. Phys. B*, 84, 1975.

[4] J.L. Bailly et al. *Phys. Lett. B*, 195, 1987.

[5] C. Y. Wong. *Introduction to High Energy Heavy-Ion Collisions*. World Scientific, 1994.

[6] K. Gottfried and V.F. Weisskopf. *Concepts of Particle Physics*, volume 2. Oxford University Press, 1986.

[7] K. Geiger and B. Müller. Dynamics of parton cascades in highly relativistic nuclear collisions. *Nucl. Phys. B*, 369:600–654, 1992.

[8] K. J. Eskola. Formation and evolution of quark-gluon plasma at rhic and lhc. *Nucl. Phys. A*, 590:383c–398c, 1995.

[9] J.W. Harris. Physics of the star experiment at rhic. 14th Winter Workshop on Nuclear Dynamics, 1998.

[10] J. Rafelski and B. Müller. Hadrons and the quark-gluon plasma. *Phys. Rev. Lett.*, 48:1066, 1982.

[11] F. Wang. Strangeness in dense nuclear matter: A review of ags results. *J.Phys. G*, 27:283–300, 2001.

[12] P. Braun-Munzinger et al. Maximum relative strangeness content in heavy ion collisions around 30 agev. *Nucl. Phys. A*, 697:902–912, 2002.

[13] M. Thoma, M. Gyulassy, M. Plumer, and X.N. Wang. High p_t probes of nuclear collisions. *Nucl. Phys. A*, 538:37, 1992.

[14] J.W. Cronin et al. Production of hadrons at large transverse momentum at 200, 300, and 400 gev. *Phys. Rev. D*, 11:3105, 1975.

[15] Thomas Roser. Rhic status and plans. RHIC Retreat, 2002.

[16] H.M. Calvani and L.A. Ahrens. Au 32+ beam intensity losses in the ags booster due to charge exchange processes. *Booster Technical Note*, (228), 1996.

[17] D. Kharzeev and M. Nardi. Hadron production in nuclear collisions at rhic and high density qcd. *Phys. Lett. B*, 507:121–128, 2001.

[18] W.H. Christie. Luminosity limits for the star detector system. *STAR Note*, (125), 1994.

[19] F. Bergsma et al. The star detector magnet subsystem. *Nucl. Instr. and Meth. A*, 499, 2003.

[20] F.S. Bieser et al. The star trigger. *Nucl. Instr. and Meth. A*, 499, 2003.

[21] C. Adler et al. The star level-3 trigger system. *Nucl. Instr. and Meth. A*, 499, 2003.

[22] M. Andersen et al. The star time projection chamber: A unique tool for studying high multiplicity events at rhic. *Nucl. Instr. and Meth. A*, 499, 2003.

[23] R. Bellwied et al. The star silicon vertex tracker: A large area silicon drift detector. *Nucl. Instr. and Meth. A*, 499, 2003.

[24] Wensheng Deng. *Charged kaon production in Au-Au collisions at sqrt(snn) = 130 GeV*. PhD thesis, Kent State University, 2002.

[25] X. N. Wang. 1997.

[26] *Eur. Phys. Jrnl. C*, 3(1-4):210–211, 1998.

[27] G. Van Buren. Soft physics in star. *Nucl.Phys. A*, 715:129–139, 2003.

[28] J. Zimányi et al. Quark liberation and coalescence at cern sps. *Phys. Lett. B*, 472:243, 2000.

[29] B. Hippolyte for the STAR Collaboration. Strange content of baryons at rhic. In *Proceedings for the XXXVIIIth Rencontres de Moriond, QCD and High Energy Hadronic Interactions*, 2003.

[30] et al. Y. Zhang. High-p_t pion and kaon production in relativistic nuclear collisions. *Phys.Rev. C*, 65(03), 2002.

[31] H.C. Eggers and J. Rafelski. Strangeness and quark gluon plasma: aspects of theory and experiment. *Int. J. Mod. Phys. A*, 6:1067–1114, 1991.

[32] T. Csörgo and B. Lørstad. Bose-einstein correlations for three-dimensionally expanding, cylindrically symmetric, finite systems. *Phys. Rev. C*, 54:1390–1403, 1996.

[33] T. Chujo. Results on identified hadrons from the phenix experiment at rhic. Quark Matter 2002, 2002.

[34] S.J. Brodsky and G.R. Farrar. Scaling laws at large transverse momentum. *Phys. Rev. Lett.*, 31:1153, 1973.

[35] M. Wing. Summary of session on jets and inclusive hadron production. Photon 2001, 2001.

[36] C. Adler et al. Kaon production and kaon to pion ratio in au+au collisions at $\sqrt{s_{NN}} = 130$ gev. nucl-ex/0206008, 2003.

[37] T. Alexopoulos et al. *Phys. Rev. D*, 48:984, 1993.

[38] C. Adler et al. Midrapidity antiproton-to-proton ratio from au+au $\sqrt{s_{NN}} = 130$ gev. *Phys. Rev. Lett.*, 86:4778–4782, 2001.

[39] A. Tounsi et al. Canonical aspects of strangeness enhancement. *Nucl.Phys. A*, 715:565–568, 2003.

[40] A. Drees. First hints of jet quenching at rhic. *Nucl. Phys. A*, 698:331–340, 2002.

[41] E. Wang and X.N. Wang. Interplay of soft and hard processes and hadron p_t spectra in *pa* and *aa* collisions. *Phys. Rev. C*, 64:034901, 2001.

[42] P. R. Bevington and D. K. Robinson. *Data Reduction and Error Analysis for the Physical Sciences.* McGraw-Hill, third edition, 2002.